Spectroscopy of localized excitons in carbon nanotubes

Dissertation
der Fakultät für Physik
der Ludwig-Maximilians-Universität München

vorgelegt von

Matthias Sebastian Hofmann
geboren in Starnberg

München, 27. Oktober 2016

Erstgutachter: Prof. Dr. Alexander Högele
Zweitgutachter: Prof. Dr. Achim Hartschuh
Tag der mündlichen Prüfung: 14.12.2016

Zusammenfassung

Halbleitende, einwandige Kohlenstoff-Nanoröhren sind nanoskalige Hohlzylinder aus Kohlenstoff-Atomen, deren Lichtemission von stark gebundenen Elektron-Loch-Paaren (Exzitonen) ausgeht. Die Photolumineszenz kann, je nach Röhrendurchmesser, im Spektralbereich von etwa 800 nm bis zu den Telekom-Wellenlängen liegen, was Kohlenstoff-Nanoröhren zu vielversprechenden Bauelementen für photonische und optoelektronische Anwendungen macht. Zudem wurde sogenanntes Antibunching in der Photonen-Emissionsstatistik nachgewiesen. Als Kennzeichen einer Einzelphotonenquelle offenbart diese Entdeckung großes Potential für den Einsatz in der Quantenkommunikation und -kryptographie. Photolumineszenzunterbrechungen (sogenanntes Blinken), spektrale Diffusion sowie schnelle Dekohärenz und Dephasierung von Exzitonen stellen jedoch technische Hürden dar, die es für die praktische Umsetzung derartiger Vorhaben zu überwinden gilt. Hierfür ist es erforderlich, sowohl extrinsische Effekte als auch die intrinsischen Eigenschaften der Nanoröhren-Photolumineszenz genauer zu untersuchen.

Im Rahmen dieser Arbeit wurde deshalb ein Aufbau zur chemischen Gasphasenabscheidung verwendet, um vom Substrat isolierte Röhren ohne Verunreinigungen herzustellen und deren optische Eigenschaften studieren zu können. Dazu wurde eine systematische Studie mehrerer Wachstumsparameter durchgeführt. So konnten Bedingungen identifiziert werden, die das Wachstum von isolierten Nanoröhren mit Durchmessern im Subnanometerbereich und großen Bandlücken für weitere optische Untersuchungen begünstigen.

Auf diese Weise hergestellte, vom Substrat gelöste Röhren zeigten deutlich verschiedene optische Eigenschaften im Vergleich zu Nanoröhren auf einem Siliziumdioxid-Substrat: Sie wiesen symmetrische Emissionslinien mit Halbwertsbreiten im Bereich von wenigen Millielektronvolt und stabile Emissionsenergien und -intensitäten auf. Die Photolumineszenz von Röhren auf dem Dielektrikum hingegen war aufgrund von Ladungsfluktuationen im Substrat spektraler Diffusion und Intensitätsschwankungen unterworfen. Zudem zeigten sich bei tiefen Temperaturen bemerkenswert schmale Emissionslinien mit niederenergetischen Seitenpeaks. Das verwendete Modell zur Reproduzierung der optischen Spektren lässt darauf schließen, dass lokalisierte Exzitonen und eine substratinduzierte Modifikation ihrer Kopplung an akustische Phononen für diese spektralen Besonderheiten ausschlaggebend sind.

Weitere optische Merkmale unbeabsichtigter Exzitonlokalisierung in substratgestützten Nanoröhren wurden anhand der spektralen Eigenschaften sowie der räumlich aufgelösten Photolumineszenz entlang der Röhrenachse identifiziert. Die Quantifizierung der zugrunde liegenden Fallenpotentiale, die von Umgebungsstörungen und von kovalent-gebundenen Gitterdefekten induziert werden, ergab Lokalisierungsenergien im Bereich von wenigen bis zu einigen Zehn Millielektronvolt. Darüber hinaus zeigen die Ergebnisse, dass der unordnungsbedingte Übergang vom diffusiven zum lokalisierten Exziton-Regime bei tiefen Temperaturen ein allgemein auftretendes Phänomen darstellt, sowohl in den vielverwendeten Kohlenstoff-Nanoröhren mit Mizellen-Ummantelung als auch in nicht weiterverarbeiteten Nanoröhren aus dem hauseigenen Herstellungsprozess.

Im letzten Abschnitt der Arbeit wird gezeigt, dass die anfangs beschriebenen Einschränkungen für quantenphotonische Anwendungen durch lokalisierte Exzitonen in freihängenden Kohlenstoff-Nanoröhren überwunden werden können. Die Photolumineszenz dieser Röhren zeigte schmale Emissionslinien ohne spektrale Schwankungen und ohne Intensitätsunterbrechungen, Zerfallszeiten gemäß den theoretischen Vorhersagen von einigen Nanosekunden, Photon-Antibunching sowie starke Anzeichen für eine signifikante Steigerung der Quantenausbeute.

Abstract

Semiconducting single-walled carbon nanotubes are nanoscale, hollow cylinders with photoluminescence of strongly bound electron-hole pairs (excitons). The optical emission shows diameter-dependent wavelengths that vary between 800 nm and the telecom wavelengths, rendering carbon nanotubes as promising building blocks for photonic and optoelectronic devices. Moreover, the recent discovery of antibunching in the photon emission statistics—the hallmark of a single-photon source—reveals significant potential for application in quantum communication and cryptography. Photoluminescence blinking, spectral diffusion, and rapid exciton decoherence and dephasing, however, challenge the practical implementation of related schemes. In this context, it is essential to investigate both the extrinsic effects and the intrinsic properties of the nanotube photoluminesence.

In the framework of this thesis, a chemical vapor deposition setup was employed to fabricate pristine carbon nanotubes detached from the substrate for photophysical studies. To this end, a systematic study of several growth parameters was conducted. By this means, conditions that favor the synthesis of isolated carbon nanotubes with subnanometer diameters and wide band gaps for optical investigations were identified.

Environmentally isolated carbon nanotubes grown with this method revealed optical properties clearly different from tubes supported by silica: The optical emission exhibited symmetric spectral profiles with full width at half maximum linewidths on the scale of millielectronvolts as well as stable emission energies and intensities. In contrast, the photoluminescence of tubes pinned to the dielectric was subjected to spectral diffusion and intensity fluctuations caused by charge fluctuations in the substrate. Furthermore, a remarkably narrow emission line with a low-energy side peak appeared at low temperatures. These spectral peculiarities were well reproduced by a model that implies localized excitons and substrate-induced modifications of their coupling to acoustic phonons.

The analysis of spectral features and the spatially resolved photoluminescence along the nanotube axis identified characteristic signatures of unintentional exciton localization in substrate-supported carbon nanotubes. Exciton localization was found to be induced by extrinsic disorder and covalent sidewall defects with exciton trapping potentials ranging from a few to tens of millielectronvolts. Moreover, the results establish disorder-induced crossover from the diffusive to the localized regime of carbon nanotube excitons at cryogenic temperatures as a general feature for widely used micelle-encapsulated tubes and as-grown carbon nanotubes by the in-house fabrication method.

Ultimately, it is demonstrated that the challenges for quantum photonic applications may be overcome by localized excitons in suspended carbon nanotubes: The photoluminescence of these tubes exhibited narrow optical lines free of spectral wandering and intensity intermittence, flourescence lifetimes of several nanoseconds as predicted by theory, photon antibunching as well as strong indication of a significant increase in the quantum yield.

Contents

Zusammenfassung iii

Abstract v

1 Introduction 1

2 Fundamentals of single-walled carbon nanotubes 5
2.1 Crystal structure . . . 6
2.1.1 Real space lattice . . . 6
2.1.2 Phonons and Raman scattering . . . 9
2.1.3 Reciprocal space . . . 11
2.2 Electronic properties and band structure . . . 12
2.2.1 Optical band-to-band transitions . . . 13
2.2.2 Excitonic photoluminescence . . . 15

3 Experimental setup for optical spectroscopy of individual carbon nanotubes 19
3.1 The cryogenic confocal microscope . . . 20
3.2 Spatial resolution of the confocal microscope . . . 22
3.3 Photodetection devices and setups . . . 23
3.3.1 Acquisition of optical spectra . . . 23
3.3.2 Second-order photon correlation measurements . . . 23
3.3.3 Time-resolved photoluminescence measurements . . . 25

4 Growth of small-diameter carbon nanotubes by chemical vapor deposition 27
4.1 Introduction . . . 28
4.2 Chemical vapor deposition . . . 28
4.2.1 Basic principles . . . 28
4.2.2 Carbon precursor and catalyst . . . 29
4.2.3 Setup and growth procedure . . . 30
4.3 Influence of synthesis parameters on carbon nanotube growth . . . 32
4.3.1 Areal density: influence of temperature and gas flow rate . . . 32
4.3.2 Length distribution: effect of oxygen plasma treatment of the catalyst 33
4.3.3 Carbon nanotube diameters: influence of temperature and gas flow rate . . . 34
4.4 Analysis by Raman spectroscopy . . . 37
4.5 Conclusion . . . 38

5 Photoluminescence spectroscopy of individual as-grown carbon nanotubes 41
5.1 Introduction . . . 42
5.2 Carbon nanotubes on a silica substrate . . . 43
5.2.1 Sample fabrication . . . 43
5.2.2 Photoluminescence of as-grown carbon nanotubes on silica . . . 44
5.3 Suspended carbon nanotubes . . . 50
5.3.1 Perforated substrates for suspended carbon nanotubes . . . 50
5.3.2 Photoluminescence of suspended carbon nanotubes . . . 50
5.4 Conclusion . . . 55

6 Exciton localization in cryogenic carbon nanotubes 57
6.1 Introduction . . . 58
6.2 Carbon nanotube samples . . . 59
6.3 Hyperspectral mapping of exciton localization . . . 60
6.4 Analysis of multi-peak emission spectra . . . 62
6.5 Adsorbate-induced disorder . . . 67
6.6 Conclusion . . . 68

7 Excitons in suspended carbon nanotube quantum dots 69
7.1 Introduction . . . 70
7.2 Sample layout . . . 70
7.3 Cryogenic photoluminescence spectroscopy . . . 71
7.3.1 Photoluminescence excitation spectroscopy . . . 73
7.3.2 Temporal evolution of the photoluminescence . . . 75
7.3.3 Time-resolved photoluminescence and photoluminescence saturation . . . 77
7.3.4 Second-order photon correlation . . . 80
7.4 Photoluminescence at 77 K and at room temperature . . . 81
7.5 Conclusion . . . 84

8 Summary and perspectives 87

Appendix A Diameter distributions of as-grown carbon nanotubes 91

Appendix B Sample fabrication by optical lithography 93

Appendix C Temperature dependence of the band gap 95

Bibliography 97

List of abbreviations 111

List of publications 113

Danksagung 115

Chapter 1

Introduction

"Dwarf"—that's the meaning of the greek word *νᾶνος*, from which the term *nano* is derived. Used as a unit prefix, *nano* designates a factor of one billionth, e. g. 1 nm = 10^{-9} m = 0.000 000 001 m. However, *nano* may nowadays also stand for an entire branch of modern technology with a budget of billions of dollars. One may call nanoscience "a very handy word for rather small things with a rather big impact" [1]. A more formal definition, however, describes nanotechnology as the study, manipulation, and manufacture of materials and devices on the scale of approximately 1–100 nm. Nanotechnology is not essentially new—even though in earlier times people were unaware of its usage. For example, in the medieval period, stained glass artisans used tiny gold or silver particles to generate the colored windows that can still be marveled at in many churches across Europe. Nowadays we know from modern imaging and characterization techniques that it is the different sizes of the particles at the nanoscale that define the variations in color.

The fact that matter at the nanoscale unveils properties and effects fundamentally different from the behavior of bulk materials is one of the main driving forces behind the extensive efforts of the past decades in the field of nanotechnology. The unique phenomena found at small length scales enable novel solutions and applications for various disciplines such as medicine and pharmaceuticals, biology, chemistry, materials science, electrical engineering, or optoelectronics.

Among the most remarkable materials in nanoscience are carbon nanotubes. These are cylindrical carbon molecules with either metallic or semiconducting behavior depending on the arrangement of the carbon atoms in the hexagonal lattice [2]. Carbon nanotubes may reach aspect ratios of up to 500,000,000:1 [3] and feature superior electrical and thermal conductivities as well as outstanding tensile strength [2, 4]. By virtue of its exceptional physical properties this nano-carbon material is a promising candidate for a vast variety of applications ranging from thin-film heaters and transistors, to supercapacitors, water filters, or biosensors [5]. Furthermore, semiconducting carbon nanotubes are direct band gap materials that exhibit large binding energies of excited electron-hole pairs around 0.4 eV resulting in excitonic photoluminescence even at room temperature [6, 7]. Additionally, as the optical band-to-band transition energies scale inversely with the tube diameter, it is possible to tune the light emission from near-infrared to telecom wavelengths by appropriate choice of the carbon nanotube species. Consequently, carbon nanotubes are particularly interesting for the

fields of optoelectronics and photonics [8], and have already been explored for various optoelectronic device applications including light-emitting diodes [9, 10], infrared photodetectors [11–13], and photovoltaic cells [14–16]. Recently, semiconducting carbon nanotubes have also attracted interest for uses in quantum photonics as they exhibit single-photon emission as the hallmark of exciton localization at cryogenic temperatures [17,18]. This generation of quantum light states is pivotal to advanced technologies such as quantum key distribution for secure communications and in contrast to approaches based on compound semiconductor quantum dots, the large exciton binding energies in carbon nanotubes principally allow for room temperature operation. However, for successful implementation of such a carbon nanotube-based device, other fundamental problems have to be overcome: typically, the photoluminescence of carbon nanotubes strongly suffers from extrinsic perturbations. This is not surprising as single-walled carbon nanotubes exhibit all-surface excitons that are highly sensitive to their immediate surrounding and environment. As a result, spectral variations [19] and intensity blinking [20] are commonly observed. Adding to that, defective lattice sites may further reduce the photoluminescence efficiency by nonradiative recombination of charge carriers [21]. For quantum cryptography operations, however, highly efficient, spectrally pure, and stable emission is required.

The work in the scope of this thesis aimed at eliminating disorder and extrinsic perturbations by direct growth of carbon nanotubes with minimized environmental interactions. To this end, the method of catalytic chemical vapor deposition was employed for synthesis of spatially isolated carbon nanotubes pinned to silica and suspended over holes and craters ideally suited for optical studies of exciton photoluminescence and exciton localization effects.

The thesis is structured as follows: After introducing the theoretical aspects of carbon nanotubes and carbon nanotube photophysics in *Chapter 2*, the design and specifications of the home-built confocal microscope for cryogenic single carbon nanotube spectroscopy as well as the various detection devices are presented in *Chapter 3*.

Chapter 4 considers the method of chemical vapor deposition: After a brief introduction into the basics of carbon nanotube growth by catalytic chemical vapor deposition, the motivation for the choice of the employed reaction gases (methane and hydrogen) as well as for the alumina-supported bimetallic catalyst (iron-ruthenium) is given. Furthermore, details of the catalyst preparation, the chemical vapor deposition reactor, and the growth procedure are described. The experimental section of this chapter presents a systematic study of various synthesis parameters and their influences on the carbon nanotube areal density, the average length, and the nanotube diameters. Synthesis conditions that favor small-diameter and wide band gap carbon nanotubes were successfully identified and applied for samples with carbon nanotubes fully suspended over holes that allowed for investigation of the material quality by Raman spectroscopy.

Chapter 5 presents cryogenic photoluminescence studies of individual as-grown carbon nanotubes. The results not only demonstrate the successful fabrication of luminescent large band gap carbon nanotubes by the synthesis method described in Chapter 4, but also reveal and exemplify the influences of a silica substrate on the photophysical properties by means of characterizing the photoluminescence from carbon nanotubes directly grown on silicon oxide and suspended over holes.

Chapter 6 presents studies of unintentional exciton localization in three different

carbon nanotube materials: micelle-encapsulated HiPco and CoMoCAT tubes as well as as-grown carbon nanotubes from the in-house chemical vapor deposition method. The comprehensive study based on spatial photoluminescence mapping and single-tube spectroscopy identifies disorder-induced transition from diffusive excitons at room temperature to localized exciton states at cryogenic temperatures as a universal feature in all investigated material systems and allows for quantification of the exciton localization energy scales.

In *Chapter 7* it is demonstrated that common inefficiencies in nanotube photoluminescence—such as rapid decoherence, environmental dephasing, spectral wandering, and intensity fluctuations—can be effectively suppressed in suspended carbon nanotubes at cryogenic temperatures. The observed features of narrow, stable, and bright emission lines stem from long-lived localized excitons as revealed by photon correlation measurements. The results are complemented by signatures of single-photon emission at room temperature and constitute a promising advance for carbon nanotube-based quantum photonic applications.

A summary of the obtained findings and an outlook that provides possible directions for future experiments are given in *Chapter 8*.

Chapter 2

Fundamentals of single-walled carbon nanotubes

This chapter presents an overview of the fundamental physical properties of single-walled carbon nanotubes. Starting from the hexagonal lattice of graphene, the geometric characteristics of carbon nanotubes are derived and distinctive Raman-active vibrational modes are discussed. Zone-folding of graphene's electronic band structure yields the electronic dispersion relation of single-walled carbon nanotubes and predicts metallic or semiconducting behavior depending on the specific geometric structure. Due to the one-dimensional character of carbon nanotubes, Coulomb interactions between excited charge carriers are significantly enhanced as compared to bulk materials, resulting in strongly bound excitons that dominate the photoluminescence of semiconducting single-walled carbon nanotubes.

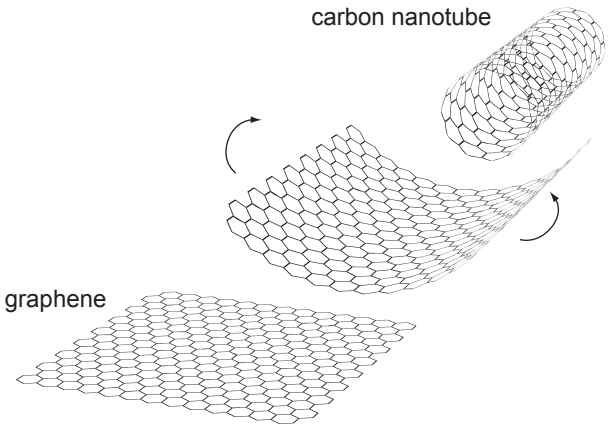

Figure 2.1: Illustrative formation of a single-walled carbon nanotube by rolling up a monoatomic layer of graphite (graphene) to a seamless cylinder.

2.1 Crystal structure

This section gives a short introduction to the structural properties of single-walled carbon nanotubes (SWNTs) in terms of the real space lattice and its modes of vibrations, as well as in terms of the reciprocal lattice which is crucial for the determination of the electronic and optical properties.

2.1.1 Real space lattice

For illustrative purposes a SWNT is commonly described as being formed from a layer of graphene (i. e. a monolayer of graphite) that is rolled up to a seamless cylinder (Figure 2.1). The graphene sheet consists of sp^2-hybridized carbon atoms that build a two-dimensional (2D) honeycomb lattice and provides the basis for the structural description of SWNTs via the real space unit vectors $\mathbf{a}_1$ and $\mathbf{a}_2$ [2]. In the x,y coordinate system as depicted in Figure 2.2a, the lattice vectors are given by

$$\mathbf{a}_1 = \left(\frac{\sqrt{3}}{2}, \frac{1}{2}\right) \cdot a\,, \quad \mathbf{a}_2 = \left(\frac{\sqrt{3}}{2}, -\frac{1}{2}\right) \cdot a\,, \tag{2.1}$$

where $a = |\mathbf{a}_1| = |\mathbf{a}_2| = \sqrt{3} \cdot a_{C-C} = 2.46\,\text{Å}$ is the lattice constant and $a_{C-C} = 1.42\,\text{Å}$ is the bond distance between two carbon atoms in graphene[1].

The SWNT diameter and the crystallographic orientation with respect to the nanotube axis is determined by the chiral vector $\mathbf{C}_h$ that connects two lattice points that come to lie on each other when rolling up the graphene sheet. The chiral vector is described by the linear combination

$$\mathbf{C}_h = n \cdot \mathbf{a}_1 + m \cdot \mathbf{a}_2 \equiv (n, m)\,. \tag{2.2}$$

[1] The nearest-neighbor distance between two carbon atoms in carbon nanotubes is slightly larger than in graphene: $a_{C-C}^{\text{CNT}} = 1.44\,\text{Å}$

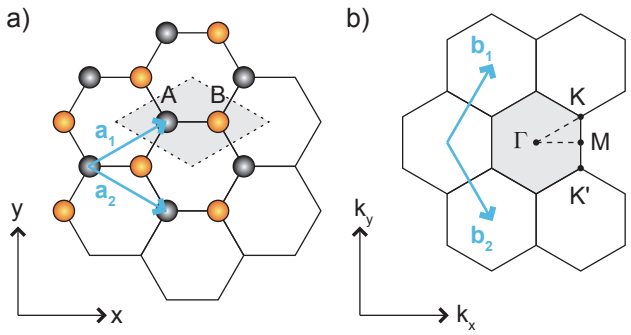

Figure 2.2: a) Real space lattice of graphene. The unit cell (gray shaded area) is spanned by the unit vectors $\mathbf{a}_1$ and $\mathbf{a}_2$ and contains two inequivalent carbon atoms that belong to the two different sublattices A and B of the honeycomb structure. b) Reciprocal lattice of graphene spanned by the reciprocal lattice vectors $\mathbf{b}_1$ and $\mathbf{b}_2$. The first Brillouin zone is given by the gray shaded area. Γ, K, K', and M are the high symmetry points.

The pair of positive integers (n,m) is called the chiral index or the chirality of a SWNT. Due to the symmetry of the hexagonal lattice, all possible SWNTs can be described by integers n, m restricted to $0 \leq m \leq n$. The schematic construction of different chiralities is depicted in Figure 2.3.

By definition, the length of the chiral vector, $|\mathbf{C}_h|$, equals the circumference of the nanotube and defines the diameter d_t of a specific SWNT according to:

$$d_t = \frac{|\mathbf{C}_h|}{\pi} = \frac{a}{\pi}\sqrt{n^2+nm+m^2}\,. \tag{2.3}$$

The angle between the vectors $\mathbf{C}_h$ and $\mathbf{a}_1$ is called the chiral angle θ with

$$\cos\theta = \frac{\mathbf{C}_h \cdot \mathbf{a}_1}{|\mathbf{C}_h|\,|\mathbf{a}_1|} = \frac{2n+m}{2\sqrt{n^2+nm+m^2}}\,. \tag{2.4}$$

Since the chiral index is limited to $0 \leq m \leq n$ by the hexagonal symmetry of the lattice, the values of θ accordingly are in the range $0° \leq \theta \leq 30°$.

Depending on the SWNT structure, three main classifications are commonly distinguished: zigzag, armchair, and chiral nanotubes.

- Zigzag SWNTs are defined by $\theta = 0°$, corresponding to a chirality of $(n,0)$. The name stems from the characteristic "zigzag" pattern along the chiral vector (see Figure 2.3).
- Armchair SWNTs have a chiral angle of $\theta = 30°$ and consequently a chiral index of (n,n). Again, the arrangement of carbon atoms along the chiral vector is responsible for the naming "armchair" (see Figure 2.3).
- The remaining nanotube species with $0 < m < n$ and $0° < \theta < 30°$ are called "chiral" SWNTs.

The unit vector of a one-dimensional (1D) SWNT is given by the translation vector $\mathbf{T}$, which points along the SWNT's axis and is perpendicular to $\mathbf{C}_h$ in the unrolled hexagonal

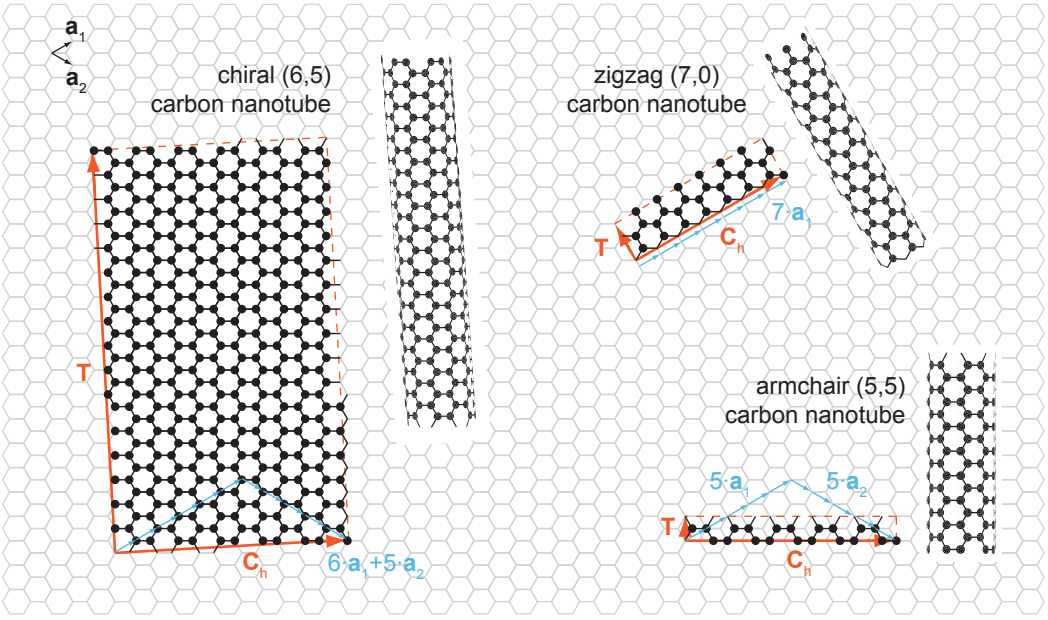

Figure 2.3: Construction scheme of single-walled carbon nanotubes from a graphene layer. The chiral vector $\mathbf{C}_h$ is a linear combination of the unit vectors $\mathbf{a}_1$ and $\mathbf{a}_2$. The unit cell of a single-walled carbon nanotube is spanned by $\mathbf{C}_h$ and the translation vector $\mathbf{T}$. Rolling up the graphene ribbon along $\mathbf{C}_h$ to a seamless cylinder leads to formation of a single-walled carbon nanotube of specific chirality (n,m). Depicted examples are a chiral $(6,5)$, a zigzag $(7,0)$, and an armchair $(5,5)$ carbon nanotube.

lattice, i. e. $\mathbf{C}_h \cdot \mathbf{T} = 0$. Using the lattice vectors $\mathbf{a}_1$ and $\mathbf{a}_2$, $\mathbf{T}$ can be expressed as

$$\mathbf{T} = \frac{2m+n}{d_R} \cdot \mathbf{a}_1 - \frac{2n+m}{d_R} \cdot \mathbf{a}_2 \,, \tag{2.5}$$

with d_R being the greatest common divisor of $(2m+n)$ and $(2n+m)$. The unit cell of a SWNT is then given by a cylinder of length $|\mathbf{T}| = \sqrt{3}\,|\mathbf{C}_h| / d_R$ and diameter d_t.

The number of hexagons per unit cell N is calculated by dividing the unit cell area $|\mathbf{C}_h \times \mathbf{T}|$ by the area of one hexagon $|\mathbf{a}_1 \times \mathbf{a}_2|$:

$$N = \frac{|\mathbf{C}_h \times \mathbf{T}|}{|\mathbf{a}_1 \times \mathbf{a}_2|} = \frac{2\left(n^2 + nm + m^2\right)}{d_R} \,. \tag{2.6}$$

Since every hexagon of the graphene lattice contains two carbon atoms, each SWNT unit cell consists of $2N$ carbon atoms.

2.1.2 Phonons and Raman scattering

In the framework of classical mechanics, a phonon can be understood as an elementary wave-like vibration of the lattice, designated as a normal mode. However, being the quantum mechanical description of elementary vibrational motions, they are commonly denoted as quasiparticles and represent the quantized excitations of lattice vibrations with energy $\hbar\omega_{\mathrm{ph}}$, where $\hbar$ is the reduced Planck constant and ω_{ph} is the phonon frequency.

The vibrational properties and phonon dispersion relations of SWNTs are closely related to the ones of the 2D graphene sheet and can be almost fully derived by the so-called zone-folding approximation, which will be discussed in more detail for the determination of the electronic properties of SWNTs in Section 2.2. For a thorough description of the zone-folding method for phonons the reader is referred to Ref. 2. The result of the approach is a variety of phonon bands. More precisely, the $2N$ carbon atoms of the unit cell of a SWNT yield $6N$ phonon dispersion relations. However, in the following only the few phonons that interact with light through Raman scattering, so-called Raman-active modes, will be considered.[2]

For carbon nanotubes (CNTs), Raman scattering refers to the inelastic scattering of light (typically provided by a laser) from phonons. Because of energy conservation, the energy of the scattered photon is given by

$$\hbar\omega_{\mathrm{scat}} = \hbar\omega_{\mathrm{L}} \pm \hbar\omega_{\mathrm{ph}}\,, \tag{2.7}$$

where ω_{L} is the laser frequency and ω_{ph} is the frequency of the phonon that is absorbed $(+)$ or created $(-)$ by the photon in the so-called anti-Stokes or Stokes Raman process, respectively. The Raman intensity is strongly enhanced when either the laser energy or the scattered photon energy is in resonance with a real optical transition (resonance Raman scattering). In case these resonance conditions are not met, a Raman signal from individual CNTs is typically not detected.

Being a non-destructive and cheap analysis technique, Raman spectroscopy has become a popular tool for CNT sample characterization. The scattered photons provide instructive information on the vibrational and electronic properties as well as on structural quality.

The main and most important Raman bands of SWNTs are the following:

- **RBM.** The in-phase vibration of all carbon atoms in the radial direction, as indicated in Figure 2.4a, is called the radial breathing mode (RBM) and is a unique feature of SWNTs. Its frequency is strongly dependent on the nanotube diameter[3] which makes the RBM a popular feature for deducing CNT chiralities. However, due to its small energy, spectral filters with sharp edges close to the excitation laser line are needed for successful detection.

- **G-band.** The most prominent feature is the G-band which is common to all sp^2-hybridized carbon materials. It corresponds to an in-plane stretching mode of the

[2] The number of Raman active phonons can be deduced by point group theory [2].

[3] The RBM frequency can be described by $\omega_{\mathrm{RBM}}\left[\mathrm{cm}^{-1}\right] = \frac{227}{d_t[\mathrm{nm}]}\sqrt{1 - C\,d_t^2[\mathrm{nm}^2]}$, where C accounts for interactions with the environment [23].

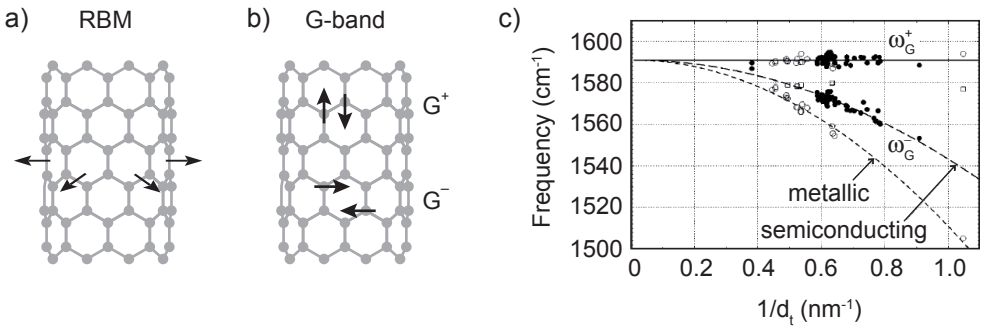

Figure 2.4: a) Illustration of the radial breathing mode (RBM) that corresponds to an in-phase vibration of each carbon atom in the radial direction. b) The G-mode corresponds to C–C stretching vibrations tangential to the nanotube surface. Vibrations along the tube's axis and vibrations along the circumference have different energies and are referred to as G^+ and G^-, respectively. c) Raman frequencies of the G^+ and G^- bands as a function of the inverse nanotube diameter d_t. The frequency of the G^+ mode is independent of d_t as indicated by the flat solid line. Dashed curves are fits to the data points for ω_G^- of metallic (open circles) and semiconducting (filled circles) single-walled carbon nanotubes. Adapted from Ref. 22.

carbon atoms. As a consequence of the curvature of the nanotube sidewall, the band is composed of two peaks for SWNTs: The higher frequency component G^+ at 1591 cm^{-1} (197 meV) is related to C–C stretching along the SWNT axis while the low-frequency component G^- is associated to stretching vibrations along the circumference (cf. Figure 2.4b). Due to this fact, the splitting of G^+ and the G^--mode is dependent on the SWNT diameter (Figure 2.4c) [22].

- **D-band.** A diameter dependence is also observed for the D-band which results from a scattering process that is only allowed by the presence of defects or impurities. Thus, it can be used as a measure of imperfections in the SWNT crystalline structure [24–27]. The Raman shift of the D-band shows a weak laser dependent dispersion and is typically located around 1300 cm^{-1} (~160 meV) for excitation with a red laser [28].

- **G'-band.** The G'-mode is the overtone of the D-band and is located at around 2600 cm^{-1} (~320 meV). It involves two phonons with opposite momentum, and—in contrast to its first harmonic—does not require a defect.

A Raman spectrum depicting the introduced CNT phonon bands is shown in Figure 2.5. Also worth mentioning are the low-intensity intermediate frequency modes (IFM) in the spectral range between the RBM and the D-band, the M-band around 1750 cm^{-1} with a non-dispersive (M^+) and a dispersive (M^-) component, as well as combination modes such as G+RBM [28].

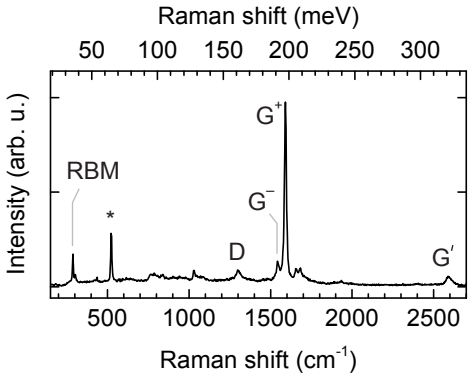

Figure 2.5: Raman spectrum of a carbon nanotube. The most prominent Raman bands are the radial breathing mode (RBM), the defect-induced D-band, the C–C stretching vibrational G-band (composed of G^+ and G^-), and the G'-band (the overtone of the D-band). The Raman peak marked with the asterisk stems from the silicon substrate.

2.1.3 Reciprocal space

In general, the reciprocal space of a given lattice with unit vectors $\mathbf{A}_i$ is spanned by a set of reciprocal lattice vectors $\mathbf{B}_i$ which are defined by the relation

$$\mathbf{A}_i \cdot \mathbf{B}_j = 2\pi\delta_{ij}\,, \tag{2.8}$$

where δ_{ij} is the Kronecker delta. Thus, the reciprocal basis vectors for the 2D graphene sheet are given by [2]

$$\mathbf{b}_1 = \left(\frac{1}{\sqrt{3}}, 1\right) \cdot \frac{2\pi}{a}\,, \quad \mathbf{b}_2 = \left(\frac{1}{\sqrt{3}}, -1\right) \cdot \frac{2\pi}{a}\,. \tag{2.9}$$

Figure 2.2b depicts the hexagonal reciprocal lattice of 2D graphene spanned by the reciprocal basis vectors $\mathbf{b}_1$ and $\mathbf{b}_2$ as well as the first Brillouin zone with the high symmetry points Γ, K, K', and M.

As already mentioned in Section 2.1.1, the real space unit cell of a SWNT is constructed by the chiral vector $\mathbf{C}_h$ and the translation vector $\mathbf{T}$. The corresponding reciprocal lattice vectors $\mathbf{K}_1$ and $\mathbf{K}_2$ can be deduced from Equations 2.2, 2.5, 2.8, and 2.9:

$$\mathbf{K}_1 = \frac{2n+m}{N\,d_R}\,\mathbf{b}_1 + \frac{2m+n}{N\,d_R}\,\mathbf{b}_2\,, \quad \mathbf{K}_2 = \frac{m}{N}\,\mathbf{b}_1 - \frac{n}{N}\,\mathbf{b}_2\,, \tag{2.10}$$

with $\mathbf{K}_1$ pointing in the circumferential direction and $\mathbf{K}_2$ being the reciprocal lattice vector along the SWNT axis.

Wave vectors along the SWNT axis can take quasi-continuous values if one makes the assumption of an infinitely long nanotube. However, wave vectors along the direction of $\mathbf{C}_h$ are quantized due to the finite circumference that requires the phase of the wave function to be an integer multiple of 2π after one circulation, yielding

$$k_\perp = \mu \cdot \frac{2\pi}{|\mathbf{C}_h|}\,, \tag{2.11}$$

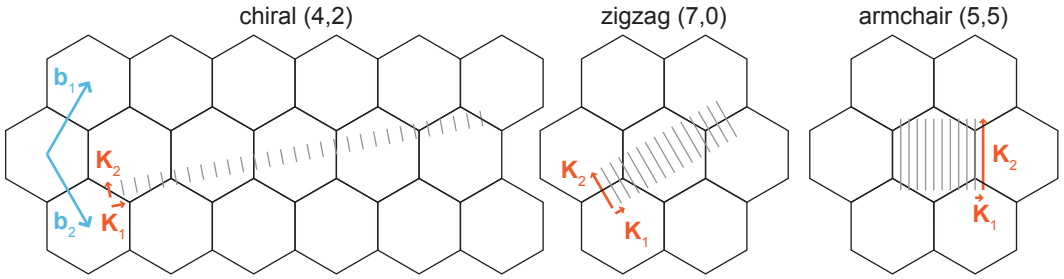

Figure 2.6: The first Brillouin zones for a chiral (4,2), a zigzag (7,0), and an armchair (5,5) single-walled carbon nanotube are depicted as gray lines parallel to the reciprocal lattice vectors $\mathbf{K}_2$. Quantization of the wave vectors due to periodic boundary conditions along the nanotube circumference gives rise to the N equidistant lines.

where $\mu = -\frac{N}{2}+1, \ldots, \frac{N}{2}$. Because of the 1D character of a SWNT, the first Brillouin zone is composed of N equidistant line segments parallel to $\mathbf{K}_2$, as depicted for three exemplary SWNTs in Figure 2.6. Depending on the specific chirality (n,m), the lines of the first Brillouin zone may include the K (or K') point of hexagonal graphene which will have major consequences for the electronic properties of a SWNT as will be shown in the next section.

2.2 Electronic properties and band structure

Being the sixth element of the periodic table, atomic carbon has four valence electrons that occupy the $2s^2$ and $2p^2$ orbitals. In the graphene lattice, however, carbon is sp^2-hybridized, meaning that the $2s$ orbital and two $2p$ orbitals (e. g. $2p_x$ and $2p_y$) mix to enhance the binding energy. The result is the formation of three in-plane sp^2 orbitals that are responsible for the strong covalent bonds (σ bonds) between the atoms. The remaining fourth electron of each carbon atom occupies the $2p_z$ orbital perpendicular to the graphene layer and forms the weaker π bonds. It is these π orbitals, i. e. the bonding π and antibonding π^* orbitals, that constitute the electronic system in terms of the valence and conduction band, respectively. As detailed by Saito *et al.* [2], a simple tight-binding approach for the π electrons gives a reasonable approximation for the energy dispersion relation in 2D graphene:

$$E_{\mathrm{g2D}}(\mathbf{k}) = \frac{\epsilon_{2p} \pm \gamma_0\, w(\mathbf{k})}{1 \pm s\, w(\mathbf{k})}, \tag{2.12}$$

where the + and − signs correspond to the valence (bonding π) and the conduction (antibonding π^*) band, respectively, and the function $w(\mathbf{k})$ is given by

$$w(\mathbf{k}) = \sqrt{1 + 4\cos\frac{\sqrt{3}k_x a}{2}\cos\frac{k_y a}{2} + 4\cos^2\frac{k_y a}{2}}. \tag{2.13}$$

Commonly chosen values for the parameters in Equation 2.12 are $\epsilon_{2p} = 0$, $\gamma_0 = -3.033$ eV, and $s = 0.129$ [2]. The resulting energy dispersion curve is depicted in Figure 2.7. The fully occupied valence band and the unoccupied conduction band are degenerate at the K and K' points at the first Brillouin zone boundary. Since the 2D density of

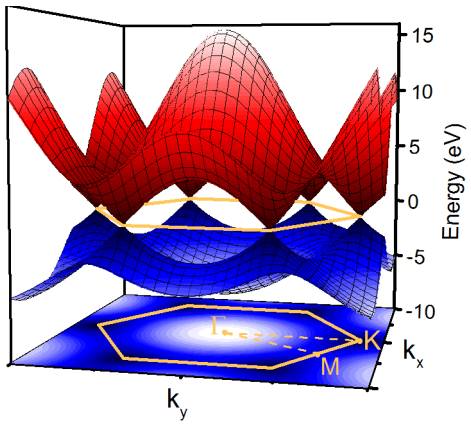

Figure 2.7: Energy dispersion relation of graphene. The valence band (blue surface) and the conduction band (red surface) are degenerate at the K (K') points of the first Brillouin zone which is depicted as orange hexagon. The bonding π band is projected onto the k_x,k_y-plane at the bottom.

states at these points is zero, graphene is a zero-gap semiconductor. Additionally, the linear dispersion at the K and K' points makes electrons and holes behave as pseudo-relativistic particles.

A good approximation to obtain the SWNT energy dispersion is made by taking cuts from the band structure of graphene along the N lines of the SWNT Brillouin zone. The resulting 1D band structure from this so-called zone-folding approach is given by

$$E_\mu(k) = E_{\mathrm{g2D}}\left(k\frac{\mathbf{K}_2}{|\mathbf{K}_2|} + \mu\mathbf{K}_1\right), \tag{2.14}$$

where $-\frac{\pi}{|\mathbf{T}|} < k < \frac{\pi}{|\mathbf{T}|}$ and $\mu = -\frac{N}{2}+1, \ldots, \frac{N}{2}$.

Depending on the SWNT chirality (n,m), the cutting lines that form the nanotube energy dispersion relation may cross a K (K') point of the graphene Brillouin zone where the valence and conduction bands are degenerate (Figure 2.8). In this case it can be shown that the SWNT has a non-zero density of states at the Fermi level resulting in metallic properties. In particular, a SWNT is metallic if $(2n+m)$ is a multiple of 3, or in other words, if $(2n+m)\mathrm{mod}(3) = 0$. In all other cases the 1D energy dispersion has a finite band gap and the SWNT is semiconducting.

2.2.1 Optical band-to-band transitions

As the density of states $D(E)$ describes the number of available states in the energy interval $[E, E+dE]$, it is of central interest when considering optical transitions, especially in SWNTs where the 1D structure gives rise to singularities with a divergent density of states at the minima and maxima of the energy bands, known as Van Hove singularities (VHs) (note the spikes in Figure 2.8c). Because of the large number of available states and the resulting large transition probability, optical transitions occur predominantly between the VHs at energies labeled as E_{ij}, where i and j denote the order of the involved VHs of the valence band (v_i) and the conduction band (c_j) with respect to

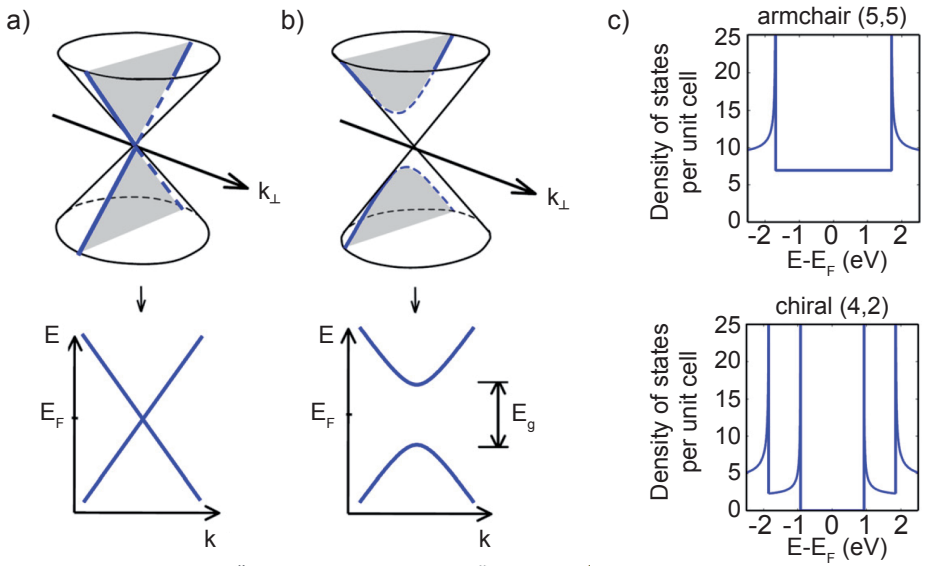

Figure 2.8: a) Dirac cone of the energy dispersion of graphene and a cutting line of allowed wave vector $k_\perp$ crossing the K point resulting in the one-dimensional band structure of a metallic single-walled carbon nanotube. b) If the allowed wave vectors $k_\perp$ do not cross the K point, the energy dispersion of the single-walled carbon nanotube exhibits a band gap E_g. c) The density of states of a metallic armchair (5,5) nanotube has a finite value at the Fermi level E_F whereas the density of states of the semiconducting chiral (4,2) nanotube is zero around the Fermi energy. Adapted from Ref. 29.

the Fermi level. Thus, the index of the VHs (either of the valence or conduction band) nearest to the Fermi level is 1 and, accordingly, the band gap energy of a semiconducting SWNT is denoted by E_{11}.

Optical selection rules restrict optical transitions from the valence band v_i to the conduction band c_j (or vice versa) to those where $(i-j)=0$ or $(i-j)=\pm 1$ related to light polarized parallel or perpendicular to the nanotube axis, respectively. Transitions involving the first two valence (v_1, v_2) and conduction subbands (c_1, c_2) are depicted in Figure 2.9a. However, a depolarization effect strongly suppresses transverse interband transitions given by $(i-j)=\pm 1$ [30]. As a result, optical transitions E_{ii} associated with a parallel light polarization are predominant, whereas transitions like E_{12} or E_{21} may be neglected due to their significantly weaker coupling to the electric field [31]. By linear approximation of Equations 2.13 and 2.12 near the K point, the band gap energies of semiconducting SWNTs can be written as follows [33]:

$$E_{11}(d_t) \approx \frac{2a_{C-C}\left|\gamma_0\right|}{d_t}. \tag{2.15}$$

However, curvature effects and C–C bond length optimization lead to significant deviations from the simple scaling behavior in Equation 2.15 especially for small-diameter SWNTs. For a more reliable prediction of the optical transition energies, Weisman and Bachilo provided empirical formulas [32] for E_{11} and E_{22} as a function of chirality (n,m). Figure 2.9b depicts the so-called Kataura plot which relates the optical transition energies to the nanotube diameters [34].

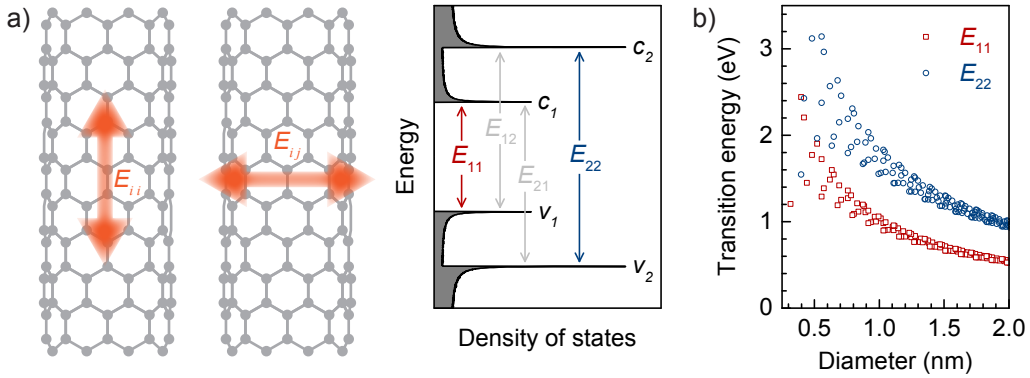

Figure 2.9: a) Optical transitions E_{ij} between the first two Van Hove singularities of the valence (v_1, v_2) and the conduction band (c_1, c_2) of a semiconducting single-walled carbon nanotube. Due to a depolarization effect, transitions E_{ii}, involving light polarized parallel to the nanotube axis, are predominant and transitions E_{ij} ($i - j = \pm 1$), involving light polarized perpendicular to the nanotube axis, are suppressed. b) Kataura plot showing the transition energies E_{11} and E_{22} of semiconducting single-walled carbon nanotubes as a function of the nanotube diameter d_t. The band gap energy E_{11} roughly follows a $1/d_t$-dependence. Data points are predictions from the empirical fitting functions of Ref. 32.

2.2.2 Excitonic photoluminescence

The radiative recombination of electron-hole pairs after optical excitation (typically provided by a laser) is called photoluminescence (PL). However, the optical transitions described up to this point neglected the importance of many-body effects in SWNTs. Conventional bulk semiconductors (e. g. Si, Ge, and III-V compounds) exhibit excited states formed by the Coulomb attraction of an excited electron to a hole. The binding energy E_B of these bound electron-hole pairs (excitons) can be estimated by a simple hydrogen model with a reduced effective mass and the dielectric constant of the medium, and is typically on the order of ~10 meV. By comparison with the thermal energy at room temperature (~25 meV) it is evident that excitonic effects in bulk semiconductors are commonly observed only at low temperatures. In the case of SWNTs, however, the strong confinement by the quasi-1D structure leads to an increased overlap of the electron and hole wave functions and results in a strongly increased exciton binding energy.

The first direct proof for excitonic effects in SWNTs was demonstrated by two-photon fluorescence excitation spectroscopy [6, 7]. In this experimental approach SWNTs were excited via two-photon absorption around half the first interband transition energy to detect the energy of the subsequently emitted photon. In the single-particle picture, all optical transitions are related to band-to-band transitions. In this case, the two-photon absorption threshold would occur at an energy of $h\nu = E_{11}/2$ and would be followed by subsequent emission of a photon from the band edge (Figure 2.10a). In the exciton picture, however, two-photon absorption should be observed at an excited exciton level that is higher in energy than the emitted photon (Figure 2.10b) which can be understood by the different wave function symmetries of the involved states [6, 7]. Figure 2.10c depicts the experimental result of the two-photon excitation spectra of SWNTs as a contour plot. The color-coded fluorescence intensity is shown as a function

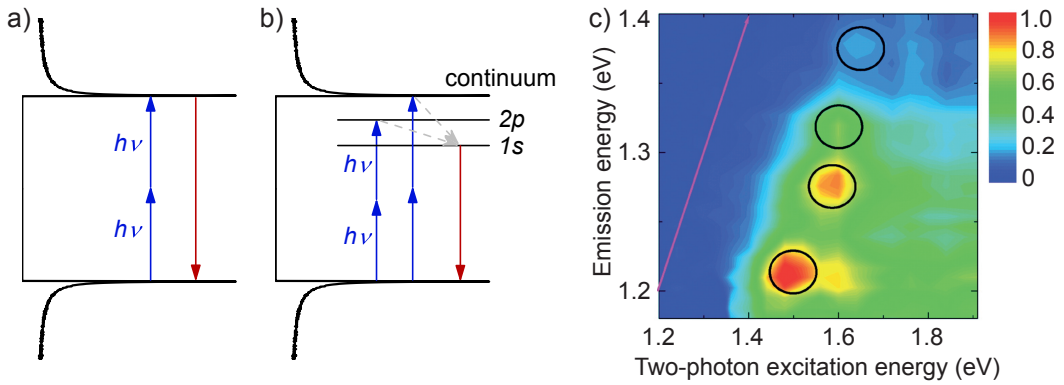

Figure 2.10: Schematic of the single-walled carbon nanotube density of states and a two-photon absorption process (blue arrows) followed by one-photon emission (red arrow) in a) the single-particle picture and in b) the exciton picture. c) False-color representation of the fluorescence emission intensity as a function of the two-photon excitation energy and the fluorescence (one-photon) energy. The emission peaks of various single-walled carbon nanotube species (indicated by the black circles) are below the two-photon excitation energy. The red solid line describes equal excitation and emission energies. Adapted from Ref. 6.

of the two-photon excitation energy and the one-photon emission energy. Black circles mark the fluorescence peaks of different SWNT chiralities. The peaks are red-shifted significantly from the red solid line defining equal excitation and emission energies, thereby providing evidence for strong excitonic effects in CNTs. The deduced values for the binding energies E_B are of the order of a few hundred millielectronvolts [6, 7, 35] making SWNT excitons stable and observable even at room temperature.

The two degenerate valleys around the K and K' points of the first Brillouin zone and the twofold degeneracy of spin for electrons and holes yield a total of 16 exciton states that are classified into four singlets and 12 triplets [36]. Because triplet states have a non-zero net spin they are optically inactive (dark). Due to Coulomb interactions, the two intravalley states among the remaining four singlets split into bonding and antibonding states, i. e. $\frac{1}{\sqrt{2}}\left(|KK\rangle \pm |K'K'\rangle\right)$.[4] The lowest energy singlet level $\frac{1}{\sqrt{2}}\left(|KK\rangle - |K'K'\rangle\right)$ is optically forbidden due to even parity and zero angular momentum, and is referred to as *the dark exciton*. The second lowest singlet state $\frac{1}{\sqrt{2}}\left(|KK\rangle + |K'K'\rangle\right)$, however, is of odd parity and has zero angular momentum, and is optically allowed (bright). The two degenerate intervalley states, $|KK'\rangle$ and $|K'K\rangle$, are also optically inactive due to non-zero angular momentum. Figure 2.11 depicts the energy dispersions of singlet excitons in a $(9,4)$ SWNT.

Additional to the increased electron-hole attraction the enhanced Coulomb interaction in SWNTs also leads to an increased electron-electron repulsion that expands the

[4] The following notation is used here: The exciton wave function of an electron in valley ν and spin ς and a hole in valley ν' and spin ς' is given by $|(\nu,\varsigma)(\nu',\varsigma')\rangle$, where $\nu,\nu' = K$ or K', and $\varsigma,\varsigma' = \uparrow$ or $\downarrow$. The four singlet states are then given by $|\nu,\nu'\rangle = \frac{1}{\sqrt{2}}\left[|(\nu,\uparrow)(\nu',\uparrow)\rangle + |(\nu,\downarrow)(\nu',\downarrow)\rangle\right]$ from which the two intravalley states $|KK\rangle$ and $|K'K'\rangle$ split into the bonding and antibonding states $\frac{1}{\sqrt{2}}\left(|KK\rangle \pm |K'K'\rangle\right)$.

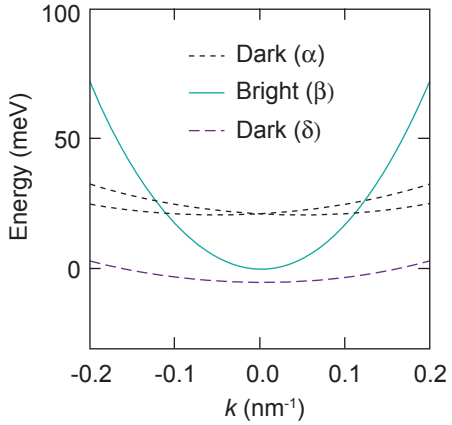

Figure 2.11: Singlet exciton energy bands for a (9,4) carbon nanotube. Finite angular momentum bands (α) and the zero angular momentum state of even parity (δ) are dark. The odd parity zero angular momentum state (β) is the only optically active state. Adapted from Ref. 37.

single-particle band gap. As a result, the lowest optical transition energy E_{opt} can be expressed by [38]

$$E_{\mathrm{opt}} = E_{11} + E_{\mathrm{BGR}} - E_{\mathrm{B}} \,. \tag{2.16}$$

It turns out that the band gap renormalization energy E_{BGR} is only slightly larger than E_{B}. Thereby, they almost compensate each other and leave E_{opt} near the level E_{11} [39]. Owing to this fact and for the sake of simplicity, the notation E_{11} will refer to the bright excitonic transition from now on and throughout this thesis.

For investigation of their photophysical properties, CNTs need to be isolated. This is owed to the fact, that nanotubes tend to form aggregates by virtue of strong van der Waals interaction and emission from bundled SWNTs is drastically weakened by rapid energy transfer from semiconducting SWNTs to metallic or smaller band gap semiconducting SWNTs [40–42]. To overcome this limitation, O'Connell *et al.* developed an effective method for unbundling of raw CNT material from a bulk synthesis process [43]. Their technique comprises the dispersion of individual CNTs in an aqueous solution of sodium dodecyl sulfate by sonication and subsequent ultracentrifugation to remove residual bundles. Similar approaches for unbundling make use of other surfactants [44–46], DNA [47], or aromatic polymers [48]. Controlled deposition of surfactant-coated CNTs from the aqueous solution onto a surface allows PL spectroscopy at the single SWNT level [49].

However, owing to the quasi-1D nanotube structure, the excited excitons are confined to the SWNT surface making them particularly sensitive to the surrounding such as the surfactant [50, 51] or dielectric medium [52, 53], charges [54–56] and molecules [57, 58]. Therefore, nanotube isolation from both other CNTs and the environment is particularly interesting for the study of intrinsic SWNT photophysics and can be achieved by direct growth of individual SWNTs across pillars using chemical vapor deposition (CVD) [59–61].

To account for the dielectric environment of a SWNT the scaling of both contributions to the optical transition energy, E_{B} and E_{BGR}, with respect to the dielectric function ε

of the medium has to be considered. The theoretical model by Walsh *et al.* yields a scaling of the binding energy as $\varepsilon^{-1.2}$ [38, 62], whereas the band gap renormalization scales as ε^{-1} [39].[5] Experimental studies of CNTs in different dielectric environments have shown that the optical transition energy exhibits a red-shift with an increase of the dielectric constant of the surrounding medium [53, 62, 64].

In the following, some of the aspects of the CNT structure and photophysics will be revisited in the context of experimental results that are presented in Chapters 4, 5, 6, and 7. First, however, the experimental setup and the various detection devices for optical studies of individual CNTs will be detailed in the next chapter.

[5] Perebeinos *et al.* have found a scaling of the binding energy as $\varepsilon^{-1.4}$ for dielectric values $\varepsilon \gtrsim 4$ [63].

Chapter 3

Experimental setup for optical spectroscopy of individual carbon nanotubes

In this chapter the setup of a home-built confocal microscope for carbon nanotube spectroscopy is described. The microscope system allows nanometer precise positioning of the sample for photoluminescence studies at ambient conditions or—when placed in an inert helium gas atmosphere—also at the temperatures of liquid nitrogen (77 K) and liquid helium (4.2 K). In combination with the used light detection devices and measurement systems, the confocal microscope provides means to study the near-infrared optical emission of individual carbon nanotubes in terms of optical spectra, photoluminescence decay dynamics, and second-order coherence.

3.1 The cryogenic confocal microscope

Optical excitation of CNTs studied with the confocal microscope was provided by a titanium-sapphire laser[1] that is tunable in wavelength in the range of 725–1000 nm and was either operated in continuous wave (cw) or pulsed mode[2]. The output power of the laser was stabilized by double-passing the beam through an acousto-optic modulator. A detailed description of the stabilization setup can be found in Ref. 65. The laser beam was coupled into an optical single-mode fiber that guided the excitation light to the horizontal side-arm of the microscope (Figure 3.1). Here, the beam was collimated and passed through a shortpass filter to block Raman scattered photons from the fiber. The following beam sampler split the laser beam with a 90/10 ratio for the incident *s*-polarization[3] that was adjusted by a 3-paddle fiber polarization controller. The transmitted 90 % of the beam was focused onto a photodiode that monitored the laser intensity as a reference signal for the laser stabilization controller while the reflected 10 % served as the excitation light. The polarization state of the excitation beam (which is linearly polarized after reflection) was adjusted by a half-wave plate ($\lambda/2$) that was variable in orientation and an optional quarter-wave plate ($\lambda/4$). During the course of the experiments presented in this thesis, two sets of focusing elements were used. The first was an aspheric lens[4] with a numerical aperture of 0.68. Later, a near-infrared apochromatic objective[5] (numerical aperture: 0.75) suitable for cryogenic temperatures and with a flat focal displacement curve within the wavelength range ~700–1000 nm was available. Piezo-slip-stick-steppers[6] and piezo-scanners[7] allowed positioning of the sample in the three spatial directions (x,y,z). A photodiode below the sample was used for monitoring the transmitted laser intensity. The focusing lens/objective, the sample, and the piezo-stack were mounted inside a tube that was evacuated to a pressure $<8{\cdot}10^{-5}$ mbar and subsequently filled with helium gas to ~20 mbar to provide thermalization with the liquid nitrogen (77 K) or liquid helium (4.2 K) bath for cryogenic operation. Reflected laser light as well as the emitted PL from the sample was collected by the objective and passed to the upper part of the microscope, denoted as the vertical collection arm. Here, a second beam sampler reflected part of the light to a charge-coupled device (CCD) camera used for imaging the focal spot or sample surface for alignment purposes and coarse orientation on the sample. The transmitted beam from the beam sampler was filtered from reflected laser light by a longpass filter before it was coupled into an optical single-mode fiber that guided the light to the photodetection devices. The longpass filter and the shortpass filter from the excitation arm were selected in opposing combinations (i. e. same cut-on and cut-off wavelengths, respectively) to efficiently suppress the excitation laser. Used filter cut-on and cut-off wavelengths were 860 nm, 900 nm, and 950 nm.

[1] *Coherent* Mira 900 pumped by a Verdi-V10 laser diode
[2] repetition rate: 76.0 MHz, pulse duration: ~200 fs
[3] The beam sampler reflects 1–10 % of the incident beam depending on the light's polarization: at an angle of incidence of 45°, ~1 % reflection is for *p*-polarization and ~10 % for an *s*-polarized beam
[4] *Thorlabs* C330TM-B, focal length: 3.1 mm, numerical aperture: 0.68
[5] *attocube systems* LT-APO/NIR/075
[6] *attocube systems* ANPx101 (2×) and ANPz102
[7] *attocube systems* ANSxy100

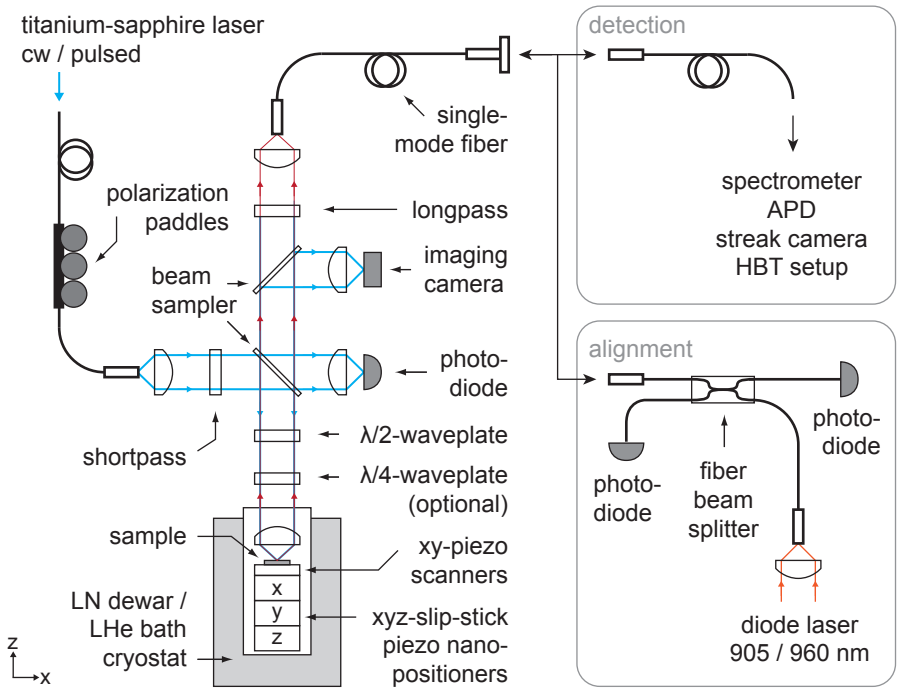

Figure 3.1: Schematic of the cryogenic confocal microscope setup. A single-mode fiber equipped with a 3-paddles fiber polarization controller guides the light of the titanium-sapphire laser, operated in either continuous wave (cw) or pulsed mode, to the excitation arm of the microscope. A beam sampler transmits 90 % of the laser beam to a photodiode for the laser power stabilization loop while the other 10 % are reflected to the sample. A variable half-wave plate ($\lambda/2$) and an optional quarter-wave plate ($\lambda/4$) allow polarization control of the laser light. The sample is mounted beneath the focusing objective on a piezo-stack for xyz-positioning inside a sealed tube filled with helium gas for thermalization with the surrounding liquid nitrogen (LN) or liquid helium (LHe) bath. A small fraction of the collected light from the sample is reflected by another beam sampler at the top part of the microscope and is used for imaging with a CCD camera while the transmitted fraction passes a longpass filter before it is coupled into a single-mode fiber. The fiber is either connected to a small alignment setup consisting of a fiber beam splitter with two photodiodes and a diode laser, or to the photodetectors and measurement systems: a grating spectrometer, an avalanche photodiode (APD), a streak camera, or a Hanbury Brown and Twiss (HBT) setup.

For alignment purposes of the microscope, the end of the optical fiber from the collection arm was plugged to a port of a fiber beam splitter whose other ends were attached to a diode laser of either 905 nm or 960 nm and two photodiodes. Operation of this small setup was as follows: The diode laser beam was coupled into the microscope at a fixed power monitored by the signal from the first photodiode. The reflected power from the sample was then captured by the second photodiode at the other output of the fiber beam splitter and was maximized by beam alignment and focal plane adjustment with the z-directional piezo-stepper.

3.2 Spatial resolution of the confocal microscope

The spatial resolution of the confocal microscope was determined by measuring the transmitted laser power through a grating of 10 µm periodicity. The grating was placed in the focal plane of the microscope and translated laterally in x-direction while recording the transmission signal $\mathcal{T}$ using the photodiode underneath the sample. The obtained signal is a convolution of the Gaussian beam profile and the transmission function of the grating approximated by a rectangular step function. By taking the derivative $d\mathcal{T}/dx$ and performing Gaussian fits, the experimental spot size is obtained by the average of the Gaussians' full width at half maximum (FWHM) linewidth. Figure 3.2 depicts an optical micrograph of the grating as well as the transmission data, its derivative, and the Gaussian fits for a laser wavelength of 940 nm and the apochromatic objective. A spot size of 1.1 µm was deduced from the fit function (red curve in Figure 3.2). The same value has been obtained with the aspheric lens [65], however, without the apochromatic correction for different wavelengths.

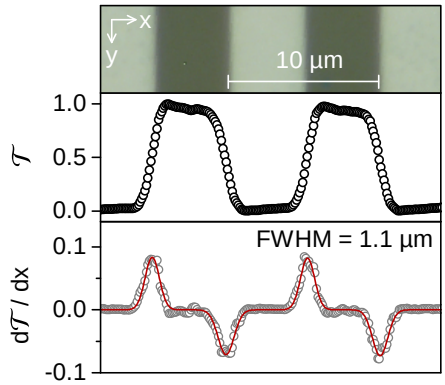

Figure 3.2: Top panel: Optical micrograph of the stripe patterned grating with a periodicity of 10 µm. Bright regions are highly reflective, dark regions are transparent. Middle panel: Normalized transmission $\mathcal{T}$ of the laser (940 nm wavelength) through the grating as a function of lateral displacement in x-direction measured with the low-temperature apochromatic objective. Bottom panel: Derivative $d\mathcal{T}/dx$ of the corresponding transmission signal. The spatial resolution is determined by the average full width at half maximum (FWHM) of the Gaussian fits (red curve) as 1.1 µm.

3.3 Photodetection devices and setups

3.3.1 Acquisition of optical spectra

For spectral dispersion of the PL or Raman signals, a grating monochromator[8] with an attached liquid nitrogen cooled Si-based CCD array[9] was used. While offering low-noise characteristics, the CCD is limited in spectral sensitivity by its vanishing quantum efficiency in the near-infrared with a lower detection boundary at ~1.18 eV (equivalent to an upper detection boundary at ~1050 nm in terms of wavelengths). Depending on the chosen grating of the monochromator, either 300 grooves/mm or 1200 grooves/mm, a spectral resolution of ~220 µeV or ~40 µeV was achieved, respectively.

3.3.2 Second-order photon correlation measurements

A so-called Hanbury Brown and Twiss (HBT) setup enables testing the temporal coherence properties of spatially coherent light. To this end, a stream of photons is directed onto two single-photon counting detectors by a 50:50 beam splitter. The generated photocurrent pulses are used as start/stop signals for a time-correlated single photon counting module that records the time that elapses between two successive start and stop pulses. For a quantitative analysis of the results it is instructive to introduce the second-order photon correlation function

$$g^{(2)}(\tau) = \frac{\langle n_1(t)\, n_2(t+\tau)\rangle}{\langle n_1(t)\rangle \langle n_2(t+\tau)\rangle}\,, \tag{3.1}$$

where $n_i(t)$ is the number of photon counts on detector $i = 1,2$ at time t, and $\langle ...\rangle$ indicates the time average. Based on the value of $g^{(2)}$ at zero time delay $\tau = 0$, one can make the following classifications of light:

- coherent light: $g^{(2)}(0) = 1$,
- bunched light: $g^{(2)}(0) > 1$,
- antibunched light: $g^{(2)}(0) < 1$.

It can be shown that coherent light shows Poissonian photon statistics where the photons are randomly distributed within the light beam [66]. Hence, after a start pulse at $t = 0$ it is equally likely to obtain a stop pulse at all times τ and $g^{(2)}(\tau) = 1$. The definition of bunched light, $g^{(2)}(0) > 1$, then indicates that there is a higher probability for detecting a stop pulse at short times, meaning that the photons arrive, as the name suggests, in bunches. In the case of antibunched light, the photons arrive with regular and long time intervals between them. Due to these large gaps between successive photons, the probability of detecting a stop pulse at small time delays τ is decreased and $g^{(2)}(0) < 1$. As a result, a dip in the second-order correlation function at zero time delay, $\tau = 0$, is a manifestation of a single-photon source. The observation of photon antibunching has no classical interpretation and is only explained by the quantum nature of light.

[8] *Princeton Instruments* Acton SP2500, later replaced by SP750i
[9] *Princeton Instruments* Spec-10, later replaced by PyLoN:100BR, 1340×100 imaging array

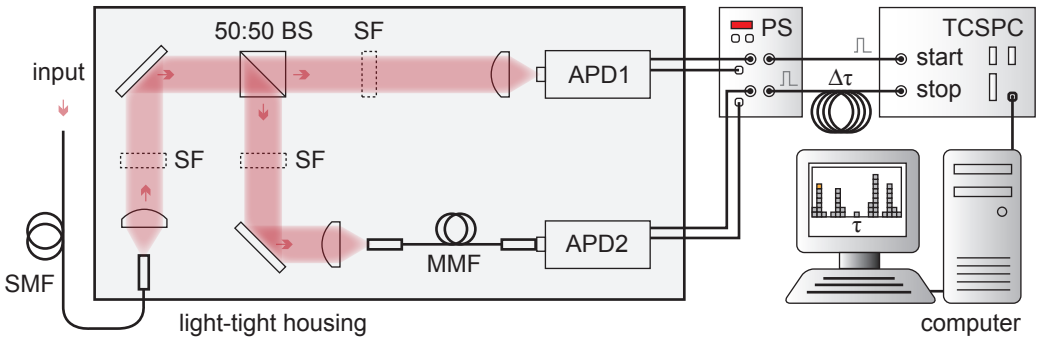

Figure 3.3: Schematic of the HBT setup. The input light is uncoupled from the single-mode fiber (SMF) and split by a 50:50 beam splitter (BS). Spectral filters (SF) can be optionally placed in the beam path to block non-photoluminescence photons. The transmitted light from the BS is directly focused onto the single photon counting avalanche photodiode APD1 while the reflected light is coupled into a multi-mode fiber (MMF) connected to APD2. The generated TTL pulses are fed via the APDs' power supply (PS) into the start and stop inputs of the time-correlated single photon counting module (TCSPC). The signal from APD2 is delayed by a time $\Delta\tau$. The measurements of the time between successive start and stop events are read out by a computer and stored to accumulate a histogram.

The experimental realization of the HBT experiment is depicted schematically in Figure 3.3. A single-mode optical fiber guided the collected PL from the detection arm of the microscope (see Section 3.1) to the inside of the HBT setup's light-tight housing that protects the high-sensitivity photodetectors from ambient light. The PL photons were uncoupled from the fiber and directed by a mirror to a 50:50 beam splitter. The transmitted light was directly focused onto the active area of a silicon-based single-photon counting APD[10] whereas the reflected part from the beam splitter was coupled into a multi-mode optical fiber that was plugged to the fiber receptacle of the second APD. The multi-mode fiber layout was chosen due to its significant reduction of cross-talk between the two APDs [65]. Spectral longpass or bandpass filters were optionally placed in the light beam to block non-PL photons. The output pulses of both APDs were passed through the APDs' power supply[11] and fed into the start and stop inputs of a time-correlated single photon counting system[12]. The electrical pulse from the second APD was delayed by an elongated copper cable. Thereby the simultaneous detection of two photons at both APDs is effectively shifted from zero time delay to a value $\Delta\tau$ determined by the elongation of the copper cable.

The HBT experiments were performed using either cw or pulsed laser excitation of the PL emitter. For cw excitation of a single-photon source the resulting histogram of the time delay τ between successive start and stop pulses shows a dip at $\tau = 0$. If the source is excited by laser pulses at a repetition rate $1/\tau_{\mathrm{rep}}$ with $\tau_{\mathrm{rep}} \gg \tau_{\mathrm{PL}}$, where τ_{PL} is the PL lifetime, the recorded histogram will consist of peaks equally spaced by the laser pulse separation τ_{rep}; however, with a missing peak at $\tau = 0$ for antibunched light.

[10] *Perkin Elmer* SPCM-AQRH-15
[11] *PicoQuant* DSN 102
[12] *PicoQuant* PicoHarp 300

3.3.3 Time-resolved photoluminescence measurements

Time-resolved PL measurements on the scale of nanoseconds were performed with the single photon counting avalanche photodiode APD1 of the HBT setup (cf. Figure 3.3) with the 50:50 beam splitter being removed from the beam path. Start pulses to the time-correlated single photon counting module were provided by the signal of a photodiode that detected the pulses of the mode-locked titanium-sapphire oscillator while the stop pulses were defined by the output of APD1. The repetitive measurement of the time delay between excitation pulse and detection pulse accounts for the statistical nature of the emission and provides the PL decay curve as a plot of the PL intensity versus time.

Decay times down to a few picoseconds were measured by a streak camera[13] that converts the time variation of the PL photons with respect to the laser pulses into a spatial profile on the detector.

Equipped with these techniques, individual CNTs were studied at room and cryogenic temperatures by means of spatial PL mapping, PL and photoluminescence excitation (PLE) spectroscopy, as well as PL decay and second-order coherence measurements. The investigated material systems include micelle-encapsulated CNTs (Chapters 6 and 7) as well as unprocessed CNTs grown with an in-house chemical vapor deposition setup to be discussed in the next chapter.

[13] *Hamamatsu* C5680

Chapter 4

Growth of small-diameter carbon nanotubes by chemical vapor deposition

The aim of the work presented in this chapter was to establish growth of small-diameter single-walled carbon nanotubes by catalytic chemical vapor deposition for optical studies. The reactor setup, the catalyst composition, and the impact of various growth parameters on nanotube lengths, areal density, and diameters are described. Further, optical investigation by cryogenic Raman spectroscopy was used to study the structural quality of the synthesized carbon nanotubes.

PARTS OF THIS CHAPTER ARE BASED ON THE PUBLICATION

Matthias S. Hofmann, Jonathan Noé, Manuel Nutz, Alexander Kneer, Raphael Dehmel, Lilian Schaffroth, and Alexander Högele. Synthesis and cryogenic spectroscopy of narrow-diameter single-wall carbon nanotubes, *Carbon* **105**, 622–627 (2016).

4.1 Introduction

A premise for the research on the intrinsic photophysical properties of carbon nanotubes is the material quality. Elaborated synthesis techniques for nearly defect-free, so called ultra-clean, CNTs have been developed over the years but optical investigations are often impeded by the need of highly-sensitive photodetectors in the near-infrared photoluminescence emission range. Silicon-based detectors offer an appropriate solution in terms of low-noise and high quantum-yield. But owing to their spectral sensitivity window they are limited to the study of few CNT chiralities with subnanometer diameters. However, most synthesis methods for CNTs are neither chirality-selective nor do they yield abundant CNTs with subnanometer diameters and corresponding PL emission wavelengths below 1050 nm. The limited control of diameter-specific CNT growth is primarily a consequence of the complex interplay of the numerous synthesis parameters in catalytic CVD such as catalyst composition, size and pretreatment, carbon precursor, additives, temperature, or substrate support. Although this complexity has impeded a thorough microscopic understanding of the details involved in the CNT synthesis, remarkable progress has been achieved in the structural control of CNTs by means of catalyst design [67, 68]. Variation of catalytic metals explored in other studies indicated that SWNTs with subnanometer diameters can be preferentially obtained under appropriate growth conditions [69–75]. In the following, the results of catalytic CVD aiming at realizing as-grown narrow-diameter CNTs for optical spectroscopy are presented.

4.2 Chemical vapor deposition

4.2.1 Basic principles

In general, CVD is the process of chemical reactions or decompositions of volatile precursors to form a solid product on a substrate. The main advantages of the CVD synthesis of CNTs over methods like laser ablation and arc discharge lie in its relatively low cost, its easy implementation, the control of growth conditions, and the possibility of localized and well separated growth on a substrate [76]. For the catalytic CVD method, nanoparticles usually made of a transition metal like Fe, Ni, or Co are used to catalyze the decomposition of a carbon-bearing gas like methane [70], ethylene [77], carbon monoxide [78], or ethanol [79] at reaction temperatures of typically 600–1000 °C.

A commonly accepted model for the growth of CNTs from metallic catalyst particles is the vapor-liquid-solid (VLS) mechanism which has originally been developed for the growth of silicon whiskers [80] and was proposed later for the growth of carbon filaments [81, 82]. Adapted to the nucleation of CNTs, the VLS mechanism suggests catalytically driven decomposition of the carbon-bearing precursor gas at the metallic catalyst nanoparticle in the form of a liquid droplet[1]. The released carbon atoms diffuse into the metal until the particle gets supersaturated and precipitates the dissolved carbon as a fullerene-like cap that grows further to a CNT as depicted in Figure 4.1. Both the

[1] The assumption of liquid catalyst particles at standard CVD temperatures in the range of 600–1000 °C is largely justified by the abrupt decrease of the melting temperature of metallic particles below 10 nm [83].

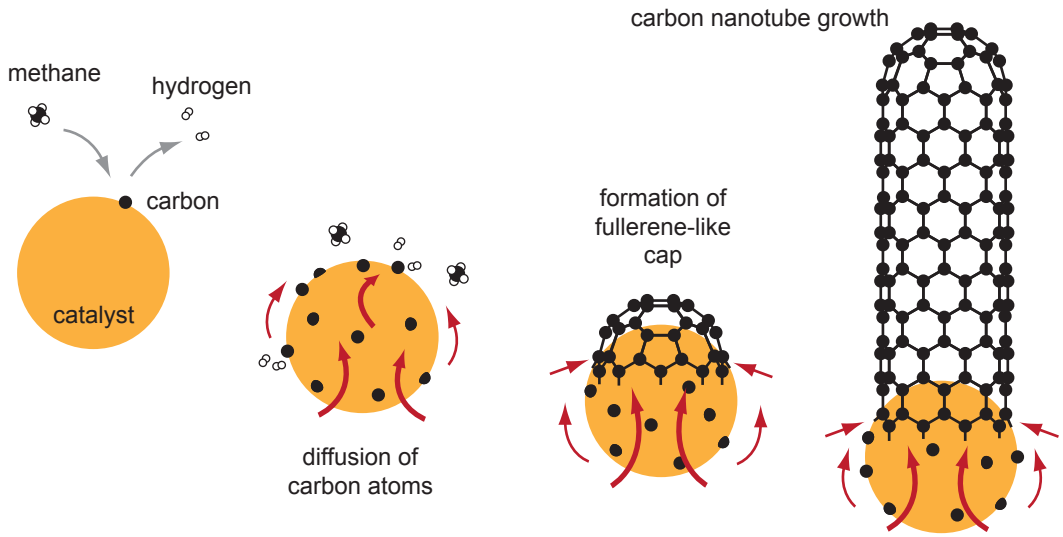

Figure 4.1: Schematic evolution of carbon nanotube growth from a catalyst particle by chemical vapor deposition using methane as the carbon feedstock. The precursor gas is catalytically dissociated at the metallic nanoparticle. The deposited carbon atoms diffuse into the catalyst particle until it is supersaturated. Carbon is precipitated to the surface where it nucleates to a fullerene-like cap and finally grows to a carbon nanotube.

initial cap formation and the CNT growth have been observed *in situ* by transmission electron microscopy (TEM) [84, 85]. Furthermore, it has been shown that the diameter of the CNT can be determined by the size of the catalyst particles [86, 87].

However, even though there is experimental support for CNT synthesis by the VLS mechanism [88], several groups reported CNT growth from crystalline catalyst particles [84, 85, 89–91] which is more in favor of a vapor-solid-solid (VSS) mechanism. Besides the open questions regarding the physical state of the catalyst, many other details such as the mechanisms of CNT nucleation and defect integration still remain controversial, leaving a precise understanding of the synthesis mechanism of CNTs still pending [92].

The CVD method allows choice and control over several process parameters such as catalyst, carbon precursor, temperature, reaction time, gas flow rate, or pressure that all effectively influence the characteristics of the synthesized CNTs. On the other hand, the numerous list of parameters makes the controlled growth of CNTs a demanding task.

4.2.2 Carbon precursor and catalyst

The main objectives for the growth of SWNTs for single nanotube PL spectroscopy with highly efficient and low noise silicon-based photodetectors are the following: first, the contamination by amorphous carbon is to be avoided, since it significantly reduces the carbon nanotube quality or may even poison the catalyst particles during CNT synthesis. Amorphous carbon is mainly deposited by self-pyrolysis of the carbonaceous gases at the elevated temperatures in the reaction chamber of the CVD furnace. By choosing methane as the carbon feedstock for nanotube synthesis, amorphous carbon

contamination is diminished due to methane's kinetic stability [70] and molecular decomposition is primarily assisted by the catalyst particles. Further, additional hydrogen gas has been shown to reduce amorphous carbon deposition and promote the growth of clean CNT samples [93]. Second, control of the nanotube density is crucial: It should be low enough to ensure single SWNTs within the focal spot of ~1 µm of the confocal microscope used for PL measurements (Section 3.1), but also high enough to locate individual nanotubes in an appropriate amount of time when scanning the sample. The main approach to tune the density is by varying the amount of deposited catalyst particles on the sample surface. Thirdly, since the detection window's lower (upper) boundary of the employed silicon-based photodetectors is at ~1.18 eV (~1050 nm), the distribution of SWNT diameters has to be centered around $\lesssim$1 nm to ensure a large fraction of wide band gap SWNTs that emit in the detector's sensitivity range.

The realized CVD method is based on methane and hydrogen in the presence of a bimetallic iron-ruthenium (FeRu) catalyst that has been reported to promote the synthesis of small-diameter SWNTs due to the temperature-stable formation of small catalytic FeRu alloy nanoparticles [72]. The FeRu catalyst was prepared from three stock solutions consisting of iron(III) nitrate nonahydrate[2] ($Fe(NO_3)_3{\cdot}9H_2O$), ruthenium(III) chloride hydrate[3] ($RuCl_3{\cdot}xH_2O$), and alumina (Al_2O_3) nanopowder[4] each dissolved in isopropyl alcohol with concentrations of 4.65 g/l, 1.40 g/l, and 1.50 g/l, respectively. The solutions were stirred over night before small amounts were mixed together and diluted with isopropyl alcohol to obtain a catalyst solution with the following ingredient concentrations[5]:

- $Fe(NO_3)_3{\cdot}9H_2O$: 116.1 mg/l
- $RuCl_3{\cdot}xH_2O$: 35.0 mg/l
- Al_2O_3 nanopowder : 37.5 mg/l

This catalyst solution is termed as having a concentration of 1:1 and was used as the basis for further diluted solutions. For example, a 1:1 catalyst solution was obtained by mixing 54 µl of each stock solution with 2 ml isopropyl alcohol. To obtain a concentration of 1:5 the volume of isopropyl alcohol is increased five-fold, i. e. 54 µl of each stock solution are mixed with 10 ml isopropyl alcohol.

4.2.3 Setup and growth procedure

A schematic of the home-built CVD reactor used for CNT synthesis is depicted in Figure 4.2. The used gases for the CVD process were methane (CH_4), hydrogen (H_2), and an Ar/H_2 mixture (95 % argon and 5 % hydrogen) that was used as an inert gas during heating and cooling periods of the CVD furnace. Pressure regulators set the output pressure of each gas cylinder to the same value of 3 bar. The cylinders containing the highly flammable reaction gases methane and hydrogen were stored in a safety gas cylinder

[2] *Sigma-Aldrich* 254223-10G
[3] *Sigma-Aldrich* 463779-10G
[4] *Sigma-Aldrich* 551643-10G
[5] based on Ref. 94 and private communications with Martin Weiss and Christian Schönenberger from the University of Basel

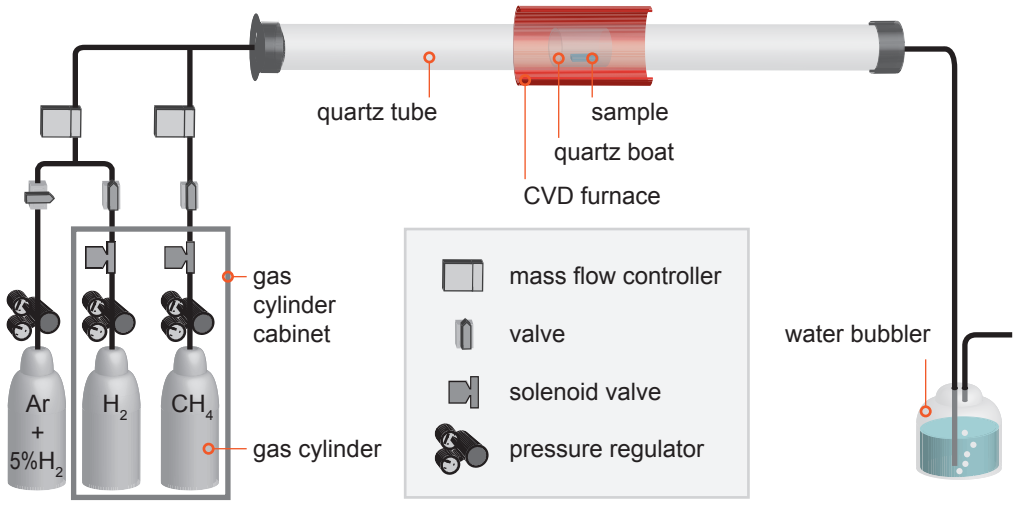

Figure 4.2: Schematic of the chemical vapor deposition setup for carbon nanotube synthesis. Flow rates are adjusted by digital mass flow controllers. For safety reasons the highly flammable gases methane (CH_4) and hydrogen (H_2) are kept in a gas cylinder cabinet and are secured with solenoid valves. The catalyst patterned sample sits inside a small quartz boat in the middle of the CVD furnace. A water bubbler prevents ambient air from diffusing into the reaction chamber and indicates possible leakage.

cabinet and were additionally secured by solenoid valves. The gas flow rates were set by digital mass flow controllers[6] before entering the CVD reaction chamber which consisted of a quartz tube (length: 130 cm, inner diameter: 32 mm, wall thickness: 2 mm) passing through a horizontal tubular furnace[7] that supplied the thermal energy for the catalytic reaction for CNT growth. The exhaust gas was passed through a water bubbler in order to prevent ambient air from diffusing into the reaction chamber. Furthermore, the bubbler acted as an indicator for possible leaks in the system.

Before starting the CNT growth procedure the FeRu suspension was bath-sonicated[8] for 2 hours. The catalyst was deposited onto the 100 nm thick oxide layer of a silicon substrate by spin coating a droplet of the FeRu suspension at 4000 rpm for 40 s. Subsequently, the samples with the nanometer-sized catalyst particles were transferred to the CVD reaction chamber by sliding a small quartz boat to the middle of the furnace from the rear end of the quartz tube. After closing the system, the furnace was heated to the growth temperature at an inert flow rate of 1.5 standard liters per minute (slm) of Ar/H_2. When the growth temperature was reached, the tube was flushed with hydrogen at 1.0 slm for 5 minutes to reduce the catalyst particles. Subsequently, methane and hydrogen with a CH_4/H_2 flow rate ratio of 1.33 were fed into the reactor for CNT synthesis. Under these conditions the growth was maintained for 10 minutes. Afterwards, the supply of CH_4 was stopped and the samples were gradually cooled in a hydrogen flow at 0.5 slm. At a temperature of $\lesssim$500 °C hydrogen was replaced by the Ar/H_2 mixture. Finally, the samples were unloaded at a furnace temperature of approximately 300 °C.

[6] *Sevenstar* D07-19B and D08-2F
[7] *Nabertherm* R40/500/12-B170
[8] *Bandelin* Sonorex Super

4.3 Influence of synthesis parameters on carbon nanotube growth

This section presents the results of the CNT growth process in terms of the areal density, the nanotube lengths, and diameters. Sample analysis was conducted using scanning electron microscopy (SEM) and atomic force microscopy (AFM).

4.3.1 Areal density: influence of temperature and gas flow rate

The following analysis concerns the influence of different synthesis temperatures and methane flow rates on the CNT density. As mentioned earlier, the main control parameter for the CNT density was the initial concentration of the catalyst solution. For a given catalyst solution, however, the CNT density also varied with the growth temperature. CNT synthesis was performed at furnace temperatures from 700 °C to 850 °C in steps of 50 °C and methane flow rates of 0.16 slm, 0.37 slm, 0.58 slm, and 1.0 slm at a methane/hydrogen flow rate ratio of 1.33 and a catalyst concentration of 1:3. The CNT density was determined with SEM[9]. The micrographs were acquired with the system's *Inlens* detector and a low acceleration voltage of 0.7 kV to achieve high contrast and CNT visibility [95, 96]. For each sample of the distinct growth processes, SEM images of equal sample area size at random positions were examined. Analysis was realized by marking each detected CNT in the scanning electron micrographs by a colored circle. The number of circles was then counted by an algorithm using MATLAB and related to the investigated area. The results are summarized in Figure 4.3. One of the main results is that the methane flow rate did not influence the mean CNT density at a given temperature within the error of data analysis (Figure 4.3a). However, for a fixed methane flow rate, the CNT density increased significantly with increasing temperature until 800 °C where it reached the point of saturation with ~14 CNTs per 100 µm^2 (Figure 4.3b). These findings indicate that the precursor-catalyst setup requires a certain thermal activation energy for efficient CNT growth which is provided for temperatures ≥800 °C. The topography image recorded by AFM in Figure 4.3c shows a (4×4) µm^2 sample area with several CNTs grown at a CVD temperature of 850 °C and a methane flow rate of 1.0 slm. It is apparent from this scan that many catalyst particles did not yield nanotubes during CVD. Therefore, the saturation regime of the CNT density in Figure 4.3b does not imply that all catalyst particles have been activated for nanotube synthesis. Low synthesis yield is a widely observed feature of catalytic CVD. For instance, results from CNT growth with well separated Ni [97, 98] or Fe [99] catalyst particles show a proportion of active catalyst particles below 20 %. Such small CNT yields are most commonly attributed to encapsulation of catalyst particles by graphitic shells observed in high resolution transmission electron microscopy [100].

[9] *Raith* e_Line

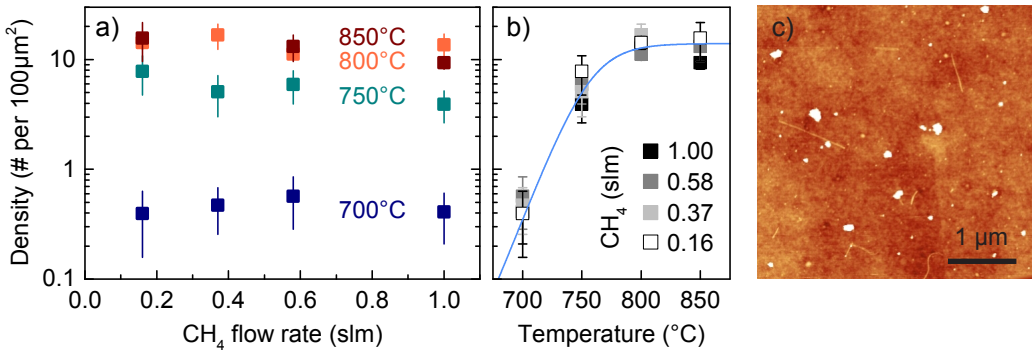

Figure 4.3: a) Carbon nanotube density as a function of the methane supply rate in standard liters per minute (slm) at temperatures of 700 °C, 750 °C, 800 °C, and 850 °C. The methane/hydrogen flow rate ratio is 1.33 for all measurements. Data points represent the mean density obtained from several scanning electron micrographs for each temperature. Error bars indicate highest and lowest densities from individual micrographs. For a given growth temperature, the nanotube density is independent of the methane flow rate within the error of data analysis. b) Carbon nanotube density as a function of growth temperature for the investigated methane flow rates. The nanotube density saturates around 800 °C. The blue line is a guide to the eye. c) Atomic force microscopy image of a 16 µm^2 sample area showing individual carbon nanotubes and several catalyst particles that remained inactive for carbon nanotube synthesis. Growth was carried out at 850 °C and a methane flow rate of 1.0 slm.

4.3.2 Length distribution: effect of oxygen plasma treatment of the catalyst

SEM was also used for determination of the length distribution of CNTs obtained with the synthesis method described above. A representative scanning electron micrograph of several CNTs grown on silicon oxide is shown in Figure 4.4a. The clearly skewed data histogram in Figure 4.4b was fitted by a log-normal distribution, which is commonly used to describe length and size distributions in chemistry and biology [101]. The corresponding probability density function reads

$$f(x) = \frac{1}{x\sigma\sqrt{2\pi}} \exp\left[-\frac{1}{2\sigma^2}\left(\log x - \mu\right)^2\right], \quad x > 0\,, \tag{4.1}$$

where x is the random variable. The point of global maximum is given by the mode, $\mathrm{Mode}[x] = e^{\mu-\sigma^2}$, whereas the median, $\mathrm{Med}[x] = e^{\mu}$, is the number that splits the upper half of the distribution from the lower half.

A mode of 0.7 µm was determined from the log-normal fit to the length data histogram in Figure 4.4b. As a measure of the occurrence of long nanotubes, the third quartile $Q_3[L]$ was evaluated. The third quartile of a data set is the value that splits the upper 25% from the lower 75%. $Q_3[L]$ for the histogram in Figure 4.4b is 1.9 µm.

The CNT length distribution increased reproducibly by exposing the alumina-FeRu catalyst particles to an oxygen plasma prior to the CVD process. The plasma was provided by a standard plasma etcher[10] operated at 2 torr and 55 W for 180 s. Figure 4.4c

[10] *LabAsh 100*

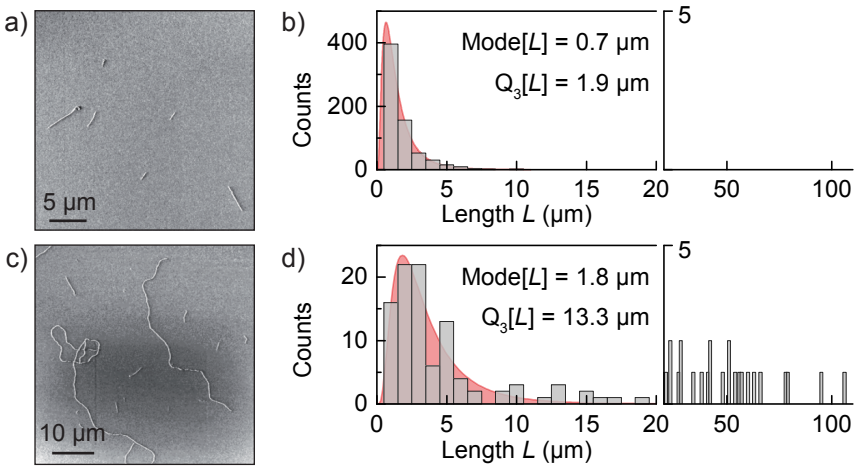

Figure 4.4: a) Scanning electron micrograph and b) length distribution of carbon nanotubes grown with the standard synthesis recipe as described in Section 4.2.3. c) Scanning electron micrograph and d) length distribution of carbon nanotubes where the catalyst particles have been exposed to an oxygen plasma prior to the chemical vapor deposition process. This catalyst pretreatment leads to increased lengths of the grown carbon nanotubes which is reflected in the values of the mode of the length distribution Mode[L] and the third quartile $Q_3[L]$.

shows CNTs with lengths of several tens to hundred micrometers that were obtained with the pretreated catalyst subjected to the same CVD synthesis process as the sample from Figure 4.4a. The evaluation of the length distribution depicted in Figure 4.4d yields a mode of 1.8 µm and a value of the third quartile of $Q_3[L]$ =13.3 µm. Similar effects have been observed for the growth of CNT forests from a Fe catalyst on an alumina support and is attributed to immobilization of the catalyst particles on the support, thereby effectively suppressing particle coarsening and bulk diffusion [102], and enhancing the catalytic lifetime.

The growth of long CNTs is particularly interesting for samples with SWNTs suspended over trenches that are wide enough to allow for background-free photophysical studies within the confocal microscope's focal spot of ~1 µm (Section 3.1). However, the obtained CNTs of a few ten micrometers in length are significantly bent (see Figure 4.4c), supposedly due to the defective incorporation of carbon 5- and 7-rings into the CNT lattice [103].

4.3.3 Carbon nanotube diameters: influence of temperature and gas flow rate

The CNT diameters were analyzed for synthesis temperatures of 750 °C, 800 °C and 850 °C and methane flow rates of 0.16 slm, 0.58 slm, and 1.0 slm (with a CH_4/H_2 flow rate ratio of 1.33). The CVD process for the analyzed samples was performed without catalyst pretreatment by oxygen plasma as discussed in Section 4.3.2. At 700 °C almost all catalyst particles remained inactive under all investigated growth conditions. As a consequence, the insufficiently large number of investigated CNTs did not yield convincing diameter

distributions.

The CNT diameters were determined by tapping mode AFM[11] in air. For this purpose the system's resolution in the vertical direction was of primary interest. The main factors of the vertical resolution are the scanner, pixelization, and the overall system noise. The resolution of the vertical scanner movement is <0.1 nm [104]. Pixelization, which here means the number of data points in the vertical direction, is determined by the conversion of 16 bits over the full vertical scanner range and can be estimated by the system's Z limit parameter as $(6.987\,\mu\text{m})/2^{16} = 0.1$ nm. The AFM noise is typically below 0.1 nm root mean square [104]. Since these errors Δd_i are statistically independent, the total error can be estimated as $\Delta d = \sqrt{\sum (\Delta d_i)^2} \leq 0.2$ nm. With regard to determination of SWNT diameters in the subnanometer range, the total error is significantly large. However, this error of a single measurement is converted into an error for the accumulated distribution composed of $\mathcal{N}$ data points that is calculated as $\Delta d_{\mathcal{N}} = \Delta d/\sqrt{\mathcal{N}}$ which turns out to be $\lesssim$0.1 nm. Therefore, the use of AFM as a tool for determining appropriate growth conditions for narrow-diameter CNTs is justified.

For CNT diameter acquisition, topography scans of several random sample areas were recorded. A representative AFM image of a $(3.5\times3.5)\,\mu\text{m}^2$ sample area is shown in Figure 4.5a. Height profiles along lines perpendicular to the nanotubes' axes were extracted by the scanning probe microscopy data visualization and analysis software *Gwyddion*. To reduce noise, the height profiles were averaged over a small range symmetrically extended perpendicular to the profile line. Figure 4.5b depicts the height profile along the dashed line that cuts the three individual CNTs marked by the arrows in Figure 4.5a. The diameters were found to be 1.3 nm, 0.7 nm, and 1.5 nm and are in accord with typical values of SWNTs.

Several AFM scans were analyzed in the same manner as described above to obtain diameter distributions from different growth temperatures at a methane flow rate 0.16 slm as exemplified in Figures 4.5c–e. Log-normal distributional fits (Equation 4.1) were used to extract the values of the median Med$[d_t]$ from the skewed diameter histograms. The median was chosen a measure of location since it is significantly more robust to outliers and a better description of central tendency than e. g. the mean. A clear trend towards narrow-diameter CNTs with increasing temperature is seen from the distributions in Figures 4.5c–e. Values for Med$[d_t]$ were 2.2 nm, 1.2 nm, and 1.0 nm for a methane flow rate of 0.16 slm and temperatures of 750 °C, 800 °C, and 850 °C, respectively. The medians for all investigated growth parameters are summarized in the bar chart of Figure 4.5f.[12] For methane flow rates of 0.16 slm and 1.0 slm the CNT diameter distributions shifted to smaller values with increasing CVD temperature. For a flow rate of 0.58 slm, however, the minimum of Med$[d_t]$ was found for 800 °C. The three minimum values of the diameter distributions' median for the three investigated methane flow rates were all determined to be 1.0 nm. Based on these results and based on the overall small values of Med$[d_t]$ for all three growth temperatures (750 °C, 800 °C, and 850 °C) at the highest investigated methane flow rate, the growth parameters for samples of further studies were chosen as 850 °C at a methane and hydrogen flow rate of 1.0 slm and 0.75 slm, respectively. Moreover, this parameter set was also found to show good reproducibility

[11] *Digital Instruments* Dimension 3100

[12] All diameter histograms and corresponding log-normal fits can be found in Appendix A.

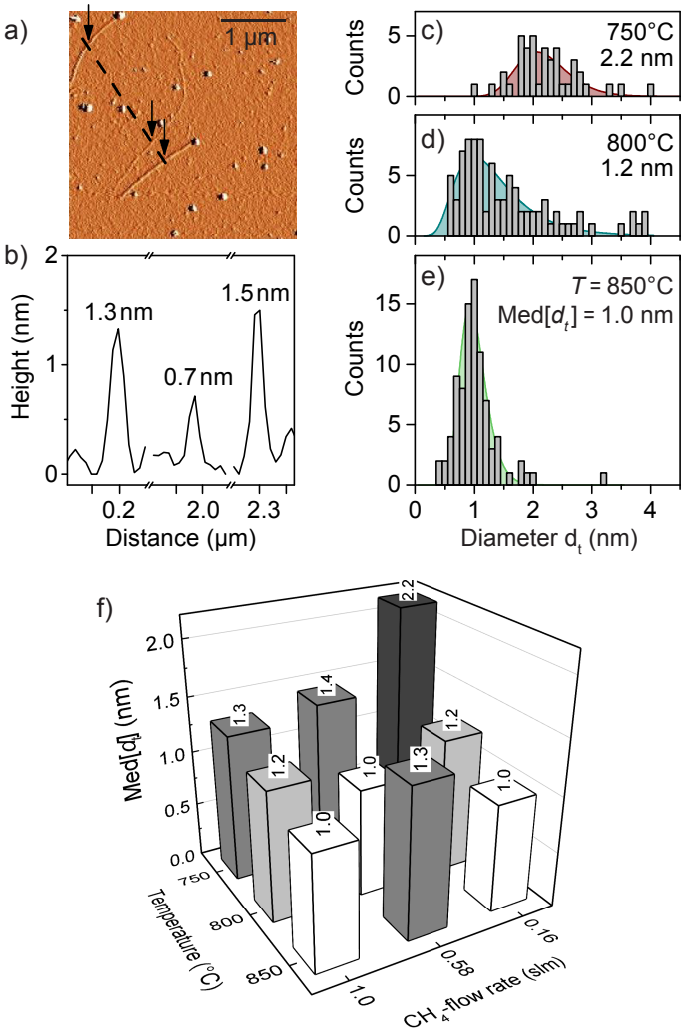

Figure 4.5: a) Example of a $(3.5\times 3.5)\,\mu m^2$ atomic force microscopy image used for the analysis of carbon nanotube diameters. The image shows three individual carbon nanotubes. b) The height profile from the line scan of the nanotubes marked by the arrows in (a) yields diameters of 1.3 nm, 0.7 nm, and 1.5 nm, respectively. c,d,e) Diameter distributions of carbon nanotubes obtained for reaction temperatures T of 750 °C, 800 °C, and 850 °C. Diameters were extracted from AFM height profiles. With increasing temperature the diameter distribution narrows and shifts to smaller values. The log-normal fits to the histograms determine the median Med$[d_t]$ of each distribution given in the graphs. The samples were grown with a methane flow rate of 0.16 slm and a methane/hydrogen flow rate ratio of 1.33. f) Bar chart of the diameter median for different growth temperatures T and methane flow rates (methane/hydrogen flow rate ratio: 1.33). The white bars represent growth conditions that yield a significant fraction of carbon nanotubes with diameters below 1 nm and corresponding emission wavelengths below 1050 nm.

in terms of the diameter distribution in successive CVD runs.

Based on recent investigations [105], it should be noted that the catalyst pretreatment by oxygen plasma as discussed in Section 4.3.2 increases the CNT diameters for a given set of CVD parameters [106].

4.4 Analysis by Raman spectroscopy

Having identified the synthesis parameters that favor narrow-diameter CNTs, the CVD method was applied to a perforated silicon nitride membrane[13] to allow the growth of SWNTs fully suspended over holes for background-free spectroscopy. Because CNT growth has shown to be less effective on silicon nitride substrates than on SiO_2, a 100 nm thick layer of silicon oxide was deposited on the membrane by plasma enhanced chemical vapor deposition[14] before applying the catalyst by drop casting and subsequent blow-drying with nitrogen. CNT growth was performed as described in Section 4.2.3 at 850 °C at a methane flow rate of 1.0 slm (methane/hydrogen flow rate ratio: 1.33).

Raman spectra were obtained at cryogenic temperatures (77 K and 4.2 K) and laser wavelengths of 780–830 nm (i. e. ~1.5–1.6 eV) with the use of the confocal microscope described in Section 3.1. Figure 4.6a shows a local raster-scan map depicting the intensity at the G-band energy detuning from the excitation laser (~197 meV) as a function of lateral sample displacement with respect to the microscope objective. A hole of the perforated membrane is clearly visible as a drop in intensity (colored in black). The pronounced G-band intensity peak stems from a CNT spanned across the hole as evidenced by the complementary SEM image (semitransparent top layer of Figure 4.6a) of the same sample region. As already mentioned in Section 2.1.2, Raman scattering is a highly resonant process. Therefore, only a certain fraction of all SWNTs from the CVD process is expected to be detectable due to the limitation of accessible laser wavelengths. From the Kataura plot in Figure 2.9b, the resonance Raman condition is most likely to be met for the E_{22} transition of SWNTs with diameters of 1.0–1.3 nm. Indeed, the SEM image in Figure 4.6a shows a second CNT bridging the hole for which the Raman resonance condition is not met but that exhibits PL emission at 1.273 meV (see Figure 5.9 in Chapter 5) indicating a diameter below 0.8 nm [32].

Even though the used microscopic setup did not allow for detecting the diameter-dependent RBM, the diameters of the located CNTs were estimated from the experimental frequency spacing of the Raman G^+- and G^--bands: According to Jorio *et al.*, the Raman frequency of the G^--mode scales as $\omega_G^- = \omega_G^+ - \frac{47.7\,\mathrm{cm}^{-1}}{(d_t\,[\mathrm{nm}])^2}$ for semiconducting CNTs [22]. From the Raman experiment, values of $\Delta\omega_G = \omega_G^+ - \omega_G^-$ were found to be in the range 20–40 cm^{-1} for most investigated CNTs and diameters were calculated to be 1.1–1.5 nm. These values are in good agreement with the estimated diameters from the Kataura plot if one also considers the scattered resonance condition for the Raman process where the incident photon carries the energy of the optical transition plus the phonon energy (e. g. ~197 meV for the G-band) thereby effectively extending the detection range.

Figure 4.6b,c shows the result of the analysis of as-grown CNTs by Raman spectroscopy. The dark gray line in Figure 4.6b depicts the Raman spectrum of a suspended CNT excited at a laser wavelength of 802 nm and a laser intensity of 0.18 $\mathrm{mW}/\mu\mathrm{m}^2$. The resonances from tangential stretching vibrations of carbon atoms, G^+ and G^-, were found at 1595 cm^{-1} and 1560 cm^{-1}, respectively. The defect-related D-band resonance at ~1300 cm^{-1} was identified by enhancing the intensity by a factor of 50 (light gray

[13] *TEMwindows.com* SN100-A50MP2Q05: hole diameter: 2 µm, pitch: 4 µm
[14] *Oxford Instruments* Plasmalab 80 Plus (PECVD)

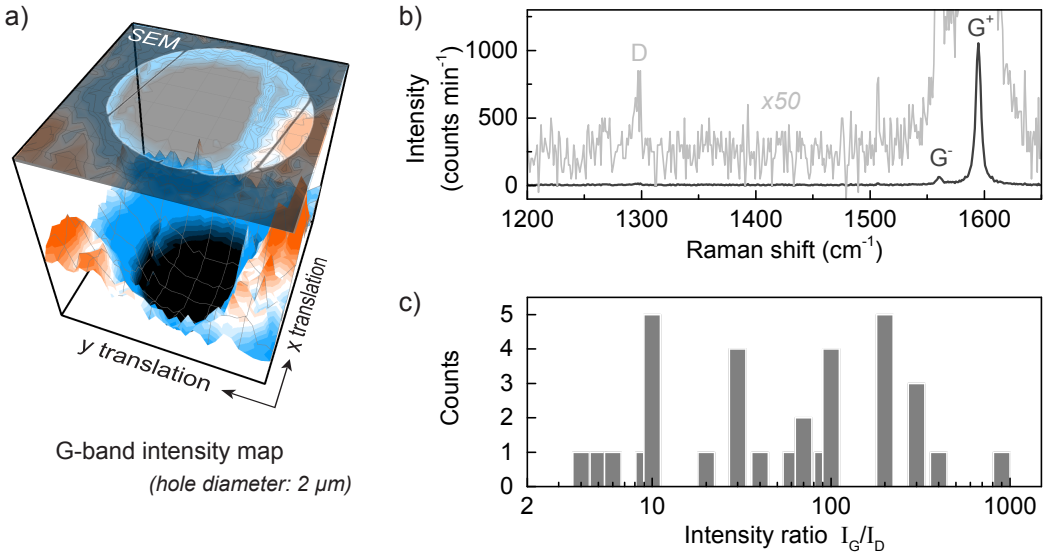

Figure 4.6: a) Color-coded spectral intensity around 1590 cm^{-1} frequency detuning from the laser source (corresponding to the Raman shift of the G-band) as a function of lateral displacement. The raster-scan intensity map is complemented by a scanning electron micrograph (SEM, top layer) of the same sample region depicting a hole of 2 µm diameter with two suspended carbon nanotubes. b) Representative Raman spectrum of a suspended carbon nanotube with a pronounced G-mode around 1590 cm^{-1} (dark gray line). At 50-fold magnification of the spectrum (light gray line) the defect-related D-band is visible at ~1300 cm^{-1}. c) Histogram of the intensity ratios of the G- and D-band resonances, I_G/I_D, obtained from measurements of 33 carbon nanotubes. About the half of the investigated nanotubes exhibits a I_G/I_D-ratio ≥50, which is indicating a high structural quality of the synthesized carbon nanotubes.

spectrum in Figure 4.6b). As the intensity ratio I_G/I_D of the G- and D-band is expected to increase with the number of structural impurities, the two bands are particularly instructive when considering the CNT material quality [24–27]. A histogram of the intensity ratios I_G/I_D from CVD-grown CNTs is shown in Figure 4.6c. The values for I_G and I_D were extracted from Lorentzian fits to the corresponding Raman peaks. The experimentally found intensity ratios span two orders of magnitude with values up to several hundred suggesting a wide range in structural quality: from average purity comparable to commercial materials[15] to high-purity CNTs with I_G/I_D ≥100.

4.5 Conclusion

In this chapter, carbon nanotube growth by the catalytic chemical vapor deposition method was presented. The experimentally realized setup was based on methane as the carbon precursor and on a bimetallic iron-ruthenium catalyst. The impact of various synthesis parameters on the sample properties was investigated: Firstly, within the explored range of reaction temperatures (700–850 °C), the carbon nanotube areal density

[15] e.g. $I_G/I_D \approx 40$ from this analysis corresponds to the quality parameter Q=0.98 of *SWeNT* SG65i CoMoCAT CNTs [107]. A similar estimate was made for HiPco CNTs from *NanoIntegris* [108].

turned out to be independent of the gas flow rate but was found to increase with rising temperature and to saturate around 800 °C. Secondly, by exposing the catalyst particles to an oxygen plasma prior to the chemical vapor deposition process, the samples' CNT length distribution was shifted from values around ~1 µm to lengths ranging from a few micrometers up to hundred microns. Thirdly, by using atomic force microscopy as an analysis tool of the diameters of carbon nanotubes from various growth procedures, it was demonstrated that a significant fraction of nanotubes with subnanometer diameters can be obtained with optimized catalytic chemical vapor deposition parameters.

To test the material quality by background-free Raman spectroscopy, as-grown carbon nanotubes suspended on perforated membranes were synthesized by the optimized chemical vapor deposition method. The intensity ratios of the G- and D-band of individual carbon nanotubes from these measurements revealed that about 50 % of the carbon nanotubes produced with the in-house chemical vapor deposition process were of high purity.

Chapter 5

Photoluminescence spectroscopy of individual as-grown carbon nanotubes

This chapter presents the results of cryogenic photoluminescence studies of single carbon nanotubes produced by catalytic chemical vapor deposition. Two sample structures were employed for investigation: a Si/SiO_2 substrate with carbon nanotubes in contact with the silica surface and a perforated membrane supporting carbon nanotubes fully suspended over holes. The optical response of single-walled carbon nanotubes from the two samples was substantially different in terms of variations in emission energy and intensity, and the coupling to phonon modes as revealed by the spectral line shape and photoluminescence excitation measurements.

5.1 Introduction

Figure 5.1 depicts exemplary emission spectra of individual SWNTs at the temperature of liquid helium (4.2 K) and the corresponding FWHM linewidths. The spread of peak positions demonstrates that several SWNTs with subnanometer diameters and PL emission energies above 1.18 eV (wavelengths below 1050 nm) were obtained with optimized catalytic CVD. The depicted spectra stem from different sample structures (to be discussed below) that are considered to have different impacts on the specific CNT surrounding and thereby on the emission characteristics. Indeed, the individual spectra showed a wide variety of spectral profiles: symmetric and asymmetric lines with an emission wing at the low-energy side were observed. Additionally, the full width at half maxima of the PL peaks scattered between values of a few millielectronvolts and linewidths of the order of 100 µeV. In the following, two distinct sample designs with CNTs on a silica substrate and CNTs suspended over holes, and the associated photophysical properties will be discussed.

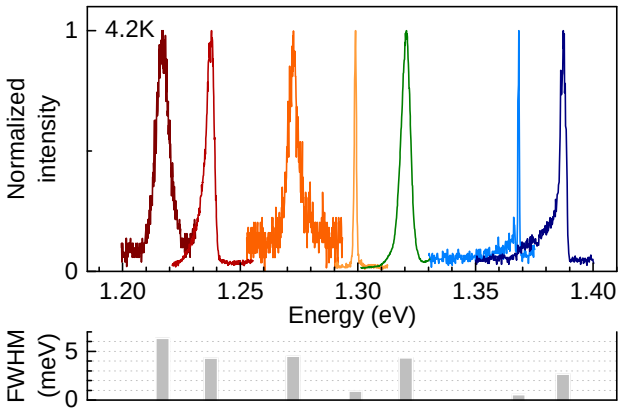

Figure 5.1: Top panel: The photoluminescence of individual as-grown single-walled carbon nanotubes at 4.2 K exhibits both a variety of emission energies reflecting the different chiralities as well as a large diversity of emission profiles with symmetric (e. g. the brown and green spectra) and asymmetric peaks with a low-energy wing (e. g. the red and dark blue spectra). Lower panel: The full width at half maximum (FWHM) spectral linewidths range from a few millielectronvolts to values of the order of 100 µeV.

5.2 Carbon nanotubes on a silica substrate

This section presents details on the sample fabrication by optical lithography prior to CVD of CNTs as well as the study of basic PL properties from these as-grown CNTs, such as the time evolution of PL spectra, the absorption characteristics by PLE spectroscopy, and the spectral line shape.

5.2.1 Sample fabrication

Silicon chips with a 100 nm thick SiO_2 surface layer were used as substrates for CNT growth. For orientation and complementary imaging (e. g. at different discrete temperatures or with AFM and SEM), the samples were patterned with a marker frame by optical lithography (Figure 5.2). To this end, the sample was cleaned with acetone and isopropyl alcohol in a bath sonicator and then coated with an image reversal photoresist[1]. After prebake on a hotplate, the sample was exposed by ultraviolet (UV) light using an inverted shadow mask positioned on top of the sample by a mask aligner[2]. The reversal bake on a hotplate crosslinked the exposed areas and the subsequent flood exposure (i. e. UV illumination with no mask used) made the still photoactive resist of the previously unexposed areas soluble in the developer[3]. Thereby, areas that had been exposed during the first UV illumination step remained and showed a negative wall profile ideally suited for lift-off. The pattern for orientation was applied by reactive ion etching of the substrate while regions still capped with photoresist remained unaltered. Finally, the remaining resist was removed in an acetone bath. A detailed list of the fabrication steps can be found in Appendix B.

A SEM image of the etched marker structure is shown in Figure 5.3a. The main pattern area consisted of 9×9 markers with a pitch of 10 µm constituting 64 squares of 100 µm^2 each. Unambiguous orientation was provided by a labeling at the edge of the pattern (not shown in Figure 5.3a) and a well-defined number assignment (1–64) to each of the square areas. After sample patterning had been finished, the CNT growth method by CVD as presented in Chapter 4 was applied with a methane flow of 1.0 slm at 850 °C. For a quick cross check of the CNT diameter distribution, a dummy sample was prepared simultaneously with the main sample and was investigated by AFM. The topography image of the (10×10) µm^2 area presented in Figure 5.3b shows the etched markers at the edges of the scan as well as catalyst particles and single CNTs lying on the sample surface. The obtained CNT diameters from AFM line scans of the dummy sample are presented in Figure 5.3c. The fraction of small-diameter CNTs (i. e. d_t<1 nm) made the main sample promising for optical investigation and also demonstrates the reproducibility of the CVD process (Section 4.3.3).

[1] *Clariant* AZ 5214E
[2] *Karl Suss* MJB3
[3] *Clariant* AZ 351B

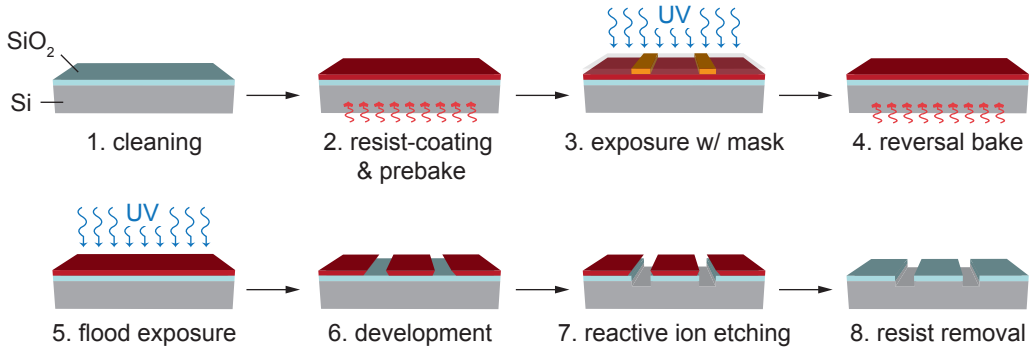

Figure 5.2: Sketch of the lithography process for samples patterned with a marker frame. The substrate was first cleaned (1) and spin-coated with an image reversal photoresist (2). The resist was baked on a hotplate (2) before exposing it to ultraviolet (UV) light at areas defined by the shadow mask (3). Image reversal was performed by reversal bake on a hotplate (4) and flood exposure (5). Development removed the previously unexposed areas and left an undercut for the remaining resist (6). Reactive ion etching (7) yielded the desired pattern. In a final step, the remaining resist was removed by acetone (8).

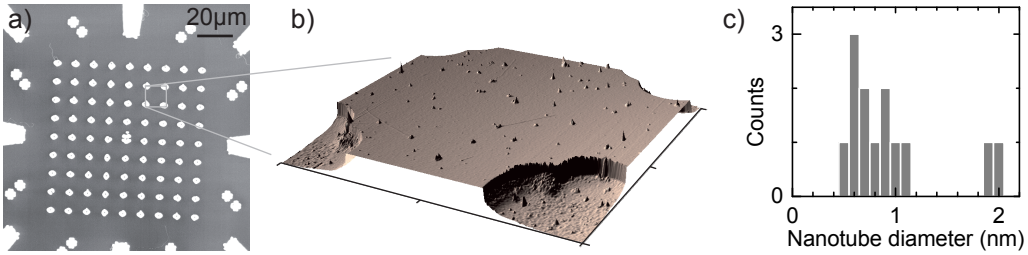

Figure 5.3: a) Scanning electron micrograph of the marker pattern applied to a Si/SiO_2-sample by reactive ion etching. Gray and white areas identify the bare substrate and the etched markers, respectively. b) Three-dimensional projection of an exemplary topography image by atomic force microscopy from a dummy sample showing the etched marker structure at the four edges and single carbon nanotubes lying on the substrate surface. c) Cross check results of the carbon nanotube diameter distribution by atomic force microscopy.

5.2.2 Photoluminescence of as-grown carbon nanotubes on silica

For a first optical investigation of as-grown CNTs on the patterned substrate, a temperature of 77 K was chosen[4]. While the sample was located inside the cryogenic microscope, the etched markers of the substrate provided means for orientation by the following methods: For coarse positioning with the piezo-steppers, the CCD camera of the microscope's collection arm was used to image the individual markers under slightly defocused laser illumination. For fine positioning with the sample surface in focus, scattered laser light from the substrate's markers identified the distinct square regions. Thereby, 2D PL maps that yield the position of single emitting SWNTs relative to the marker frame were obtained. To this end, a small area of typically about $(15\times15)\,\mu m^2$

[4] Previous investigations with commercial SWNTs yielded a higher PL visibility at cryogenic temperatures as compared to measurements at room temperature.

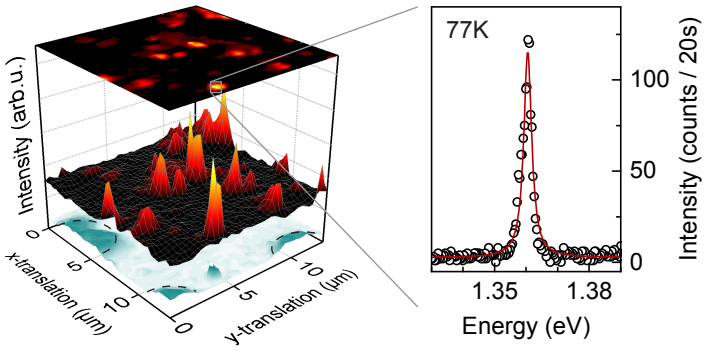

Figure 5.4: Left: Spatio-spectral photoluminescence intensity maps; 41×41 pixels, 20 s integration time. The white to cyan color-coded plot at the bottom depicts the etched marker frame at the corners, also indicated by the dashed lines. The photoluminescence intensity map from the SiO_2 surface region (middle surface plot and projection at the top) reveals several emission hotspots. Right: Spectral dispersion of such a hotspot reveals the photoluminescence emission peak of a single-walled carbon nanotube. The red line is a Lorentzian fit to the data points (open circles) with a full width at half maximum of 3.0 meV.

was raster-scanned with the piezo-scanners and a spectrum was acquired at each step. An exemplary false-color 2D PL map obtained with this procedure is depicted in the left panel of Figure 5.4. The presented plot consists of three layers: The white to cyan coded bottom layer represents the maximum intensity of the 860–870 nm spectral band as a function of lateral displacement. This plot allows identification of the etched markers by a change in substrate-related background in the respective wavelength range, clearly visible at the corners of the squared area and indicated by the dashed lines. The middle and top layers represent the maximum PL intensity of each spectrum as a function of lateral displacement as color-coded surface plot and its 2D projection, respectively. Several intensity hotspots were found in the scanned area. Spectral dispersion yielded PL peaks from as-grown SWNTs as depicted in the right panel of Figure 5.4. The red line to the data points is a Lorentzian fit with a FWHM of 3.0 meV.

Depolarization effect and spectral evolution with time

Typical features of SWNT emission spectra are presented in Figure 5.5 for the same SWNT at 77 K. As already mentioned in Section 2.2.1, optical transitions in SWNTs are subjected to a large depolarization effect. Accordingly, the PL intensity is a function of the linear excitation polarization with a $\cos^2 \alpha$ dependency [49], where α is the angle between the light's polarization vector and the CNT axis. Figure 5.5a exemplifies this so-called antenna effect: The polar plot (upper graph) depicts the integrated emission peak intensities (black squares) as a function of the linear excitation polarization adjusted with the microscope's half-wave plate. The red curve is a $\cos^2 \alpha$ fit function. The lower graph of Figure 5.5a shows PL spectra for linear polarizations parallel (co) and perpendicular (cross) to the SWNT axis highlighting the pronounced difference in intensity with an extinction ratio (maximum to minimum intensity) of 50.

Time traces of the spectrally dispersed PL revealed fluctuations in both the emission

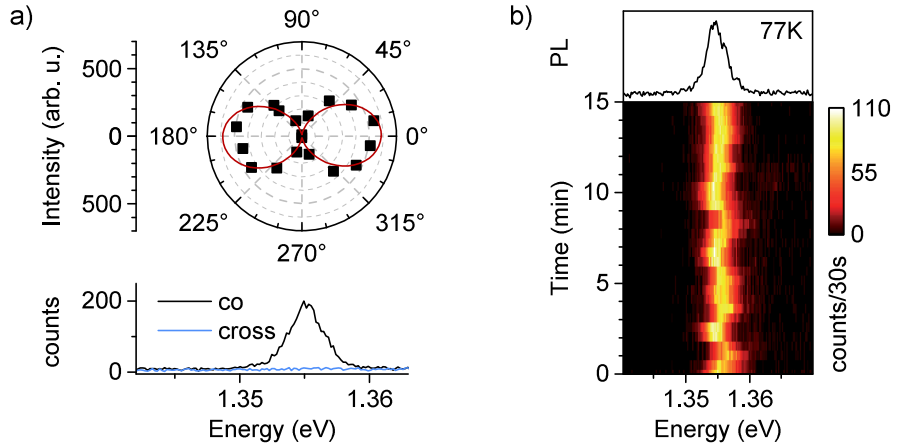

Figure 5.5: a) Depolarization effect: The photoluminescence intensity is a function of the (linear) excitation light polarization α with respect to the carbon nanotube axis. The red curve in the polar plot (upper panel) is a fit with $\cos^2 \alpha$ dependence. Emission spectra at co-polarized and cross-polarized excitation (lower panel). b) Photoluminescence spectrum (upper panel) and corresponding time evolution over 15 minutes (lower panel) of the same single-walled carbon nanotube at circularly polarized excitation. The emission exhibits pronounced spectral wandering and intensity fluctuations. All data were acquired at 77 K with continuous wave excitation at 815 nm and 70 µW. The integration time was 30 s.

intensity and energy (Figure 5.5b). Similar effects are also observed in different materials like quantum dots [109, 110] or quantum rods [111, 112]. Strong variations in intensity, also known as blinking, and spectral wandering are commonly attributed to the quantum-confined Stark effect induced by local electric field variations via trapped and released surface charges in the vicinity of the CNT [19, 20]. Also the gaseous environment has been debated as a source of intensity fluctuations by oxygen molecule adsorption and photoinduced chemisorption [113, 114]. In most studies, however, the CNT environment consists of micelles from the unbundling process [43, 115] and the substrate surface. The CNTs investigated here had been synthesized directly on the substrate with low density, so that unbundling steps were not required leaving CNTs free from any micelle-coating. Further, the microscope was operated in an inert ambient of ~20 mbar helium gas. Therefore, the observed fluctuations were attributed to the SiO_2 substrate. Indeed, Ai *et al.* have shown that capping SWNTs on silica with PMMA[5] removes surface-bound water molecules from the SiO_2 substrate resulting in a much more stable PL [55].

Photoluminescence excitation spectroscopy

By PLE spectroscopy, characteristic phonon-assisted absorption processes [116, 117] were investigated. To this end, PL spectra were acquired as a function of the cw titanium-sapphire laser wavelength which was varied in discrete steps of ~ 0.5 nm at constant power. Figure 5.6a depicts the PLE spectrum of a single SWNT on silica at 77 K as a 2D color plot. Having fit each PLE spectrum with a Lorentzian yielded the integrated PL

[5] Poly(methyl methacrylate)

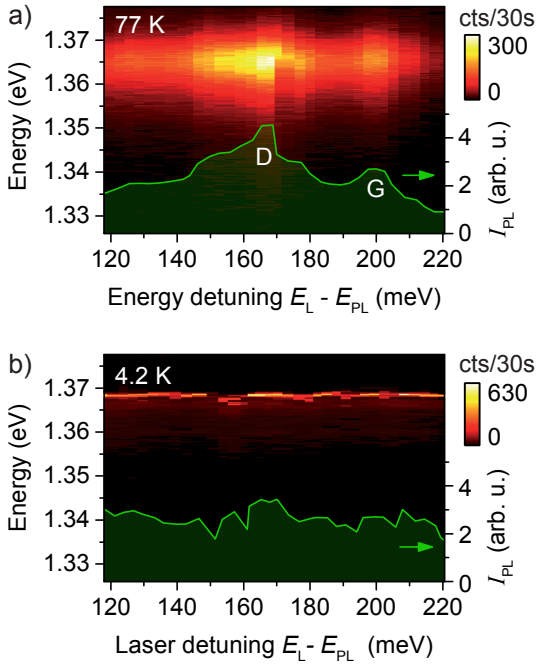

Figure 5.6: a) Photoluminescence excitation map of an as-grown carbon nanotube at 77 K. The photoluminescence intensity as a function of the laser detuning (green line) shows two resonances around 165 meV and 200 meV coinciding with the Raman D- and G-band, respectively. b) Photoluminescence excitation map of the same carbon nanotube at 4.2 K. The narrow emission line exhibits a blurred intensity profile (green curve) as compared to the 77 K case. All data were acquired at continuous wave excitation at 70 µW and with 30 s integration time per spectrum.

intensity I_{PL} as a function of the laser detuning from the PL resonance, which is also plotted in Figure 5.6a (green curve). The PLE map shows two major intensity peaks, located around 165 meV and 200 meV energy detuning. Strong enhancement of the PL intensity is expected when the laser meets the resonance condition of simultaneously exciting an exciton to the fundamental emission state E_{11} and one or more phonons [116–118]. If the resonance condition is not met by the laser energy, PL emission can be yet expected due to exciton relaxation to E_{PL} via emission of an optical phonon with non-zero momentum and multiple acoustic phonons. However, due to much less ineffective coupling of the involved phonons, the PL intensity is weaker than for the resonant case [116]. Indeed, the two PLE resonances coincide with the expected energies of the D- and G-phonons (see Section 2.1.2) and can be regarded as a "fingerprint" of CNT emission. However, a strong PL resonance due to the defect-induced D-band is unusual [117] but can be explained as follows: For the presented data in Figure 5.6, acquired with the aspheric lens as the focusing element, the focal plane variation with different laser wavelengths resulted in a changing excitation intensity with a distinct maximum when the focal plane coincided with the sample surface. This effect added to the PL intensity dependence on the laser detuning and constituted a contributing factor to the D-band resonance in the PLE scan of Figure 5.6a.

The marker frame on the sample allowed re-locating the same SWNT at a temperature

of 4.2 K. Interestingly, the PLE map of the same CNT in Figure 5.6b indicated a weaker coupling of excitons to optical phonons as the distinct D and G-band resonances observed at 77 K (Figure 5.6a) were strongly blurred at 4.2 K leading to an almost flat PLE intensity profile (green curve in Figure 5.6b). A reduced exciton-phonon coupling for the same CNT was also observed for the case of acoustic phonon modes as revealed by analysis of the PL line shapes that is described in the following.

Spectral line shape

Figure 5.7a and b depict the PL spectra of the single SWNT on silica at 77 K and 4.2 K, respectively. The emission peak with a FWHM linewidth of 10.6 meV at 77 K evolved into a remarkably narrow emission line (FWHM: ~320 µeV) with a low-energy emission wing. As will be shown in the following, this peculiar line shape was well fitted using the recently introduced model of Vialla *et al.* [119] Their model relies on the description of asymmetric CNT PL spectra at low temperatures [120] that were explained by the coupling of a localized exciton [17] to a 1D acoustic phonon bath [120,121]. By including modifications of the exciton-phonon coupling due to small energy acoustic barriers, Vialla *et al.* were able to explain a wide diversity of low-temperature CNT PL line shapes. Technically, these modifications are taken care of by an altered form factor $F(\omega)$ that contributes to the exciton-phonon coupling matrix element.

Specifically, the PL line shape is calculated from the linear susceptibility

$$\chi(t) = -i\, e^{-i\overline{\Omega}t}\chi_T(t)\chi_0(t) \tag{5.1}$$

in response to a δ-shaped laser pulse. Here, $\overline{\Omega} = \Omega - \sum_q |\gamma_s(q)|^2 \omega_s(q)$ is the polaron-shifted transition frequency, $\hbar\Omega$ denotes the bare energy of the quantum dot state, and $\omega_s(q)$ describes the dispersion relation of the stretching mode which is given by $\omega_s(q) = v_s q$ for small wave vectors and the sound velocity v_s. The term $\gamma_s(q)$ is given by $\gamma_s(q) = g_s(q)/\omega_s(q)$, where $g_s(q)$ is the exciton-coupling matrix element which itself is given by the product of the form factor $F(q)$ and the deformation potential coupling $G(q) = q/\sqrt{2\rho L\hbar\omega_s(q)}$, with the CNT's linear mass density ρ, and length L. The temperature-dependent and temperature-independent contribution to the linear susceptibility in Equation 5.1 are

$$\chi_T(t) \propto i \exp\left(\sum_q |\gamma_s(q)|^2 \left[-n_s(q)\left|e^{-i\omega_s(q)t} - 1\right|^2\right]\right), \tag{5.2}$$

$$\chi_0(t) \propto i \exp\left(\sum_q |\gamma_s(q)|^2 \left[e^{-i\omega_s(q)t} - 1\right]\right), \tag{5.3}$$

where $n_s(q) = \left(e^{\hbar\omega_s(q)/k_B T} - 1\right)^{-1}$ denotes the phonon occupation number. The imaginary part of the Fourier transform of $\chi(t)$ yields the absorption spectrum which in turn is the mirror image of the experimentally obtained PL line shape. Now the form factor for the exciton in a parabolic potential can be expressed as

$$F_0(\omega_s) = D_s \exp\left(-\frac{\sigma_c^2\omega_s^2}{4v_s^2}\right), \tag{5.4}$$

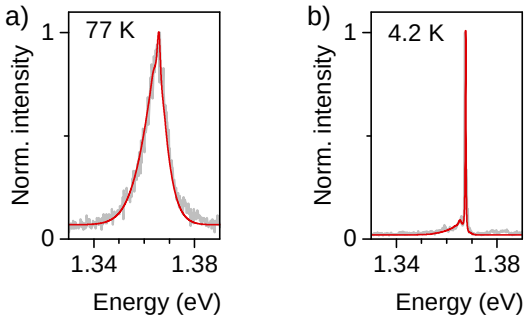

Figure 5.7: Photoluminescence spectra of the as-grown carbon nanotube from Figure 5.6 at a) 77 K and b) 4.2 K. The red curves are approximations to the data (light gray lines) according to the acoustic barrier model by Vialla *et al.* [119] All data were acquired at continuous wave excitation of 70 µW and 30 s integration time. The excitation energy was 1.501 eV.

where D_s is the deformation potential and σ_c is the quantum-dot-like confinement length of the exciton. The specific fits in Figure 5.7a and b were conducted under the assumption of a local acoustic barrier of length ℓ and height $\hbar\omega_c$ that modified the low energy phonon modes probed by the exciton. This barrier is implemented by the following approximate expression for the form factor [119]:

$$F_\ell(\omega_s) \approx F_0(\tilde{\omega}) \left(1 + \frac{\omega_c^2 \sin^2(\ell\tilde{\omega}/2v_s)}{\tilde{\omega}^2}\right)^{-1/2}, \tag{5.5}$$

where $\tilde{\omega} = \sqrt{\omega_s^2 - \omega_c^2}$.

The simulated spectra are depicted as red curves in Figure 5.7a and b (data is shown in light gray) and were achieved with parameters $D_s = 9$ eV, $\sigma_c = 2$ nm, and an acoustic barrier height $\hbar\omega_c = 1.2$ meV and width $\ell = 38$ nm. Effective temperatures of 77 K and 12 K were used for the fits in Figure 5.7a and b, respectively. The overall good agreement of the low-temperature spectra with the utilized model suggests ineffective coupling of excitons to long-wave acoustic phonon modes in as-grown CNTs pinned to a silica surface. This interpretation is strengthened by theory of thermal conductivity [122] which proposes the appearance of a low-energy acoustic gap due to local hardening of the nanotube lattice by CNT-substrate interactions.

As a last point, it should be noted that under the assumption of electron-hole symmetry, theoretical modeling of the exciton-phonon coupling through deformation potentials reveals a much weaker contribution (factor 20) by the off-diagonal coupling matrix elements [123] than assumed in the model used here [119, 120]. However, depending on the distinct nature of exciton trapping potentials it is questionable if localized excitons preserve electron-hole symmetry. Regarding this question, it is of primary interest if and how the weights of the individual exciton-phonon coupling matrix elements are redistributed for trapped excitons with broken symmetry and has to be elucidated in further theoretical and experimental work.

5.3 Suspended carbon nanotubes

The previous section presented basic photophysical properties of individual cryogenic SWNTs grown on a silica substrate by the CVD method introduced in Chapter 4. This section presents the results of analogous investigations conducted for SWNTs suspended over holes and is complemented by magneto-PL spectroscopy.

5.3.1 Perforated substrates for suspended carbon nanotubes

To obtain suspended CNTs, the CVD method was employed on perforated silicon nitride membranes[6] with holes of 2 µm in diameter. The hole pattern of the sample, as depicted in the micrographs of Figure 5.8, provided a coordinate frame for unambiguous orientation. To maintain the surface growth conditions of CNTs on silica, the silicon nitride substrates were covered with a 100 nm thick layer of silicon oxide by plasma enhanced CVD[7] prior to drop casting the catalyst solution onto the sample surface and subsequent blow-drying with nitrogen. CNT growth was then performed at 850 °C with a methane flow rate of 1.0 slm as detailed in Chapter 4. The SEM image in Figure 5.8c shows the perforated sample after the CVD process with several CNTs fully suspended over the holes.

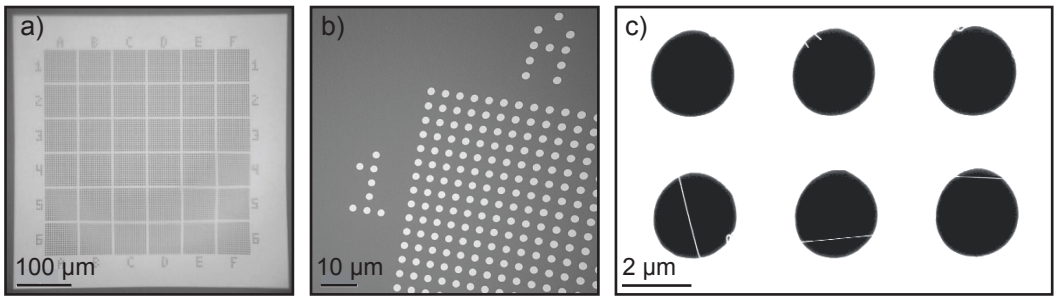

Figure 5.8: a,b) Optical micrographs of the perforated silicon nitride membrane that was used as a substrate for growth of suspended carbon nanotubes. Adapted from Ref. 124. c) Scanning electron micrograph of the sample after chemical vapor deposition of carbon nanotubes showing as-grown nanotubes fully suspended over holes.

5.3.2 Photoluminescence of suspended carbon nanotubes

As already discussed for the case of as-grown CNTs on a silica substrate (Section 5.2.2), spatiospectral maps of individual sample regions were acquired by raster-scanning the sample with respect to the focal spot of the excitation laser and recording a PL spectrum at each displacement position. By choosing appropriate spectral integration windows, intensity maps of the PL and of a substrate-related background signal at the blue end of each spectrum were obtained. Correlating the two maps allowed identification of individual suspended CNTs. Figure 5.9a exemplifies the approach: the PL intensity

[6] *TEMwindows.com* SN100-A50MP2Q05
[7] *Oxford Instruments* Plasmalab 80 Plus (PECVD)

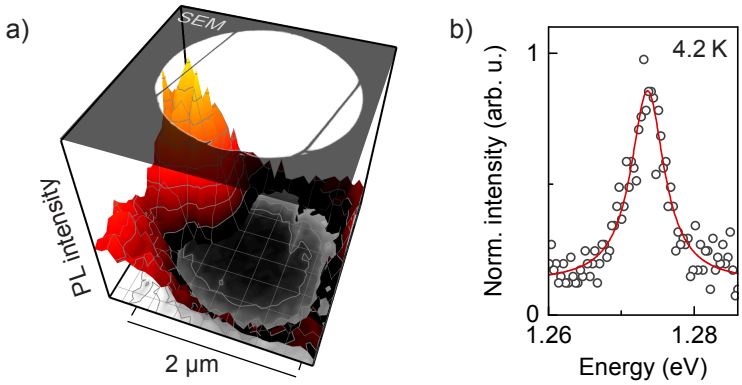

Figure 5.9: a) Raster-scan background signal (black-to-white color code) and photoluminescence intensity map (red-to-yellow color code) of a hole of the perforated substrate, complemented by a scanning electron micrograph (SEM, top layer) of the same sample region showing two suspended carbon nanotubes. b) Spectrum of the photoluminescent carbon nanotube in (a) at 4.2 K with a linewidth of 6 meV. The red curve is a Lorentzian fit to the data.

map in red-to-yellow color code shows a strong peak near the rim of a hole that was identified by the substrate-related background signal map depicted in black-to-white color code (projection at the bottom in Figure 5.9a). The maps are complemented by a semitransparent SEM image of the same sample region (top layer in Figure 5.9a) that was acquired after optical investigation and provides further evidence that the PL signal is related to an individual suspended CNT. The scanning electron micrograph revealed a second suspended CNTs that was not photoluminescent in the detection window of the optical setup (cf. Chapter 3). However, this CNT was identified by its Raman G-band. The corresponding raster-scan intensity map of the Raman signal is shown in Figure 4.6a. The spectrum of the photoluminescent CNT at 4.2 K is shown Figure 5.9b. The PL emission featured a single symmetric PL emission resonance with a FWHM linewidth of 6 meV that was obtained from a Lorentzian fit to the data (red curve in Figure 5.9b) and is in accord with earlier studies of symmetric single-peak spectra with linewidths in the range of a few millielectronvolts [125, 126].

Depolarization effect and spectral evolution with time

As already discussed above for the case of a SWNT on silica, the integrated PL intensity shows a pronounced antenna effect, meaning that the PL emission intensity fits a $\cos^2 \alpha$ dependence, where α is the angle between the laser light's linear polarization vector and the CNT axis. Figure 5.10a highlights this polarization anisotropy for a suspended SWNT: the polar plot (upper panel in Figure 5.10a) shows the integrated PL intensity data (black squares) that is well approximated by the fit function with $\cos^2 \alpha$ dependence (red curve) while the two PL spectra (lower panel in Figure 5.10a) illustrate the strong suppression of the PL emission in case of perpendicularly polarized (cross-polarized) excitation.

The spectral evolution of the PL over time of the same suspended SWNT is depicted in Figure 5.10b. The single symmetric emission peak with a FWHM linewidth of 2.2 meV displayed drastically reduced spectral diffusion and intensity variations as compared to

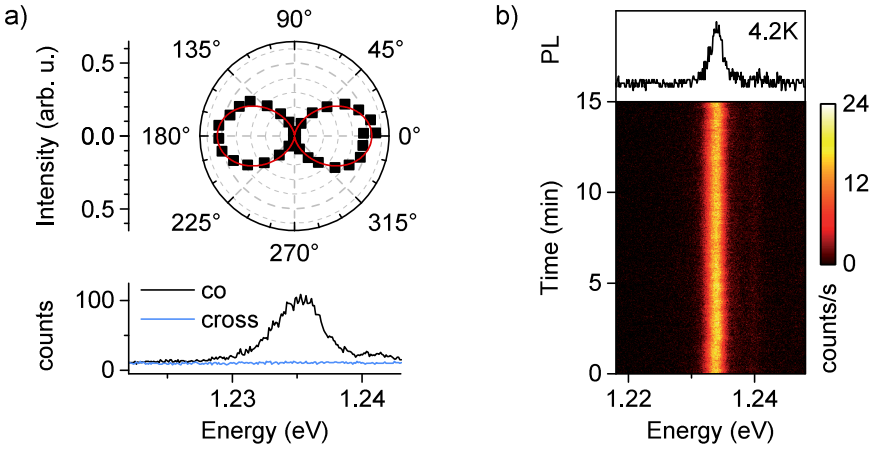

Figure 5.10: a) Upper panel: Polar plot of the polarization dependence of a suspended carbon nanotube's integrated photoluminescence intensity. The red curve is a fit with $\cos^2 \alpha$ dependence, where α is the angle between the laser's linear polarization vector and the carbon nanotube axis. Lower panel: Photoluminescence spectra obtained under co-polarized and cross-polarized excitation at 77 K. b) Photoluminescence emission peak (upper panel) and corresponding spectral evolution over 15 minutes (lower panel) of the same single-walled carbon nanotube at 4.2 K. The emission is free from significant spectral wandering and intensity fluctuations.

the CNT in contact with silica (Figure 5.5b). The steady PL characteristics of the SWNT suspended in the inert gas ambient is a hallmark of minimized interactions with the substrate.

Photoluminescence excitation spectroscopy

PLE spectroscopy was employed to probe the absorption characteristics near the fundamental transition E_{11} of the suspended SWNT. Figure 5.11 depicts the corresponding PLE map, where the PL intensity in 2 s integration time is plotted on a logarithmic false-color scale with the emission energy along the y-axis and the laser detuning from the PL peak energy at 1.234 eV along the x-axis. Weak diagonal lines that cross the PL peak and lead to strong resonances in the PL emission were observed in the accessible detuning range of 98–470 meV. These lines maintain a constant separation from the laser energy—a feature inherent to Raman peaks and implying that the resonances are due to phonon-assisted absorption processes. Further evidence is provided by the integrated PL peak intensity as a function of the laser detuning that was obtained from Lorentzian fits to the emission spectra and is displayed as the green curve in Figure 5.11: the intensity peak positions coincide with the energies of prominent CNT phonons and phonon combination modes. In particular, the most pronounced features are the G-band around 200 meV and the replica of the G'-mode at ~320 meV. In the detuning range between these two modes (i. e. from 200 meV to 320 meV), the curve shows two more resonances, at 222 meV and 231 meV, that can be assigned to the M-band and the combination of the G-band and the RBM, respectively. From the position of the latter resonance, the RBM energy was estimated by subtracting the G-

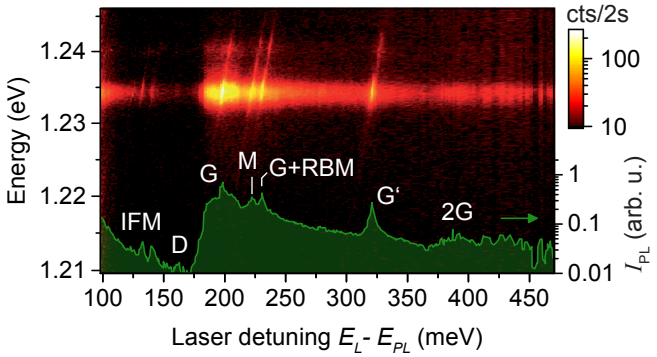

Figure 5.11: Photoluminescence excitation map of an as-grown suspended carbon nanotube at 4.2 K in false-color representation. The green curve is the integrated photoluminescence intensity I_{PL} as a function of the laser detuning from the photoluminescence peak energy at 1.234 eV. The resonances stem from simultaneous excitation of specific phonon modes with the emitting exciton state E_{PL}.

phonon energy (197 meV), yielding ~34 meV, which is equivalent to a RBM frequency of $\omega_{\mathrm{RBM}} = 274\,\mathrm{cm}^{-1}$ and corresponds to a SWNT diameter of 0.8 nm,[8] as expected for SWNTs emitting in the spectral detection window of the optical setup. Further weak resonances were detected at energy detunings around 140 meV, 150 meV, and 390 meV where the intermediate frequency modes (IFM), the D-band, and the overtone of the G-mode (2G) can be found, respectively [28]. In essence, the observed resonances in the PLE map indicate strong coupling of excitons to optical phonon modes, constituting a "fingerprint" of excitonic nanotube PL.

Magnetic brightening of the dark exciton

It was shown in Section 2.2.2 that a singlet exciton with zero angular momentum and even parity is located below the bright exciton state. This low-energy exciton is optically inactive, but can be brightened by a magnetic flux ϕ threading the CNT along its axis [30, 127–129]. The magnetic flux adds an Aharonov-Bohm phase to the circumferential component of the electron wave function, thereby lifting the degeneracy of the K and K' valleys [36]. With increasing flux that is threading the CNT, the optically active exciton state X^{β} and the lowest lying singlet exciton state X^{δ} mix, and spectral weight is redistributed. The Aharonov-Bohm mixing of the two states is given by [128]

$$\Delta_{\mathrm{AB}} = \mu_{\mathrm{AB}}\phi + \Delta_{\mathrm{dis}} = \mu_{\mathrm{AB}}\pi B_{\parallel} d_t^2/4 + \Delta_{\mathrm{dis}}\,, \tag{5.6}$$

where μ_{AB} is a coupling constant, $B_{\parallel} = B\cos\vartheta$ is the magnetic field component parallel to the CNT axis, and the disorder-induced zero-field splitting Δ_{dis} may be neglected if a zero-field brightening of the dark state is not observed. Using the simple two-level model of Refs. 130 and 37, the field-induced splitting of the bright and dark exciton states is given by [128]:

$$\Delta^2 = \Delta_{\mathrm{x}}^2 + \Delta_{\mathrm{AB}}^2\,, \tag{5.7}$$

where Δ_{x} is the zero-field splitting.

[8] The SWNT diameter was determined with the relation $\omega_{\mathrm{RBM}}[\mathrm{cm}^{-1}] = 227/d_t[\mathrm{nm}]$ from Ref. 23.

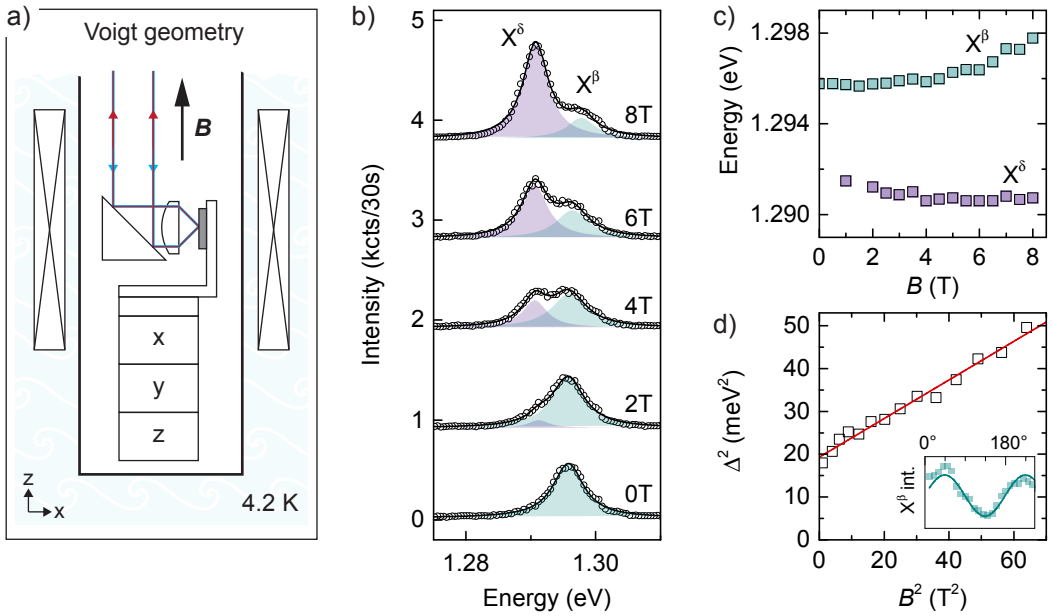

Figure 5.12: a) Schematics of the optical configuration and sample orientation in Voigt geometry for carbon nanotube PL spectroscopy in a magnetic field B. b) Magnetic field dependent photoluminescence spectra of an as-grown suspended single-walled carbon nanotube at 4.2 K. With increasing magnetic field the dark exciton peak (X^{δ}) increases in intensity at the expense of the bright exciton emission peak (X^{β}). The black curve is a cumulative fit composed of two Lorentzian functions (colored in purple and cyan) to the data (open circles). c) Emission peak energies of the bright (X^{β}) and dark (X^{δ}) exciton as a function of applied magnetic field. d) Linear fit (red line) to the squared energy splitting Δ as a function of squared magnetic field B to obtain the zero-field splitting Δ_x. Inset: data (cyan squares) and fit (cyan curve) of the bright exciton emission intensity as a function of the angle between the linear excitation polarization vector and the magnetic field direction.

Figure 5.12a shows a schematic diagram of the experimental setup to test the magnetic field dependence of as-grown SWNTs. A magnetic field B of up to 9 T and fixed field direction was provided by a superconducting magnet inside a helium bath cryostat. The sample was oriented in Voigt geometry by an L-profile sample holder that was mounted on the stack of piezo-positioners. The excitation laser light was redirected by a right-angle prism mirror[9] and focused with an aspheric lens[10] onto the sample. As the CNTs on the sample surface were randomly oriented, only nanotubes with a significant magnetic field component parallel to the tube axis showed a brightening of the dark excition state. Figure 5.12b depicts the evolution of the PL emission of an as-grown suspended SWNT with increasing magnetic field. At $B = 0$ T the nanotube exhibited a single symmetric PL peak centered at 1.296 eV with a FWHM linewidth of 5.8 meV. With increasing B-field, the dark exciton X^{δ} progressively brightened at the expense of the bright exciton PL as evident from the appearance of the low energy peak in Figure 5.12b. A cumulative fit function composed of two individual Lorentzians was used to model the PL spectra in Figure 5.12b and to extract the emission peak positions of the bright

[9] *Thorlabs* MRA10-P01
[10] *Thorlabs* 352330-B, focal length: 3.1 mm, numerical aperture: 0.68

and brightened dark exciton as a function of the magnetic field. The B-field dependence of the PL energies is plotted in Figure 5.12c.

In order to deduce the zero-field splitting Δ_x from Equations 5.6 and 5.7, the energy splittings Δ of both emission peaks in Figure 5.12c were extracted. Furthermore, the polarization dependence of the PL intensity (inset of Figure 5.12d) yielded the orientation of the SWNT with respect to the magnetic field ($B_\parallel = B\cos 45°$) and the SWNT diameter $d_t = 0.78$ nm was determined from the PL emission energy [32]. A zero-field splitting of 4.4 meV was obtained from the linear fit in Figure 5.12d, in accord with previously found values for CNTs of comparable diameters [128, 129].

The findings identify magneto-PL as a viable complementary probe of the CNT spectrum. The technique is particularly interesting for the understanding of CNTs with narrow emission lines that are to be discussed in Chapter 7.

5.4 Conclusion

This chapter presented basic photophysical properties of individual cryogenic single-walled carbon nanotubes that were grown by the catalytic chemical vapor deposition method described in Chapter 4. In a first step, the photoluminescence of carbon nanotubes in contact with the silica surface of a Si/SiO_2 substrate was investigated. Unambiguous orientation and the re-locating of individual carbon nanotubes at different experimental conditions were provided by a marker frame on the silica surface defined by optical lithography. The photoluminescence of substrate-supported as-grown carbon nanotubes revealed spectral wandering on the scale of millielectronvolts and intensity fluctuations on seconds timescales. Additionally, the distinct resonances in the photoluminescence excitation spectra at 77 K that were assigned to phonon-assisted absorption processes largely disappeared upon cool-down to 4.2 K. At the same time, spectral line shape peculiarities with a substantially narrowed photoluminescence peak and a red-shifted emission wing evolved. The emission spectra were in good agreement with theoretically modeled line shapes that assumed a modified coupling of localized excitons to long-wave acoustic phonons due to interactions with the substrate. In a second step, the photoluminescence of isolated carbon nanotubes that were grown to be fully suspended over the holes of a perforated membrane was studied. In contrast to nanotubes on silica, the emission of suspended carbon nanotubes exhibited symmetric peaks with linewidths of a few millielectronvolts that were stable both in energy and intensity. Also, the resonances in photoluminescence excitation spectra at 4.2 K were perfectly accounted for by phonon-assisted excitation. Additional cryogenic magneto-photoluminescence experiments confirmed the existence of a dark exciton state few millielectronvolts below the bright exciton transition.

In summary, the overall good agreement of the low-temperature emission spectra of the substrate-supported carbon nanotube with the applied model, as well as the strongly reduced fluctuations in the emission of suspended nanotubes highlight the role of the environment for the photophysical properties of individual single-walled carbon nanotubes. The consequences of environmental interactions for the optical properties are further elaborated in the following chapter.

Chapter 6

Exciton localization in cryogenic carbon nanotubes

This chapter presents photoluminescence studies of individual HiPco, CoMoCAT, and as-grown semiconducting single-walled carbon nanotubes at room and cryogenic temperatures. From the analysis of spatial and spectral features of the nanotube photoluminescence, characteristic signatures of unintentional exciton localization are identified. Moreover, the energy scale of exciton localization potentials was quantified as ranging from a few to a few tens of millielectronvolts and stemming from both environmental disorder and shallow covalent side-wall defects. The results establish disorder-induced crossover from the diffusive to the localized regime of nanotube excitons at cryogenic temperatures as a ubiquitous phenomenon in both micelle-encapsulated and as-grown carbon nanotubes.

THIS CHAPTER IS BASED ON THE PUBLICATION
Matthias S. Hofmann, Jonathan Noé, Alexander Kneer, Jared J. Crochet, and Alexander Högele. Ubiquity of exciton localization in cryogenic carbon nanotubes, *Nano Letters* **16**, 2958–2962 (2016).

6.1 Introduction

At cryogenic temperatures individual carbon nanotubes exhibit single-photon emission statistics [17]. Figure 6.1 presents exemplary PL spectra and second-order coherence measurements of three single CNTs of the HiPco[1], CoMoCAT[2], and as-grown type at the temperature of liquid helium (4.2 K). The spectral profiles exhibited multi-peak emission (Fig. 6.1a) as well as single symmetric (Fig. 6.1c) and asymmetric (Fig. 6.1e) emission lines. The second-order photon correlation measurements were performed using the HBT setup described in Section 3.3.2. The repetition rate of the titanium-sapphire laser (76 MHz) lead to coincidence peaks equally spaced by the laser pulse separation $\tau_{\mathrm{rep}} = (76\,\mathrm{MHz})^{-1} = 13.2\,\mathrm{ns}$ in the unnormalized correlation function $G^{(2)}(\tau)$ in Figure 6.1b,d,f. The results of the HBT experiments show suppressed coincidence peaks at zero time delay ($\tau = 0$), indicating that multiphoton emission after single-laser pulse excitation is inhibited. With normalized coincidence peak areas at non-zero time delays, the degree of photon antibunching was determined from the integrated suppressed central peak at $\tau = 0$ in each case. The normalized second-order correlation function at zero time delay, $g^{(2)}(0)$, varied from 0.66 for the HiPco CNT, to 0.26, and 0.11 for the CoMoCAT and as-grown CNT, respectively. Values of $g^{(2)}(0)$ of less than unity are a signature of a quantum light emitter and a hallmark of exciton localization [17–19, 119, 120, 126, 133, 134]. This quantum-dot-like, quasi zero-dimensional regime of CNTs is of both fundamental and practical interest, as it provides improved coherence [126, 134] and higher quantum yield [134–136] of localized excitons for novel applications in quantum cryptography [17, 18, 126, 134, 137] or spin-based quantum information processing [138].

Exciton localization can arise accidentally in various CNT materials [17–19, 119, 126, 133, 134], or it can be promoted by means of covalent side-wall functionalization with oxygen [135, 137, 139, 140] or diazonium [136] chemistry. While chemical doping yields defect-specific exciton localization traps as deep as 100–300 meV [135–137, 139, 140], the order of magnitude of unintentional localization potentials stemming from structural or environmental disorder along the CNT axis remained elusive. In the following, the results of PL spectroscopy experiments on individual SWNTs identifying the localization energy scale and the related spectral signatures of disorder-induced exciton traps are presented. The comprehensive studies are based on monitoring the PL of individual micelle-encapsulated HiPco and CoMoCAT nanotubes, as well as SWNTs obtained with the in-house CVD method on silica substrates at room temperature (295 K) and the temperatures of liquid nitrogen (77 K) and liquid helium (4.2 K).

[1] The HiPco process is a large-scale CVD process using high-pressure CO and iron as a catalyst [131].
[2] The CoMoCAT process is catalytic CVD method using CO and a unique Co-Mo catalyst [132].

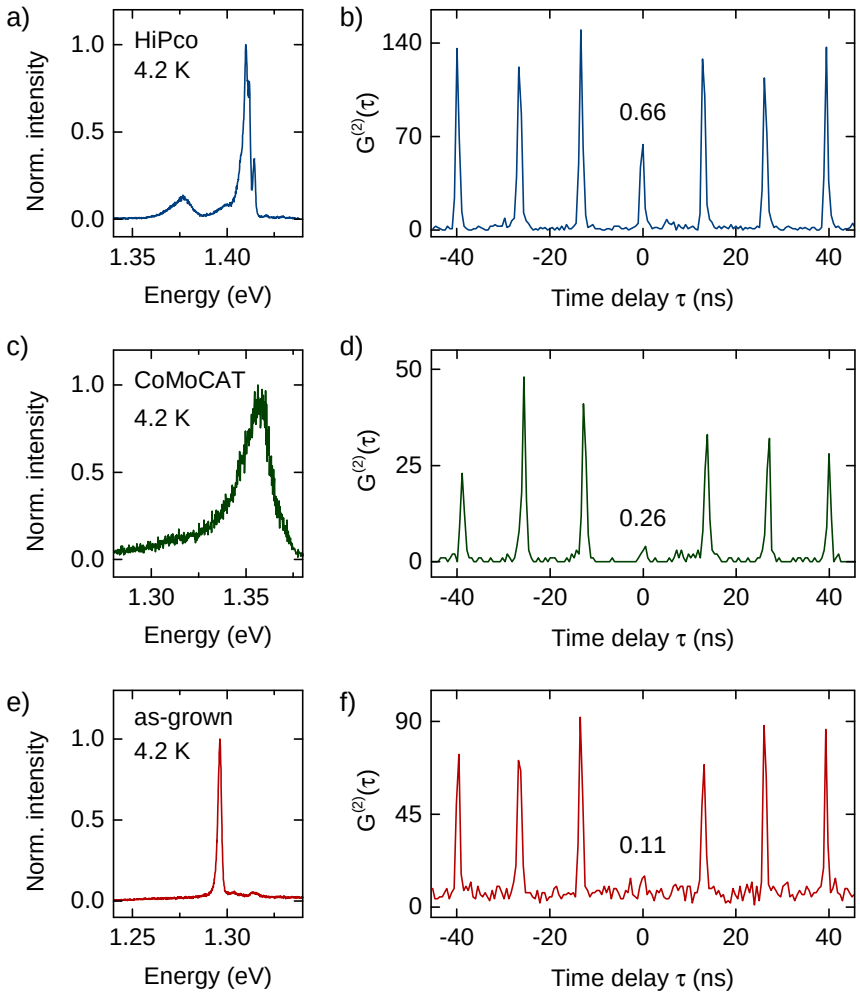

Figure 6.1: Photoluminescence spectra of an individual a) HiPco, c) CoMoCAT, and e) as-grown single-walled carbon nanotube at 4.2 K, and b,d,f) the corresponding unnormalized second-order correlation function $G^{(2)}(\tau)$. The suppressed correlation peaks at zero time delay $\tau = 0$ are a signature of emission from a single-photon source. The emission probabilities of more than one photon derived from normalized coincidence peaks are 0.66, 0.26, and 0.11 for the HiPco, CoMoCAT, and as-grown carbon nanotube, respectively.

6.2 Carbon nanotube samples

Si/SiO_2 substrates were used to support HiPco and CoMoCAT CNTs wrapped in deoxycholate and sodium cholate, respectively. Prior to the deposition of HiPco and CoMoCAT CNTs out of aqueous suspensions, the substrates were patterned with markers for lateral orientation on the sample by direct optical imaging via the confocal microscope's CCD or by monitoring the intensity of the silicon Raman band at 521 cm^{-1}. The markers were fabricated by optical lithography and successive metal deposition or reactive ion etching. Metallic markers were obtained by depositing a 2 nm thick titanium adhesion layer followed by 20 nm of gold in an ultra high vacuum electron-gun evaporator deposition system after development of the optically lithographed sample. Subsequent lift-off in an acetone bath yielded the metallic markers on the silica surface. The details

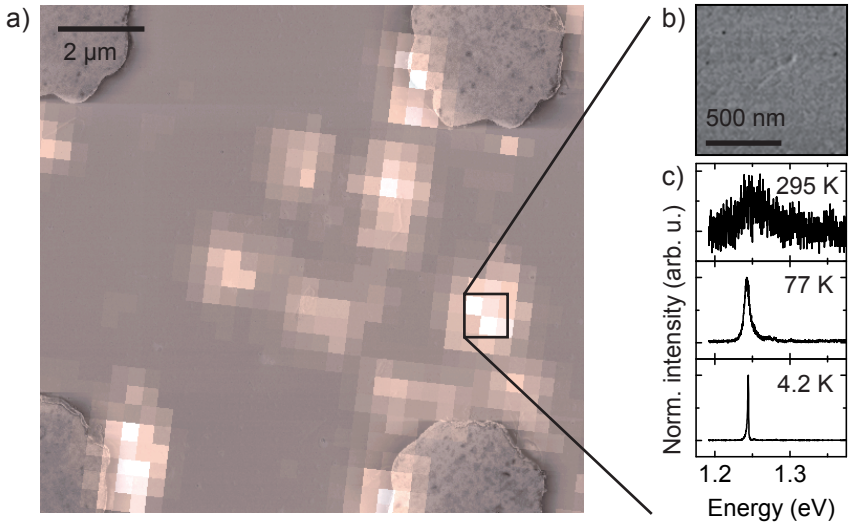

Figure 6.2: a) Scanning electron micrograph of a CoMoCAT sample superimposed by a semitransparent photoluminescence map showing several emission hotspots. Metallic markers on the substrate surface are identified at the corners of the micrograph. b) Close-up scanning electron micrograph depicting a single CoMoCAT carbon nanotube lying on the silica surface. c) Normalized photoluminescence spectra of the carbon nanotube in (b) obtained with confocal photoluminescence microscopy at three fixed temperatures (295 K, 77 K, and 4.2 K).

of optical lithography and the etching process for marker fabrication are described in Section 5.2.1 and Appendix B.

Surfactant-wrapped HiPco and CoMoCAT CNTs were spin-coated on the substrates to yield densities of less than one nanotube per μm^2. For samples with as-grown CNTs, commercial TEM grids consisting of a silicon nitride membrane with a perforated coordinate system were used. Details of the sample were already given in Section 5.3.1. It should be noted, however, that as-grown SWNTs on silica were chosen for this study.

6.3 Hyperspectral mapping of exciton localization

The marker pattern on the substrates allowed for retracing of individual CNTs at the three fixed temperatures (295 K, 77 K, and 4.2 K) of the experiments as well as with SEM or AFM. Figure 6.2a depicts a scanning electron micrograph of the CoMoCAT sample superimposed by a semitransparent raster-scan PL map of the same sample region with several emission hotspots in false-color representation. Four metallic markers are identified at the corners of the SEM image. The close-up view in Figure 6.2b depicts a single CNT of around 400 nm in length in contact with the silica substrate. Raster-scanning the same sample region with confocal PL microscopy and taking spectra at each displacement position at the three distinct temperatures 295 K, 77 K, and 4.2 K allowed to extract the emission spectra from the sample spot associated with the CNT in Figure 6.2b. The evolution of the obtained PL spectra with decreasing temperature is presented in Figure 6.2c. The observed emission from single CoMoCAT SWNTs in the

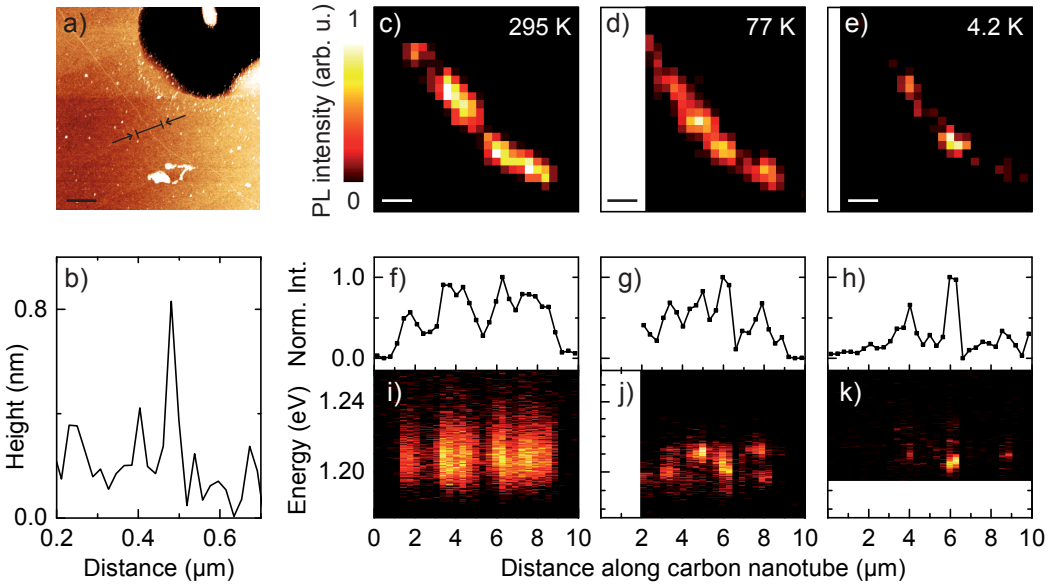

Figure 6.3: a) Atomic force micrograph of a single HiPco carbon nanotube with a length of ~10 µm. The black area in the upper right corner is an etched marker structure. b) The height profile along the line in the topography image in (a) is consistent with the diameter of an individual (7,5) nanotube. c,d,e) Local photoluminescence maps of the same sample area as in (a). f,g,h) Intensity profiles along the nanotube axis at temperatures of 295 K, 77 K, and 4.2 K. The nanotube exhibits extended room-temperature emission that fractionalizes progressively into emission hotspots at cryogenic temperatures. i,j,k) The spectral dispersion of the photoluminescence energy along the carbon nanotube axis at three fixed temperatures of the experiment reveals the emergence of multi-peak emission upon cool-down. The scale bars are 1 µm.

acquired hyperspectral maps was typically confined to single spots of 1 µm in diameter and PL variations along the tube axis were not resolved. From SEM analysis, the mode of the length distribution of CoMoCAT CNTs was found to be 540 nm, which is significantly smaller than the spatial resolution of the optical setup (~1 µm). Therefore, the characteristic spatial and spectral signatures of unintentional exciton localization are established using a representative HiPco SWNT that was several microns in length: The atomic force micrograph in Figure 6.3a shows the respective CNT with a length of ~10 µm and a diameter of ~0.8 nm determined from the height profile in Figure 6.3b. For the same nanotube, hyperspectral maps at three fixed temperatures were recorded by raster-scanning the sample with respect to the focal spot of the apochromatic low-temperature micro-objective and recording the PL spectrum within the interval of 1.20–1.30 eV at each pixel. The corresponding raster-scan PL intensity images shown in Figures 6.3c–e were obtained by integrating the spectra within limited exciton-specific bands at each pixel. The profiles of the PL intensity (Figure 6.3f–h) and the spectral PL characteristics (Figure 6.3i–k) were obtained from respective hyperspectral image analysis along the nanotube axis.

At room temperature, the (7,5) nanotube of Figure 6.3a exhibited a PL resonance consistently centered at 1.207 eV [32, 115] with ~30 meV FWHM linewidth and without

significant spectral variations along the nanotube axis (Figure 6.3i). The respective axial PL intensity profile was extended over several microns (Figure 6.3f) with characteristic quenching regions at the nanotube ends and at the sites of disorder sampled by diffusive excitons [57, 114, 141–150]. The fragmented axial PL profile at ambient conditions fractionalized progressively with reduced temperatures. The raster-scan images in Figure 6.3d and e, as well as the axial PL profiles in Figure 6.3g and h, demonstrate how the extended nanotube PL evolved into singular hotspots at 77 K and 4.2 K, respectively. This hotspot axial PL fragmentation, observed with confocal microscopy for cryogenic nanotubes, is one main signature of exciton localization at the sites of disorder that resembles previous observations at room temperature and sub-100 nm length scales with near-field microscopy [26, 142]. The second main signature is evidenced by the spectral axial PL profiles of Figure 6.3j and k: the spectral variations of 10–15 meV along the SWNT axis [26] become more and more pronounced on the scale of the spectral linewidth of ~3 meV and ~1 meV at the temperatures of liquid nitrogen and liquid helium, respectively. Finally, the emergence of multiple emission resonances (as in Figure 6.3j at the axial position of 8 µm) is identified as the third main characteristic of exciton localization in accord with previous studies [54, 125].

6.4 Analysis of multi-peak emission spectra

In the second step of the analysis the multi-peak PL structure of individual nanotubes was used to quantify the energy scale associated with unintentional exciton trap potentials. To this end, the experimental observations at three fixed points of temperature were confronted with theoretical expectations. The data in Figure 6.4a exemplifies the approach. The spectra of a single (6,5) HiPco nanotube at 295 K, 77 K, and 4.2 K were used to extract the PL peak positions from Lorentzian fits (red curves in the top panel of Figure 6.4a) as a function of temperature, and to compare these values for the emission energies (triangles in the bottom panel of Figure 6.4a) with the theoretical prediction for the thermal band gap renormalization [151] (black solid curve in the bottom panel of Figure 6.4a).

In the theoretical work by Capaz *et al.* [151], the effects of electron-phonon coupling contributing to the temperature-dependent bang gap shift are approximated by a two-phonon model [152] as

$$\Delta E_g(T) = E_g(T) - E_g(0) = \frac{\alpha_1 \Theta_1}{e^{\Theta_1/T} - 1} + \frac{\alpha_2 \Theta_2}{e^{\Theta_2/T} - 1}\,, \tag{6.1}$$

where $\Theta_{1,2}$ are the effective temperatures of the two model phonons and $\alpha_j \Theta_j$ are the corresponding effective electron-phonon coupling coefficients. The anharmonic contribution to the temperature dependence of E_g that arises from the thermal expansion is small and can be neglected [151]. The parameters of Equation 6.1 as well as the the band gap shifts $\Delta E_g(295K)$ for various narrow-diameter SWNTs are tabulated in Appendix C. The values for the three chiralities (6,5), (8,3), and (9,1) that were used in the analysis below are summarized in Table 6.1.

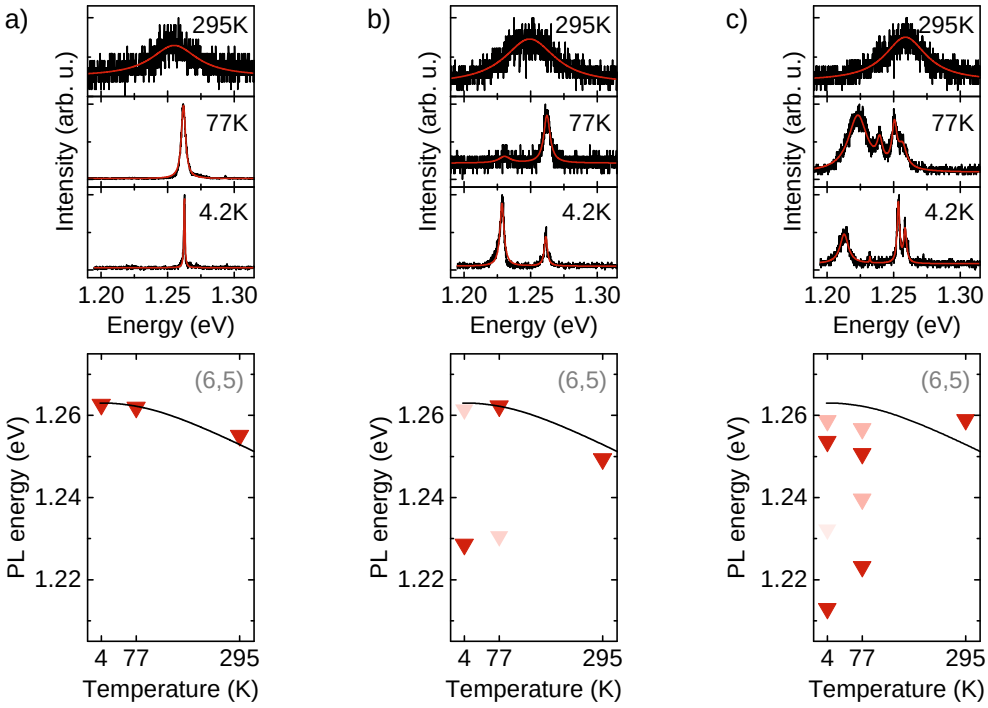

Figure 6.4: a) Photoluminescence spectra of an individual (6,5) HiPco carbon nanotube at 295 K, 77 K, and 4.2 K (top panel) and peak emission energies (lower panel) extracted from Lorentzian fits (red solid lines). The energy dispersion with temperature (black solid line) shows the theoretical dependence of the band gap according to Capaz *et al.* [151] b,c) Same data for two other (6,5) HiPco carbon nanotubes of the sample which deviate from the ideal picture by developing red-shifted satellites of multi-peak spectra. Data points with different shades of red indicate relative intensities of the emission peaks.

(n,m)	α_1 (10^{-5} eV/K)	Θ_1 (10^2 K)	α_2 (10^{-5} eV/K)	Θ_2 (10^2 K)	ΔE_g(295 K) (meV)
(6,5)	-1.94	1.04	-4.30	4.53	-10.11
(8,3)	-0.24	0.97	-6.54	5.45	-7.27
(9,1)	0.42	1.04	-7.62	5.77	-6.22

Table 6.1: Coefficients for modeling the temperature dependent band gap renormalization of the (6,5), (8,3), and (9,1) nanotube chiralities according to Equation 6.1 proposed by Capaz *et al.* [151]

As for the nanotube in Figure 6.4a, the chiralities of the individual SWNTs of these experiments were assigned using their room temperature PL emission energy [32, 115] and allowing energy offsets of the order of 10–30 meV to account for the tube-to-tube variations in the effective dielectric environment [50–52] which may stem from an inhomogeneous tube coverage by surfactant [148], water-filling of CNTs dispersed from aqueous suspensions [153], or local charges in the nearby substrate [54–56].

Figures 6.4b and c show data of two other (6,5) HiPco nanotubes of the same sample. Both CNTs clearly contrast the nearly-ideal picture of the CNT in Figure 6.4a: instead of the expected line narrowing and blue-shift upon cool-down, they develop multi-peak

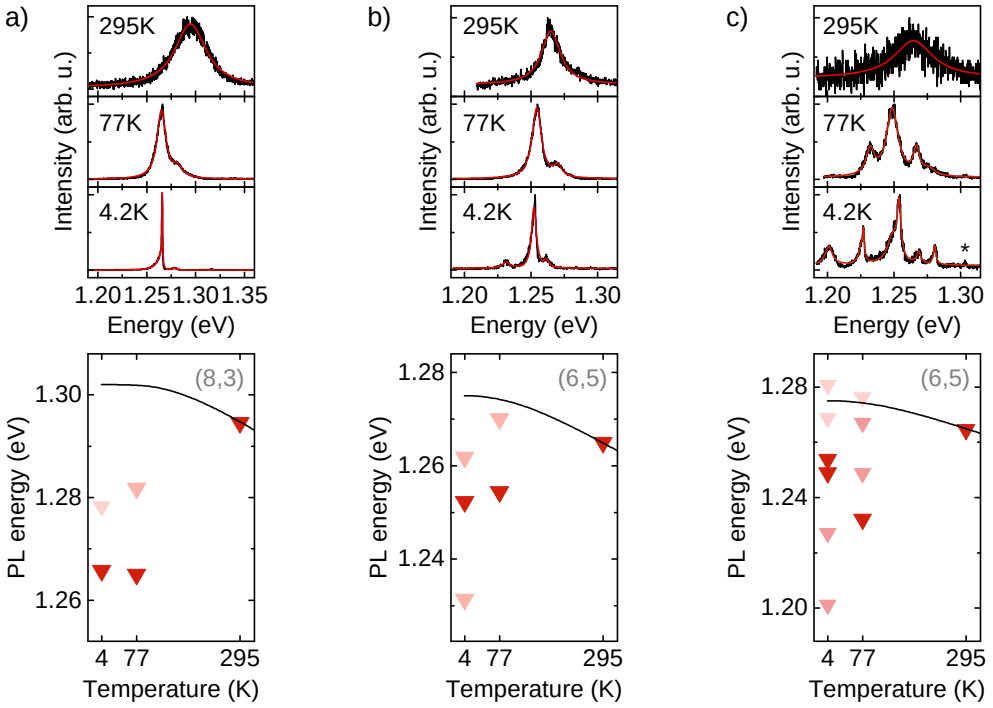

Figure 6.5: a,b,c) Photoluminescence spectra (top panels) and peak emission energies (lower panels) of three individual CoMoCAT carbon nanotubes at 295 K, 77 K, and 4.2K. The energy dispersion with temperature (black solid curve in the bottom panels) shows the theoretical dependence of the band gap according to Ref. 151. Peaks marked by the asterisks correspond to carbon nanotube Raman bands.

PL resonances (two and four peaks in the spectra of Figure 6.4b and c, respectively) of variable linewidths (note the broad red-most peak in Figure 6.4c) and spectral red-shifts of the order of a few tens of millielectronvolts. In the case of the two-peak emission, the fundamental PL peak follows the theoretically expected energy dispersion but loses its intensity at the expense of the red-shifted satellite that emerges as a weak signature at 77 K and dominates at 4.2 K (Figure 6.4b). This observation is consistent with thermal localization of excitons in the lowest-lying state, which appears 33 meV below the E_{11} emission for the CNT of Figure 6.4b. The example of a CNT with a four-peak emission as in Figure 6.4c is also instructive. The energy splittings between the satellites and the main E_{11} peak, that roughly follows the theoretical thermal shift, were estimated as 5 meV, 26 meV, and 46 meV from Lorentzian fits to the spectra at 4.2 K in Figure 6.4c. This energy scale is in remarkable agreement with the low-temperature characteristics of shallow oxygen side-wall defects in ether-I configuration [140]. Although the agreement could be accidental and deeper-lying localization states established in previous spectroscopy of oxygen-doped CNTs [135, 137, 139, 140] were not observed in these experiments due to the limited spectral detection window, it is plausible to include the class of covalent side-wall defects as a likely source of unintentional exciton localization. The fact that none of the CNTs on the investigated samples have experienced a deliberate chemical treatment prior to spectroscopic studies yet in most cases exhibited multi-peak spectra indicates that the notion of one-dimensional diffusive excitons in cryogenic CNTs is of only limited validity.

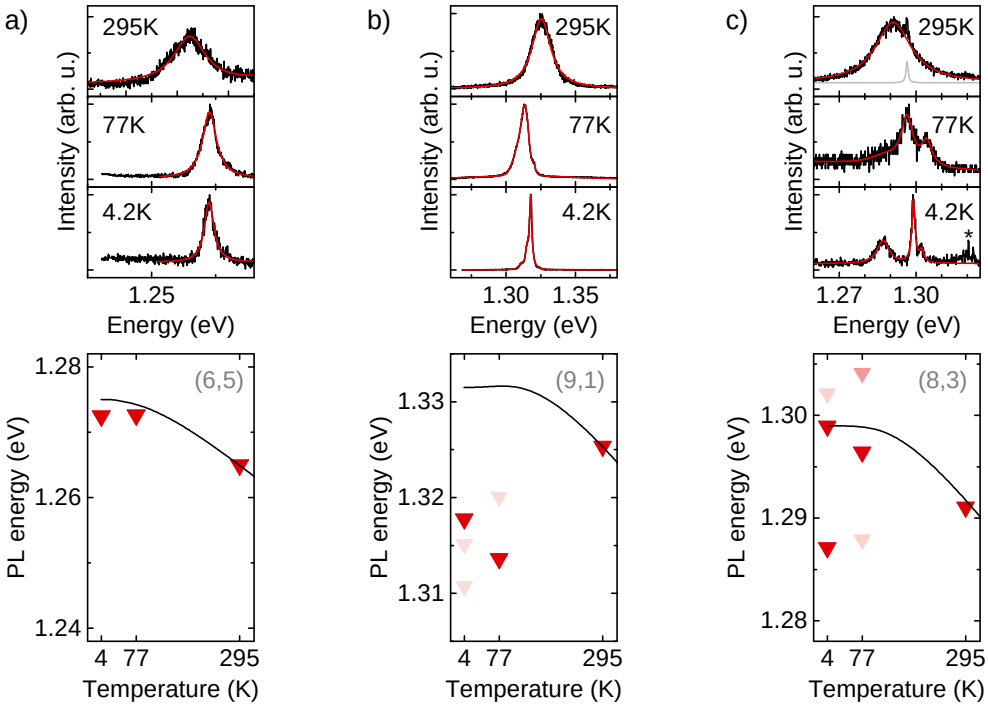

Figure 6.6: a,b,c) Photoluminescence spectra (top panels) and peak emission energies (lower panels) of three individual as-grown carbon nanotubes at 295 K, 77 K, and 4.2K. The energy dispersion with temperature (black solid curve in the bottom panels) shows the theoretical dependence of the band gap according to Ref. 151. Peaks marked by the asterisks correspond to carbon nanotube Raman bands.

Complementary to the data in Figure 6.4, additional PL spectra as well as PL peak positions and their theoretical temperature dependence are presented for individual CoMoCAT and as-grown CNTs at three fixed points of temperature (295 K, 77 K, and 4.2 K) in Figure 6.5 and Figure 6.6, respectively. Peaks marked by the asterisks correspond to CNT-related Raman bands and were not considered for analysis of the multi-peak PL structures.

In order to establish the generality of the spectroscopic findings, individual CNTs with single-peak spectra at room temperature and multi-peak spectra at cryogenic conditions were analyzed. The procedure described above allowed to quantify the exciton localization energy scale for CNTs of different chiralities obtained with different synthesis methods. Figures 6.7a–d show the histograms of PL emission peaks for HiPco tubes of (6,5) and (8,3) chirality, CoMoCAT (6,5) and as-grown (9,1) SWNTs, respectively. Only the fraction of CNTs with a single PL peak at room temperature was selected for statistical analysis. The increase in occurrences at cryogenic temperatures is a direct consequence of multi-peak emission profiles attributed to incidental localization. For each chirality and CNT synthesis method, the ensemble distribution of the PL energies at 295 K was fitted with a Gaussian function (shown as red solid lines in Figure 6.7) centered at the corresponding room-temperature energy of the chirality-specific E_{11} with a FWHM of 13 meV for the HiPco tubes and the (6,5) CoMoCAT tubes, and 19 meV for the as-grown (9,1) SWNTs. Same FWHMs of micelle-encapsulated HiPco and CoMoCAT

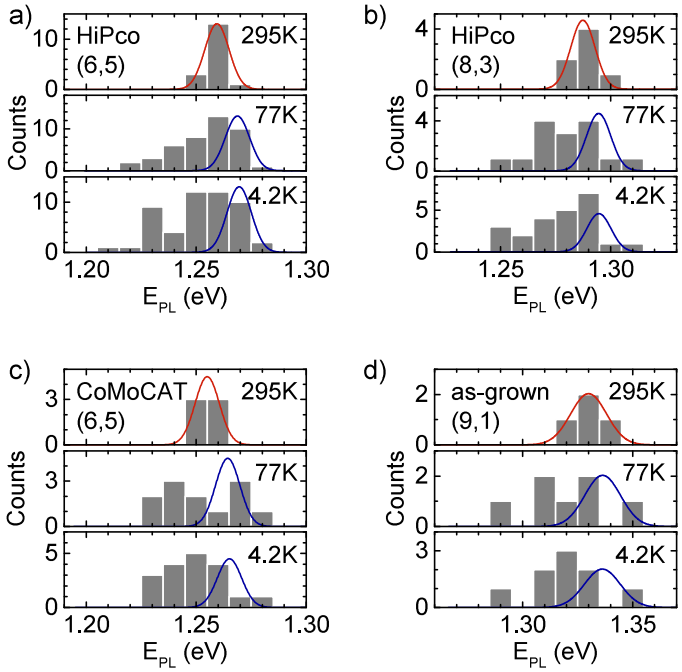

Figure 6.7: Photoluminescence energy histograms of a) HiPco (6,5), b) HiPco (8,3), c) CoMoCAT (6,5), and d) as-grown (9,1) carbon nanotubes at 295 K, 77 K, and 4.2 K. The Gaussian distributions of the single-peak emission at 295 K with ~10–20 meV full widths at half maxima (red solid lines) were used to calculate theoretically expected cryogenic distributions (blue solid lines) by taking into account the thermal band gap renormalization after Capaz *et al.* [151] Both the broadening and the asymmetry of the experimental distributions at cryogenic temperatures stem from exciton localization.

CNTs reflect similar average dielectric environments of nanotubes on samples prepared out of aqueous suspensions, while as-grown CNTs without surfactant are likely to experience higher spectral fluctuations and thus ensemble broadening due to their proximity to charge traps in SiO_2. In the low-temperature PL histograms of Figure 6.7 the Gaussian ensemble distributions (blue solid lines) were blue-shifted according to the theoretical temperature dependence of the band gap [151]. The asymmetric cryogenic ensemble distributions of Figure 6.7 underpin the picture of lower-lying exciton trap states, discussed above at the level of individual nanotubes. Furthermore, they provide evidence that unintentional exciton localization is a universal feature of CNT materials: for micelle-encapsulated HiPco and CoMoCAT CNTs as well as for surfactant-free as-grown nanotubes a redistribution of the PL emission from the fundamental E_{11} transition at room temperature to lower-lying localized exciton states at cryogenic temperatures was observed. The higher energy tail of the Gaussian ensemble distribution at 295 K is depleted upon cool-down, while the occurrence of the PL emission peaks at the lower energy side increases—a signature of exciton localization by environmental disorder with trap potentials as deep as 50–60 meV (lowest-energy states of (6,5) HiPco CNTs at 4.2 K in Figure 6.7a).

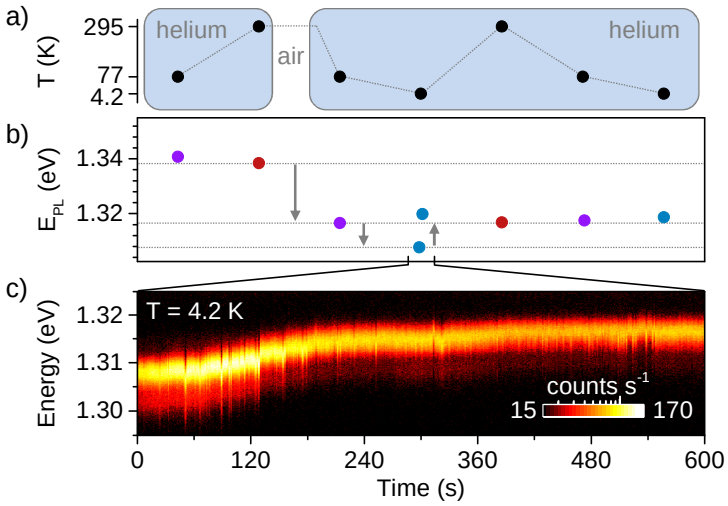

Figure 6.8: a) Measurement procedure: the emission of a single as-grown nanotube in an inert helium atmosphere was sampled at three fixed temperature points (the measurement progress was from left to right). After the first measurement point at 295 K the sample was exposed to air under ambient conditions. b) Corresponding peak photoluminescence energy E_{PL} determined at each point of fixed temperatures (red, purple and blue circles represent data points at 295 K, 77 K, and 4.2 K, respectively). c) False-color representation of the photoluminescence evolution at 4.2 K over 10 min. The emission energy exhibited a blue-shift of ~10 meV during the course of the measurement. The laser intensity was 17 kW/cm^2 at 807 nm wavelength.

6.5 Adsorbate-induced disorder

To shed light on the nature of the environmental disorder caused by adsorbates on the nanotube surface, a set of data for a single as-grown (9,1) CNT recorded over several cooling cycles is presented in Figure 6.8. All PL measurements were carried out on the same CNT in the inert atmosphere of a helium gas at 20 mbar. However, the sample has been exposed to ambient conditions for several days before the second cooling cycle, as indicated in the illustration of the measurement procedure shown in Figure 6.8a. After a measurement point at 77 K, the CNT was sampled twice from 295 K to 4.2 K with a measurement point at 77 K in between, and the maxima of the PL emission energy were determined at each fixed temperature point (colored data points in Figure 6.8b). The first red-shift of 2 meV in the PL energy from 77 K to 295 K is consistent with the thermal band gap renormalization of 6 meV expected for a (9,1) CNT [151]. Instead of blue-shifting back upon temperature reversal, however, the CNT PL developed a red-shift of 24 meV indicated by the first arrow in Figure 6.8b. This red-shift is interpreted as arising from a modified dielectric environment of the CNT due to adsorbates [23,52,58,154,155], most likely oxygen or nitrogen, that have contaminated the nanotube surface during its exposure to ambient conditions.

A further cool-down step from 77 K to 4.2 K in the inert helium atmosphere added an additional red-shift of 9 meV (second arrow in Figure 6.8b) instead of the theoretically expected value of 0.3 meV. It is plausible that additional adsorption of oxygen

or nitrogen, both present in their gaseous phase at 77 K and 20 mbar as a remanent contamination of the helium atmosphere, was responsible for this second red-shift. This scenario is supported by the observation of a laser-induced desorption process (third arrow in Figure 6.8b) which was monitored *in situ* with cryogenic PL spectroscopy. Figure 6.8c shows a sequence of 10 min as a part of this process: The temporal evolution of the nanotube PL showed a blue-shift of the emission energy by 12 meV due to desorption [154] induced by local laser heating. Within the initial ~5 min of laser excitation with an intensity of 17 kW/cm^2 at 807 nm wavelength the PL energy levelled-off at 1.32 eV after overcompensating for the red-shift caused previously by molecule adsorption at cryogenic conditions. Successive heating and cooling cycles showed thermally induced PL blue- and red-shifts within the range of a few meV (last four data points in Figure 6.8b) in accord with theoretical expectations. The observation of the PL energy shifts of the order of a few tens of millielectronvolts caused by adsorption and desorption processes on the very same CNT highlight the role that environmental disorder can play in exciton localization: an inhomogeneous coverage of the CNT surface by adsorbates would result in local exciton traps with potentials comparable to those of shallow covalent sidewall defects.

6.6 Conclusion

The presented results establish exciton localization as a general feature of micelle-encapsulated and as-grown carbon nanotubes at low temperatures. The analysis of spectral signatures, both at the level of individual nanotubes and single-walled carbon nanotube ensembles in different materials, highlights the roles of crystalline and environmental disorder for cryogenic exciton localization. The findings not only emphasize the sensitivity of the carbon nanotube excitons to their immediate surrounding, they also indicate the potential for spectral fine-tuning of the carbon nanotube emission into resonance with optical cavities for the realization of efficient single-photon cryptography devices in the telecom transmission window.

Chapter 7

Excitons in suspended carbon nanotube quantum dots

In this chapter, it is demonstrated that common limitations in carbon nanotube optics, such as rapid decoherence at non-radiative quenching sites [57], environmental dephasing [148], and emission intermittence [18], may be overcome by exciton localization in suspended carbon nanotubes. For excitons localized in nanotube quantum dots, narrow optical lines free of spectral wandering, radiative exciton lifetimes [63, 156, 157], and effectively suppressed blinking were observed. The findings identify the great potential of localized excitons for efficient and spectrally precise interfacing of photons, phonons, and spins in carbon nanotube-based quantum devices.

THIS CHAPTER IS BASED ON THE PUBLICATION
Matthias S. Hofmann, Jan T. Glückert, Jonathan Noé, Christian Bourjau, Raphael Dehmel, and Alexander Högele. Bright, long-lived and coherent excitons in carbon nanotube quantum dots, *Nature Nanotechnology* **8**, 502-505 (2013).

7.1 Introduction

By virtue of their exceptionally low mass and extreme stiffness, CNTs provide ultrahigh-quality mechanical resonances [158], promise long electron spin coherence times in a nuclear-spin free lattice [159, 160] for quantum information processing and spintronics, and feature unprecedented tunability of optical transitions [43, 115] for optoelectronic applications [8]. Excitons in semiconducting single-walled carbon nanotubes [6, 7] could facilitate the upconversion of spin [138], mechanical [123] or hybrid spin-mechanical [161] degrees of freedom to optical frequencies for efficient manipulation and detection. However, all-surface excitons in SWNTs are highly mobile at room temperature and thus exhibit high sensitivity to both the interior and exterior dielectric environments on length scales that far exceed the exciton Bohr radius [141, 162]. On the one hand, this is very attractive for CNT-based applications in optical sensing, but on the other hand, it renders CNT excitons susceptible to extrinsic perturbations. As a result, successful implementation of the aforementioned schemes with CNTs has been impeded by rapid exciton decoherence [57], dephasing in an inhomogeneous environment [148], and blinking [18]. It has been shown in recent transport experiments that extrinsic effects can be successfully suppressed in as-grown suspended CNTs [163]. This approach was adopted for optical studies and samples with suspended wide-band gap CNTs were fabricated using CVD.

7.2 Sample layout

Suspended CNTs were synthesized (see Chapter 4) on commercial grids typically used in TEM. The grid[1] consisted of a silicon nitride membrane perforated with holes of 2 µm in diameter and a pitch of 4 µm supported by a silicon frame. The sample was coated with ~100 nm silicon oxide by plasma enhanced CVD[2] to ensure comparable growth conditions in terms of the substrate as for the previously investigated CNT growth process. CNTs were synthesized by CVD at a growth temperature of 850°C and a methane flow rate of 1.0 slm. The details can be found in Chapter 4.

Figure 7.1a shows optical micrographs of the sample for two different magnifications. The grid provided for suspension of CNTs in the region where the hole-perforated silicon nitride membrane was not supported by the underlying silicon frame (scanning electron micrograph and cross-section schematics in Figure 7.1b); this region appears yellowish in Figure 7.1a. In regions where the perforated membrane was in contact with the carrier frame lying beneath (blue regions in Figure 7.1a) CNTs were found to be suspended over the full diameter of the crater (Figure 7.1c) as well as having short suspended segments at the perimeter of the crater (Figure 7.1d). The following results were all observed from this latter region.

[1] *DuraSiN* Mesh for TEM, DTM-25233
[2] *Oxford* Plasmalab 80 Plus (PECVD)

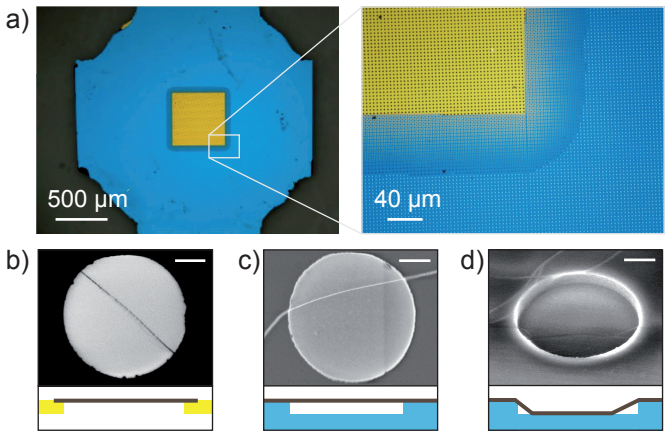

Figure 7.1: a) Optical microscopy images of a TEM grid used as sample substrate. A regularly hole patterned silicon nitride membrane lies on top of a silicon frame (blue region). In the central region the membrane is fully suspended with no substrate underneath (yellow region). Hole diameters are 2 µm, pitch is 4 µm. Scanning electron micrographs and cross-section schematics depict carbon nanotubes b) fully suspended over a hole, c) fully suspended over a crater, and d) partially pinned to the crater base. Scale bars in b–d are 500 nm.

7.3 Cryogenic photoluminescence spectroscopy

Individual craters of the sample were identified by scanning a finite area of a few µm^2 and recording the reflected signal of a diode laser at 905 nm wavelength. An exemplary confocal raster-scan reflection image and the corresponding PL map of a representative crater are shown in Figure 7.2a and b, respectively. Although intense PL was detected from the inner part of the crater, its outer rim exhibited only a faint PL signal. The spectral dispersion of the strong luminescence revealed a remarkably narrow emission line (Figure 7.2c) centered at 1.36 eV. This feature of a nearly resolution-limited linewidth (~40 µeV spectral resolution) was observed for all SWNTs detected in the emission window 1.30–1.45 eV (representative PL spectra are presented in Figure 7.2d). The spread in emission energies is related to the different chiralities present in the grown material from CVD with an average diameter of 1.0 nm (Chapter 4) and, for SWNTs of the same chirality, is related to dissimilarities in exciton confinement. Ideal SWNTs of five different chiralities, namely (7,0), (6,2), (6,4), (8,3), and (9,1) are expected to emit into the spectral window of Figure 7.2d.

The PL intensities displayed a pronounced antenna effect: Figure 7.3a displays a raster-scan reflection map of a crater and PL intensity maps of the same sample region obtained with the excitation laser linearly polarized parallel ($\parallel$) and perpendicular ($\perp$) to the CNT axis. While strong PL emission was observed from the inner rim of the crater using parallel polarization, no signal was detected with perpendicular excitation. The polar plot in Figure 7.3b depicts the PL intensity as a function of the angle between the laser polarization vector and the nanotube axis that is well described by a fit function with $\cos^2$-dependence (red curve in Figure 7.3b)—a characteristic feature of emission from a single SWNT [49] (cf. Chapter 5).

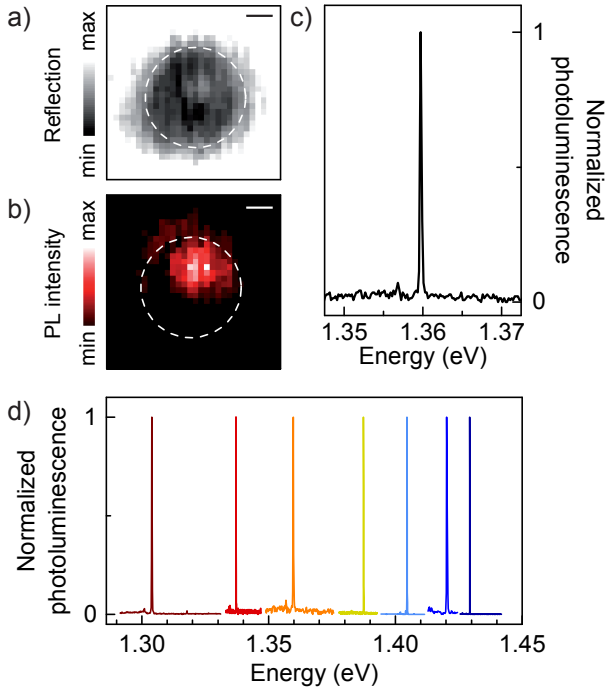

Figure 7.2: False color maps of a crater recorded in a) reflection and b) photoluminescence. Scale bars are 500 nm. c) Spectral dispersion of the photoluminescence in (b) reveals a sharp emission spectrum at 4.2 K. d) Exemplary photoluminescence spectra in the range 1.30–1.45 eV are represented in different colors, all exhibiting resolution-limited linewidths of ~40 µeV at 4.2 K.

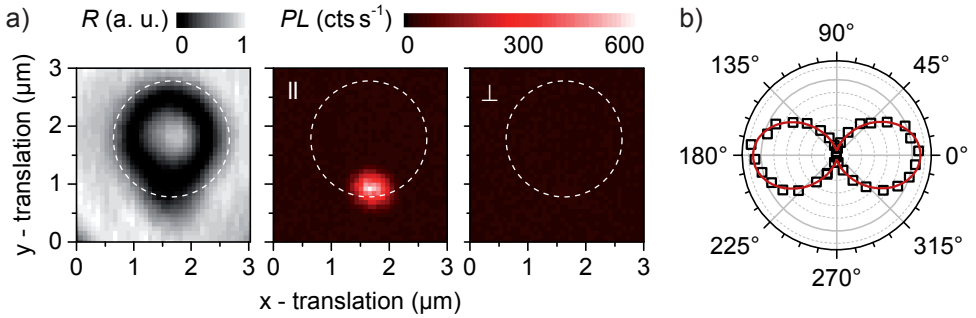

Figure 7.3: a) False-color map of a crater in reflection (*R*, left panel) and photoluminescence (*PL*) map of the same crater with laser polarization parallel (∥, middle panel) and perpendicular (⊥, right panel) to the nanotube axis. b) Polar plot of the photoluminescence intensity as a function of the angle between the laser polarization axis and the carbon nanotube axis. The red solid curve is a fit with $\cos^2$-dependence. All data were recorded at 4.2 K.

7.3.1 Photoluminescence excitation spectroscopy

Photoluminescence excitation was studied by tuning the frequency of the titanium-sapphire laser at a constant cw power. Figure 7.4a depicts the PL spectrum of a suspended CNT at 77 K with a narrow emission line (FWHM of 570 µeV) and the corresponding normalized PL intensity as a function of the laser detuning. Chromatic aberration of the optical setup[3] makes a quantitative analysis of PLE intensities difficult. In the presence of chromatic aberration, different focal planes are associated with different laser wavelengths. Therefore, the excitation intensity varies as a function of the laser wavelength. In consequence, PLE intensities depend on the specific optical alignment and are not comparable in terms of absolute intensity over the entire laser tuning window. To account for this effect, two sweeps of the laser wavelength were performed (dark and light blue traces in Figure 7.4a), each in a setup configuration optimized for the laser wavelength indicated by the asterisks. The data shown for the CNT in Figure 7.4a demonstrate that PLE resonances may appear strong or weak depending on the laser wavelength used to define the focal plane. In a given setting, however, both the intensity and the energy positions of individual resonances are reproducible from sweep to sweep. The resonances in the PLE intensity profile of Figure 7.4a resemble those of the as-grown SWNT on silica in Figure 5.6a. Peak positions around 160 meV and 200 meV are associated with the D- and G-modes, respectively. The resonance at ~160 meV, however, is composed of at least three sharp peaks. At further decreasing the sample temperature to 4.2 K, the PL linewidth reduced further to 230 µeV and the resonances in PLE became even more pronounced as depicted in Figure 7.4b. Several sharp resonances were also found in the PLE spectra in the range of ~30–300 meV accessible with the laser for other suspended CNTs. Figure 7.5 depicts two exemplary PL spectra and the corresponding PLE intensity profiles at 4.2 K. These specific cryogenic PLE spectra of as-grown suspended CNTs are inconsistent with the data of suspended CNTs in Section 5.3.2 and with previous reports that assigned absorption resonances to phonon sidebands [116, 117]. However, PLE profiles inconsistent with phonon-assisted absorption processes [116, 117] were already observed for as-grown CNTs on silica as in Section 5.2.2. In the particular case of the nanotube of Figure 5.7b, the PL at 4.2 K also exhibited a remarkably narrow emission line that was well approximated by a fit function that assumes localized excitons interacting with modified acoustic phonon-modes [119]. In light of these findings, the inconsistencies and dissimilarities in the PLE experiments can be explained by dissimilarities in exciton confinement and require further investigation from both experiment and theory.

[3] The measurements were performed using the aspheric lens described in Section 3.1.

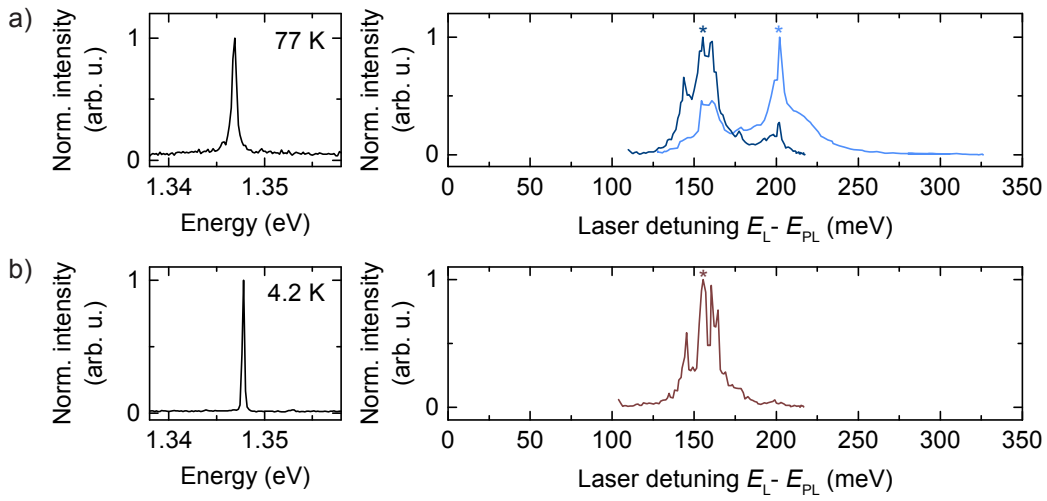

Figure 7.4: a) Emission spectrum (left panel) and corresponding photoluminescence excitation spectrum (right panel) of an as-grown suspended carbon nanotube at $T = 77\,\mathrm{K}$. Dark blue and light blue spectra were recorded with optical alignments optimized at laser detunings indicated by the asterisks. The variation between the traces is due to chromatic aberration of the optical setup. b) Emission spectrum and photoluminescence excitation spectrum of the same carbon nanotube at $T = 4.2\,\mathrm{K}$.

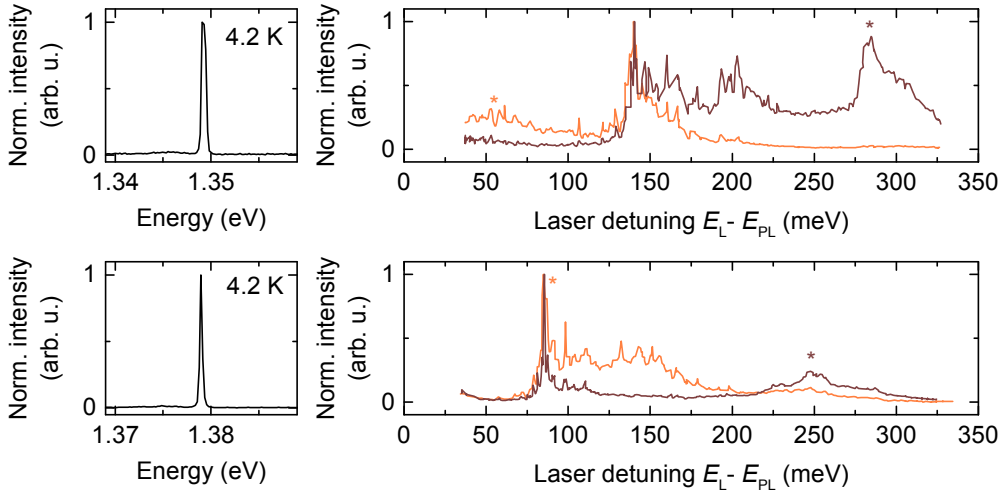

Figure 7.5: Emission spectra (left panels) and corresponding photoluminescence excitation spectra (right panels) of as-grown suspended carbon nanotubes at $T = 4.2\,\mathrm{K}$. Brown and orange spectra were recorded with optical alignments optimized at laser detunings indicated by the asterisks. The variation in photoluminescence excitation intensity between the traces is due to chromatic aberration of the optical setup.

7.3.2 Temporal evolution of the photoluminescence

Narrow optical linewidths are unusual for SWNTs, even at cryogenic temperatures [17, 19, 125]. For reference, as-grown CNTs in contact with SiO_2 as well as commercial micelle-encapsulated CoMoCAT-nanotubes dispersed on SiO_2 were studied. Under similar experimental conditions, CoMoCAT SWNTs typically exhibited asymmetric PL profiles [17,19,120] with linewidths of ~1 meV (Figure 7.6a), one order of magnitude broader than the CVD-grown SWNTs in 1 s integration time (Figure 7.6b,c). On longer experimental timescales, the linewidth of the time-averaged PL broadened even further for reference SWNTs (spectra in Figure 7.6g,h); suspended CNTs, however, showed no change in the emission profile, irrespective of the integration time (effective integration time of 100 s in Figure 7.6i and up to several days of observation). The PL time traces in Figure 7.6d–f reveal that spectral wandering is responsible for the broadening of the optical linewidth on a millielectronvolt energy scale, in accord with previous reports [17, 19, 54]. At the same time, it also accounts for the apparent fine structure [54, 125] and, to some

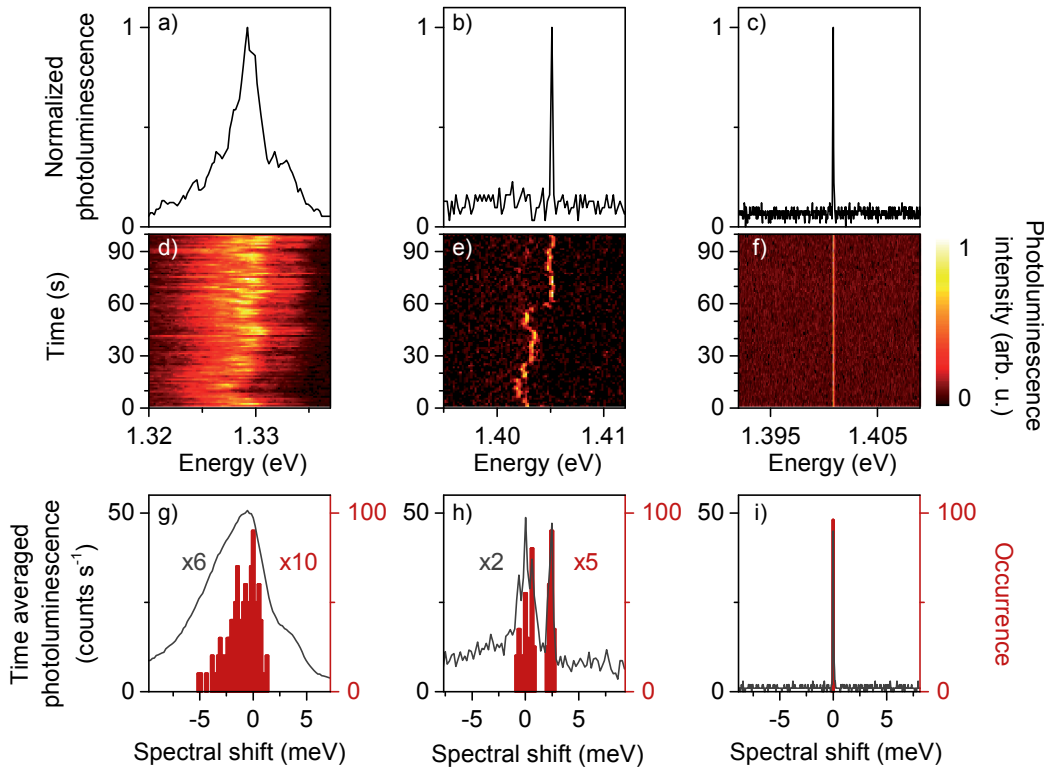

Figure 7.6: a) Photoluminescence spectra measured in 1 s for a commercial micelle-encapsulated CoMoCAT-nanotube on SiO_2, b) a single as-grown nanotube on SiO_2, and c) a single as-grown nanotube suspended over a SiO_2 crater. d,e,f) Corresponding time traces of successive photoluminescence spectra with 1 s integration time in false-color representation. g,h,i) Histograms of the position of the maximum photoluminescence (red bars) and time-averaged photoluminescence intensity (dark gray spectra) derived from the respective time traces are shown as a function of the spectral shift. All spectra were measured at 4.2 K.

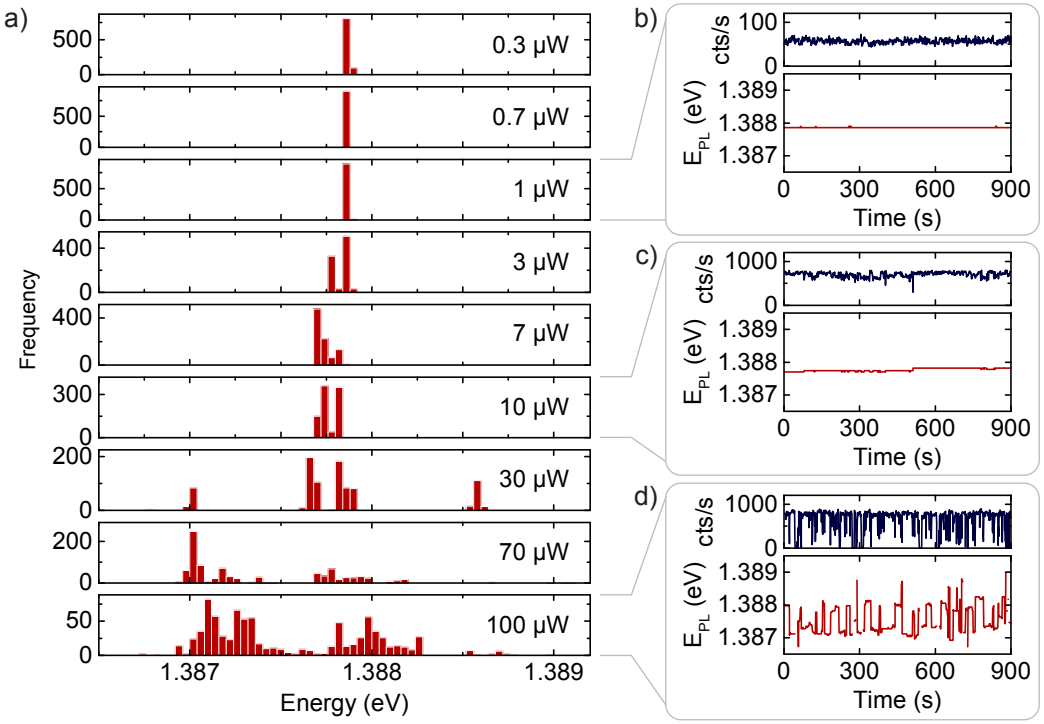

Figure 7.7: a) Histograms of the photoluminescence peak positions of a suspended CNT extracted from 900 consecutive emission spectra of 1 s integration time under pulsed laser excitation of various time-averaged excitation powers in the range 0.3–100 µW. Plots of the time evolution of the emission intensity (upper panel) and the photoluminescence energy E_{PL} (lower panel) are shown for excitation powers of b) 1 µW, c) 10 µW, and d) 100 µW.

extent, for the asymmetry in the spectral profile: the histograms in Figure 7.6g,h,i depict the emission peak positions obtained from the time traces in Figure 7.6d,e,f, respectively. While the CoMoCAT SWNT exhibited an asymmetric time-averaged PL spectrum and emission energy distribution (Figure 7.6g), an initially narrow spectrum of an as-grown CNT in contact with SiO_2 (Figure 7.6b) developed, in the course of integration, an asymmetric peak accompanied by a satellite (Figure 7.6h). For suspended CNTs, such detrimental features as spectral wandering were not observed (Figure 7.6c,f,i), as evidenced by both the time-averaged spectrum and the peak position histogram in Figure 7.6i.

However, a spectral jitter was induced by increasing the power of the excitation laser. Figure 7.7a depicts PL peak position histograms of a suspended CNT for several excitation powers of the pulsed laser in the range between 0.3 µW and 100 µW (time-averaged powers). At low excitation powers (0.3–1 µW), the emission featured a single PL peak with a resolution-limited linewidth stable in intensity and energy (Figure 7.7b). As the power was increased to moderate levels (~3–10 µW), the spectral emission line started to jitter on a submillielectronvolt energy scale without significant PL intensity intermittence (Figure 7.7c). High laser powers (30–100 µW) further enhanced the extent of spectral wandering with variations in emission energy on the order of 1 meV. At the same time, the PL switched rapidly between high and low intensities (Figure 7.7d).

The stable emission at low optical power densities is interpreted as a consequence

of the negligible influence of the substrate's distant charge reservoir on the localized excitons in suspended CNTs. It is known from PL measurements of CNTs in a gate structure that localized excitons can exhibit a permanent polarization and interact with nearby charges via a first-order Stark effect[4] [65], analogous to the observation of optical charge sensing in self-assembled quantum dots [164]. Here, at high optical power densities these charges can be created by Auger processes of diffusive excitons excited in the 1 µm wide focal spot of the laser. Subsequent charge trapping and fluctuations at the sites of disorder, possible adsorbates or dopants in the vicinity of an exciton localization center can therefore lead to Stark shifts of the exciton emission line and result in the observed spectral fluctuations. However, to further clarify the involved processes a detailed analysis of the spectral diffusion characteristics (e. g. via categorizing spectral fluctuations and noise) is required[5].

7.3.3 Time-resolved photoluminescence and photoluminescence saturation

In striking contrast to previous reports, decay times on the scale of nanoseconds, one order of magnitude longer than for the CoMoCAT reference material (red versus black circles in Figure 7.8b), were found for all suspended CNTs of narrow linewidth. A PL decay trace for a single CNT with a monoexponential decay time of 3.35 ns is shown in Figure 7.8a. Previous room-temperature experiments determined both monoexponential and biexponential decays depending on material quality, with PL decay times of the order of tens of picoseconds [165]. Similar results were obtained at low temperatures [21]. The light gray curve in Figure 7.8a is the PL decay curve of a micelle-encapsulated SWNT on silica at 4.2 K measured with the APD setup (cf. Section 3.3.3). The typical PL lifetime of the order of tens of picoseconds cannot be resolved by the APD and may thus be regarded as the instrument response function of the system.

The discrepancy between the 10–100 ps PL lifetimes observed experimentally and the radiative exciton lifetimes of 1–10 ns predicted by theory [63, 156, 157] is attributed to rapid non-radiative decay of mobile excitons encountering quenching sites [142]. The long PL lifetimes in these suspended SWNTs indicate that excitons are protected by localization from exploring PL quenching sites.

Following Perebeinos *et al.* [63,156] the intrinsic radiative lifetime τ_{rad} of CNT excitons is calculated as the inverse of the radiative decay rate Γ_{rad} as

$$\frac{1}{\tau_{\mathrm{rad}}} = \Gamma_{\mathrm{rad}} = \frac{n_r e^2 E_{11}^2 f}{2\pi\epsilon_0 m_0 \hbar^2 c^3}\,, \tag{7.1}$$

where ϵ_0 is the vacuum permittivity, m_0 is the free electron mass, e is the elementary charge, c is the speed of light, and $n_r = \sqrt{\epsilon}$ is the refractive index with ϵ =1.846 for a CNT in vacuum [166]. For a SWNT with chirality (n, m) and diameter d_t, the exciton emission energy is approximated by $E_{11} = \frac{0.84\,\mathrm{eV\,nm}}{d_t\,[\mathrm{nm}]}$ and the oscillator strength per carbon atom can be calculated by f =0.014 $\mathrm{eV}^{-1} E_{11} \pi d_t \sigma_c / A$ [63]. Here $A = \frac{3\sqrt{3}}{4} a_{C-C}^2$ is the area per

[4] The Stark shifted energy is $E = E_0 - \mathbf{p}\cdot\mathbf{F}$, where E_0 is the unperturbed energy, $\mathbf{p}$ is the dipole moment, and $\mathbf{F}$ is the electric field.

[5] J. Noé *et al.*, in preparation

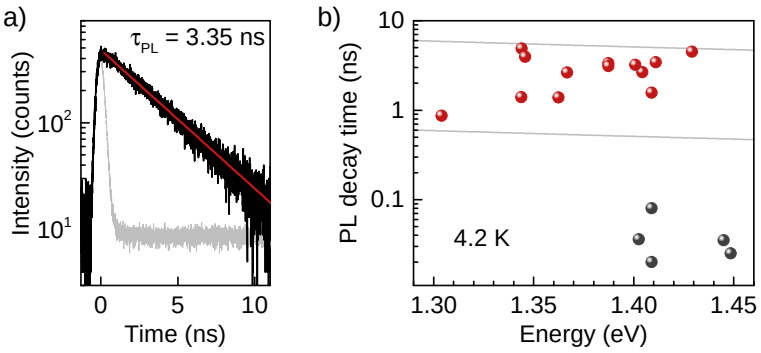

Figure 7.8: a) Monoexponential decay of an individual suspended as-grown carbon nanotube at 4.2 K with a decay time of τ_{PL} =3.35 ns (integration time: 600 s, excitation power: 7 µW, excitation wavelength: 827 nm). The light gray trace is the instrument response function. b) The photoluminescence lifetimes of suspended nanotube quantum dots are in the range of 1–5 ns (red circles), one order of magnitude longer than for surfactant-encapsulated CoMoCAT carbon nanotubes on SiO_2 (black circles, the low energy range was inaccessible for the streak camera). Limits of the radiative lifetime of excitons localized within their Bohr radius and free excitons are represented by the upper and lower gray lines, respectively.

carbon atom, and σ_c is the coherence length given by the confinement length in units of the exciton Bohr radius σ_X [166]. The values for the intrinsic exciton lifetimes obtained from Equation 7.1 are in good agreement with *ab initio* calculations by Spataru *et al.* [157] With this estimate, PL lifetimes on the scale of nanoseconds are in agreement with the radiative lifetimes estimated for excitons with coherence lengths in the range between the exciton Bohr radius of ~1.2 nm in narrow-diameter CNTs and the optical wavelength, as depicted by solid lines in Figure 7.8b.

Moreover, localization is also responsible for narrow emission profiles by inhibiting diffusive exploration of inhomogeneities along the CNT axis that would give rise to line broadening via dephasing. Taking the resolution limit of the spectrometer as a value for the total linewidth, the exciton coherence time in CNTs at 4.2 K is ~15 ps.

Further support for exciton localization is presented in Figure 7.9. In the time-resolved PL measurements no evidence was found for the exciton-exciton annihilation that is typically responsible for saturation effects in the emission of mobile CNT excitons [167]. Despite PL saturation for excitation intensities above 2 kW cm^{-2} (Figure 7.9b), the monoexponential PL lifetime remained constant without signatures of an emerging Auger-mediated rapid secondary decay, even for the highest laser powers (Figure 7.9a). Instead, the saturation behavior is consistent with the response of a three-level system that is modeled as follows.

Saturation of a three-level system

The temporal evolution of the crystal ground state $|0\rangle$ and the exciton ground and excited states $|X\rangle$ and $|X^*\rangle$, respectively, is described by a set of coupled rate equations:

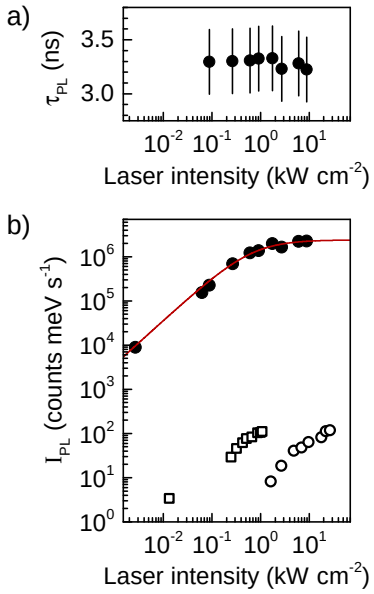

Figure 7.9: a) Photoluminescence lifetime τ_{PL} and b) integrated photoluminescence intensity I_{PL} as a function of the excitation laser intensity for the suspended single-walled carbon nanotube of Figure 7.8a (black solid circles). The red solid line is the saturation response of a three-level system fitted to the data. Open squares and circles are for representative CoMoCAT and as-grown carbon nanotubes on silica, respectively.

$$\begin{aligned}
\frac{\mathrm{d}}{\mathrm{d}t}\rho_0 &= -\rho_0\Gamma_{\mathrm{abs}} + \rho_X\Gamma_{\mathrm{rad}} \\
\frac{\mathrm{d}}{\mathrm{d}t}\rho_{X^*} &= \rho_0\Gamma_{\mathrm{abs}} - \rho_{X^*}\gamma_{\mathrm{rel}} \\
\frac{\mathrm{d}}{\mathrm{d}t}\rho_X &= \rho_{X^*}\gamma_{\mathrm{rel}} - \rho_X\Gamma_{\mathrm{rad}}
\end{aligned} \tag{7.2}$$

that is solved for steady-state, $\mathrm{d}\rho_i/\mathrm{d}t = 0$. In the set of equations, ρ_i denotes the population of state $|i\rangle$ with $\rho_0 + \rho_{X^*} + \rho_X = 1$, and Γ_{abs}, γ_{rel}, Γ_{rad} are the absorption, relaxation, and radiative recombination rates, respectively. For the population of the exciton ground state $|X\rangle$ one finds:

$$\rho_X = \frac{\Gamma_{\mathrm{abs}}}{\Gamma_{\mathrm{rad}} + \frac{\Gamma_{\mathrm{abs}}}{\gamma_{\mathrm{rel}}}\left(\Gamma_{\mathrm{rad}} + \gamma_{\mathrm{rel}}\right)} \tag{7.3}$$

which reduces in the limit $\gamma_{\mathrm{rel}} \gg \Gamma_{\mathrm{rad}}$ to

$$\rho_X = \frac{\Gamma_{\mathrm{abs}}}{\Gamma_{\mathrm{rad}} + \Gamma_{\mathrm{abs}}}\,. \tag{7.4}$$

This limit of fast relaxation as compared to the radiative emission is justified by linewidths of PLE resonances of the order of tens of meV corresponding to subpicosecond relaxation timescales. The PL intensity is proportional to the product of the excited

state population and the radiative decay rate, $I_{PL} \propto \Gamma_{rad}\rho_X$, with the proportionality factor given by the overall detection quantum efficiency. Normalizing the PL intensity by the constant value in saturation I_{PL}^{max} eliminates the detection efficiency and with Equation 7.4 one obtains:

$$\frac{I_{PL}}{I_{PL}^{max}} = \frac{\Gamma_{abs}}{\Gamma_{abs}+\Gamma_{rad}} . \tag{7.5}$$

The saturation is uniquely determined by the ratio of the radiative decay rate to the absorption rate. Finally, by relating the absorption rate Γ_{abs} to the excitation laser intensity $I_{laser} = \eta\Gamma_{abs}$ through the fitting parameter η one obtains the model response of a three-level system:

$$I_{PL} = I_{PL}^{max}\frac{I_{laser}}{I_{laser}+\eta\Gamma_{rad}} , \tag{7.6}$$

where the radiative recombination rate is experimentally obtained as the inverse PL lifetime, $\Gamma_{rad} = 1/\tau_{PL}$. The resulting fit (red solid line) to the data (solid circles) in Figure 7.9b yields I_{PL}^{max} =2.4 cts eV s^{-1} and η =2.2·10^{-9} $\frac{kW\,s}{cm^2}$ for the PL lifetime of τ_{PL} =3.35 ns.

7.3.4 Second-order photon correlation

Additional to the monoexponential decay rate and the saturation behavior, photon correlation results with pronounced antibunching both under continuous wave and pulsed excitation (Figure 7.10a) rule out multiexciton emission. In Figure 7.10a, the normalized second-order correlation function $g^{(2)}(\tau)$ of the SWNT under cw excitation was fitted with

$$g_{fit}^{(2)}(\tau) = 1 - \mathcal{A}\cdot\exp\left(-\frac{|\tau|}{\tau_{PL}}\right) , \tag{7.7}$$

where τ is the time delay between two successive photon detection events in the APDs of the Hanbury Brown and Twiss setup, τ_{PL} =3.35 ns is the exciton lifetime measured with time-resolved PL, and $\mathcal{A} = 1 - g^{(2)}(0) = 1 - 0.3 = 0.7$ is a fitting parameter representing the degree of photon antibunching.
In contrast, the second-order photon correlation function of the reference CoMoCAT CNT under pulsed laser excitation in Figure 7.10b showed side-peak bunching that is interpreted as the result of rapid PL blinking (i. e. switching between an "on" and "off" state) and was modeled based on the work of Santori *et al.* for blinking quantum dots [168]:

$$g^{(2)}(\tau) = 1 + \frac{\tau_{off}}{\tau_{on}}\cdot\exp\left(-|\tau|\left(\frac{1}{\tau_{on}}+\frac{1}{\tau_{off}}\right)\right) . \tag{7.8}$$

Here, τ_{on} and τ_{off} are the time constants for the luminescent and non-luminescent CNT states, respectively. Best fit parameters to the bunching data in Figure 7.10b were τ_{on} =340 ns and τ_{off} =160 ns.

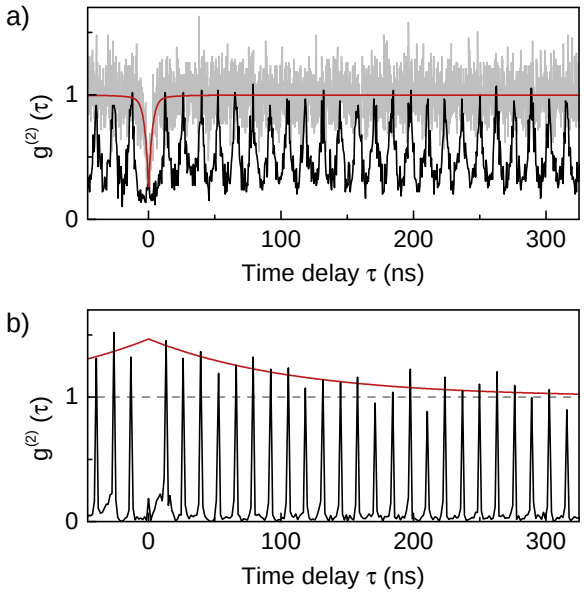

Figure 7.10: a) Normalized second-order photon correlation function $g^{(2)}(\tau)$ for a suspended as-grown carbon nanotube under pulsed (black) and continuous wave (gray) excitation. The pronounced antibunching at zero time delay is not accompanied by bunching as in the case of a b) CoMoCAT carbon nanotube on SiO_2. The absence of side-peak bunching is a hallmark of suppressed emission intermittence in suspended carbon nanotubes. To model the antibunching and bunching responses shown as red solid lines, parameters τ_{PL} =3.35 ns, $g^{(2)}(0)$ =0.3, and τ_{on} =340 ns, τ_{off} =160 ns were used in (a) and (b), respectively.

In summary, the consistency of the saturation behavior with the model for a three-level system implies the successful suppression of non-radiative PL quenching [142] and emission intermittence [18], as well as ineffective shelving into lowest-lying long-lived dark states [156, 157], rendering localized excitons in suspended CNTs intrinsically bright. The orders of magnitude higher values of saturated PL intensities as compared to reference CoMoCAT- and CVD-CNTs on substrate (Figure 7.9b), together with the missing signatures of photon bunching associated with PL intermittence (Figure 7.10) are strong indications for a significant increase in the quantum yield of localized excitons in suspended SWNTs.

7.4 Photoluminescence at 77 K and at room temperature

With the strong evidence for exciton localization in zero-dimensional trap states in suspended CNTs at 4.2 K it is of general interest for potential applications as quantum light sources how the observed features develop with increasing temperature. Trapping energies that exceed the thermal energy of $k_B T = 25$ meV at room temperature (k_B is the Boltzmann constant), could sufficiently preserve the localization of excitons and result in single-photon generation. Since the used microscopic setup did not allow for continuous temperature sweeps over large intervals, individual CNTs have been tried to track over the three temperatures accessible with the setup: temperatures of

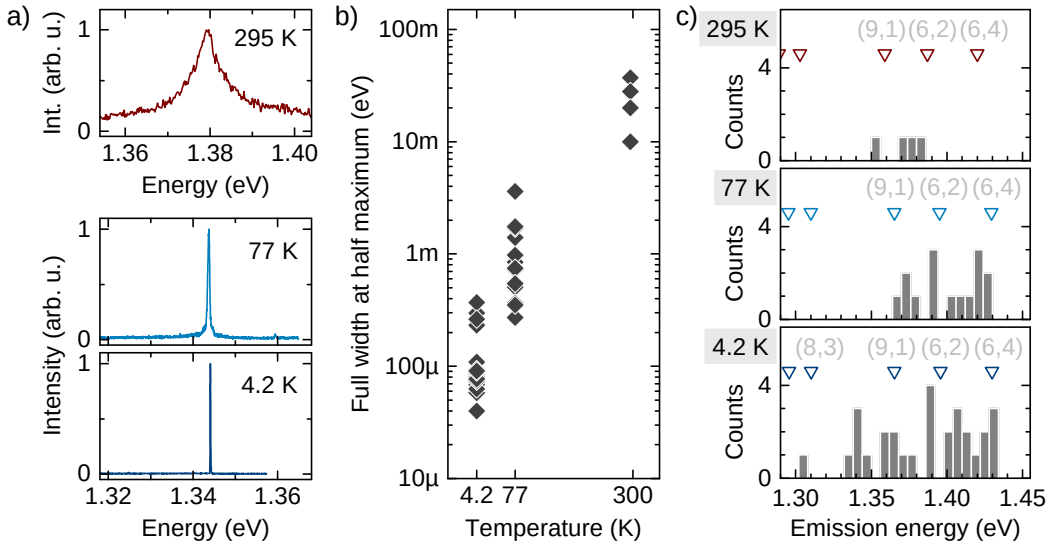

Figure 7.11: a) Exemplary emission spectra of carbon nanotubes at $T = 295\,\mathrm{K}$ (upper panel), 77 K (middle panel), and 4.2 K (lower panel). Note that the spectrum at 295 K was recorded on a different nanotube as the the spectra at 77 K and 4.2 K. b) Full width at half maximum of the photoluminescence emission spectra at 4.2 K, 77 K, and 295 K. c) Histograms of photoluminescence emission energies at $T = 295\,\mathrm{K}$ (upper panel), 77 K (middle panel), and 4.2 K (lower panel). The triangles mark photoluminescence energies estimated for small-diameter carbon nanotubes [32] taking into account the temperature dependent energy shift according to Ref. 151.

liquid helium (4.2 K) and liquid nitrogen (77 K), and room temperature (295 K). However, because the employed TEM grid did not feature a coordinate frame that would have allowed for local orientation on the sample, the temperature-dependent values of the piezo-steppers' resistive readout were correlated with the edges of the silicon frame from the inspection CCD image for course orientation. Thereby, it was possible to measure a few individual CNTs both at 4.2 K and 77 K. However, attempts on a closed set of data for a single CNT at all three temperatures were not successful due to loss of orientation upon the transition from 77 K to room temperature.

Representative PL spectra and spectral linewidths of suspended CNTs at temperatures of 4.2 K, 77 K, and 295 K are shown in Figure 7.11a and b, respectively. At 4.2 K, the PL linewidths of all as-grown suspended CNT were below the 400 µeV down to the resolution limit of the spectrometer (~40 µeV). An increase of the FWHM linewidth up to several millielectronvolts was observed at the temperature of 77 K. At room temperature, the linewidths were of the order of 10 meV, consistent with previous reports for suspended CNTs [125, 143].

Emission energies of all suspended CNTs studied in this work are summarized in histograms (bin size 6 meV) in Figure 7.11c. The figure also shows chirality-assigned PL emission energies using values at room temperature of Weisman and Bachilo [32] that were corrected for temperature-induced band gap shifts for 77 K and 4.2 K according to Capaz *et al.* [151] Further corrections to the emission energy due to strain or details of the confinement potential and of the specific dielectric environment were not

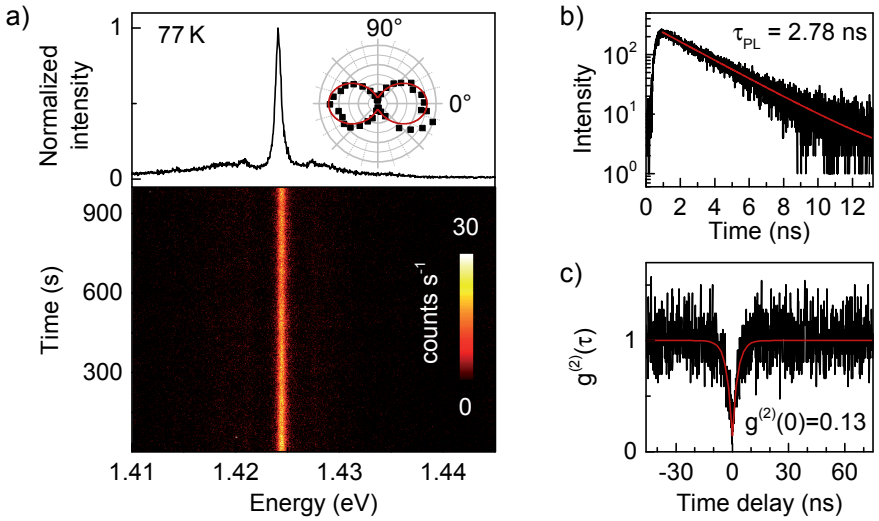

Figure 7.12: a) Upper panel: Photoluminescence spectrum with a full width at half maximum of 720 µeV of a suspended as-grown carbon nanotube at 77 K. The photoluminescence intensity displays a pronounced antenna effect (inset). The red solid line is a fit with $\cos^2$-dependence. Lower panel: A time trace of the spectrum reveals that the emission line is free of spectral wandering and intensity blinking. b) The photoluminescence decay curve is fitted with a mono-exponential function (red solid line). c) The dip in the normalized second-order correlation function $g^{(2)}(\tau)$ at zero time delay, τ=0, reveals single-photon emission under continuous wave laser excitation. The fit function (red solid line) yields a multiple photon emission probability of $g^{(2)}(0)$=0.13.

considered.

The PL spectrum of an as-grown suspended CNT at 77 K with a FWHM of 720 µeV as well as a polar plot of the characteristic $\cos^2$-dependence of the PL intensity on the linear excitation laser polarization is depicted in the upper panel of Figure 7.12a. The emission stability in terms of intensity blinking and spectral jitter under constant laser irradiation (839 nm, 2.5 µW) over several minutes of observation is one of the conserved features at 77 K as shown in the time trace in the lower panel of Figure 7.12a. Also, as for 4.2 K, the exciton lifetimes were found to be in the nanoseconds time range (PL decay curve and monoexponential fit in Figure 7.12b). Additionally, pronounced photon antibunching was observed. The results are not surprising when considering the relevant thermal energy: 77 K corresponds to $k_B T = 6.6$ meV which is still insufficiently large to effectively depopulate trapping states of moderate depth with tens of millielectronvolts in trapping energy (cf. Chapter 6).

Although a closed set of data was not achieved and the data from room temperature measurements in this setting is sparse, the result is remarkable. The room temperature emission as shown in Figure 7.13a was free of intensity blinking and spectral wandering (time trace in the lower panel of Figure 7.13a) suggesting an effective protection against environmental fluctuations. This assumption is further strengthened by the $g^{(2)}$-measurement from fs-pulsed laser excitation (819 nm, 50 µW time-averaged power) presented in Figure 7.13b. The absence of side-peak bunching excludes the rapid switching between a bright (on) and dark (off) state on submicrosecond timescales [18, 168].

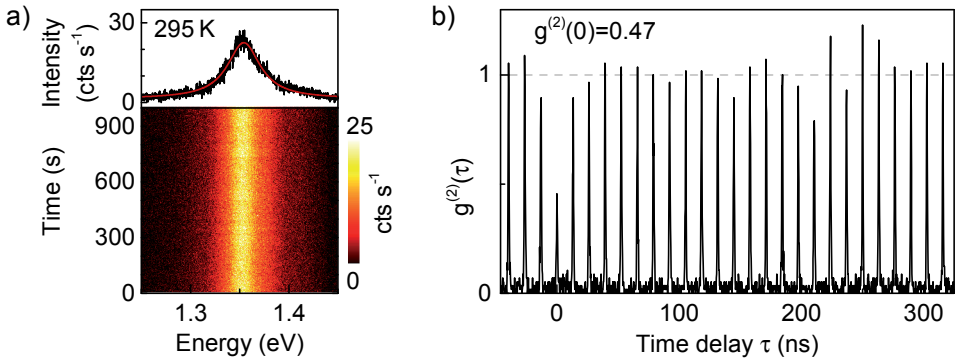

Figure 7.13: a) Upper panel: Single photoluminescence spectrum of an as-grown suspended carbon nanotube at room temperature T=295 K. Lower panel: False-color plot of successive photoluminescence spectra recorded at 1 s integration time showing that the emission is free of spectral wandering and intensity blinking. b) The second-order photon correlation trace $g^{(2)}$ for pulsed laser excitation reveals moderate photon antibunching with a value of $g^{(2)}(0)$=0.47 and no signatures of side-peak bunching from rapid intensity blinking. (Excitation: 819 nm and 50 µW time-averaged laser power, time resolution: 256 ps, integration time: 6.1 h)

Most remarkable, however, is the signature of photon antibunching. Although a clear dip in the $g^{(2)}$-trace is present at zero time delay, the degree of antibunching was moderate ($1-g^{(2)}(0)=1-0.47=0.53$) suggesting suppressed multiphoton emission that may be due to multiple single-photon emission sites within the investigated sample spot. In fact, a $g^{(2)}(0)$ value of 0.5 corresponds to two independent quantum emitters [169]. Indeed, the spectrum in Figure 7.13a is slightly asymmetric with a weak shoulder on the blue side of the main emission peak that supposedly adds to the photon statistics. Similar values for $g^{(2)}(0)$ have been reported recently by Endo *et al.* in a very similar experimental setting and have been explained by multi-domain carrier confinement from amorphous carbon contamination [170].

Even though the PL lifetime τ_{PL} was not directly measured by time-resolved PL, conclusions can be drawn from the correlation peaks in Figure 7.13b. Since the peaks' slope in a pulsed $g^{(2)}$-measurement reflects the exciton lifetime, an upper bound for τ_{PL} was extracted by monoexponential fits and found to be ≤500 ps. This decrease in exciton lifetime as compared to the observed PL decay times at cryogenic temperatures is in agreement with the findings for dopant-induced trap states [137].

7.5 Conclusion

The results establish bright, long-lived, and coherent quantum dot excitons as a new regime of carbon nanotube optics. Exciton localization emerged naturally in the presented as-grown suspended carbon nanotubes, and the underlying microscopic origin is currently unknown. Analogous to color defects in bulk crystalline solids with discrete optical spectra, luminescent structural defects may constitute a class of quantum dots in semiconducting carbon nanotubes. Another candidate for accidental exciton

trap formation would be a proximal charge impurity [171]. However, there is no fundamental reason that precludes quantum dot formation by design: electrostatic traps are commonly used in carbon nanotube transport experiments to define and vary the localization of electrons or holes, a strategy also applicable to neutral excitons [123]. Chemical functionalization of the carbon nanotube or its structural modification on the atomic scale, as recently used for room temperature single-photon generation from doped carbon nanotubes [137], are among alternative strategies to control the position and extent of exciton localization in carbon nanotubes.

Chapter 8

Summary and perspectives

By virtue of strongly bound electron-hole pairs (excitons) with photoluminescence (PL) up to room temperature and tuneable emission wavelengths from the near-infrared (~830 nm) to the telecommunication bands, semiconducting single-walled carbon nanotubes (CNTs) have attracted strong interest for photonic and optoelectronic applications [8]. The recent discovery of single-photon emission caused by exciton localization at cryogenic temperatures have made nanotubes also promising for application in quantum photonics [17, 18]. Since CNTs are nanoscale objects with large aspect ratios (typically 1000:1) and high surface-to-volume ratios, they are highly sensitive to extrinsic and environmental perturbations and their PL commonly suffers from fundamental drawbacks for quantum light applications such as strong spectral jittering, intensity blinking, or a much more rapid decay than theoretically expected.

In the framework of this thesis, chemical vapor deposition (CVD) was employed to fabricate samples with as-grown CNTs in order to overcome the challenges of enhancing nanotube PL. The CVD setup was based on methane as the carbon feedstock supplemented by hydrogen and alumina-supported iron-ruthenium nanoparticles that catalyzed CNT synthesis at elevated temperatures. Two major accomplishments enabled analysis of the optical properties: First, the excitation and detection spot size of 1 µm of the home-built cryogenic confocal microscope required spatially isolated CNTs for single-tube spectroscopy. Second, due to the inverse diameter-dependence of CNT emission energies and the limited performance in the near-infrared spectral range of the employed silicon-based photodetectors, which however offered favorable characteristics in terms of low noise and high quantum-yield, a significant fraction of subnanometer-diameter CNTs with wide band gaps had to be grown. The systematic study in *Chapter 4* identified growth parameters that control the average length, diameter, and areal density of CNTs grown on silica substrates. Furthermore, analysis of the intensity ratios of the vibrational G- and D-mode from cryogenic Raman spectroscopy of individual as-grown CNTs fully suspended over holes indicated that ~50 % of the synthesized CNTs were of high structural quality.

Using synthesis conditions that favored the growth of CNTs with subnanometer diameters, samples with spatially isolated as-grown CNTs in contact with a silica substrate as well as CNTs suspended over holes of a perforated membrane were fabricated for optical investigations (*Chapter 5*). While spectral wandering and PL intensity fluctuations on the second timescale were observed for on-substrate CNTs, these features were

drastically reduced in the PL of suspended as-grown CNTs with symmetric emission peaks. Additionally, distinct resonances in photoluminescence excitation spectra were observed for suspended CNTs and assigned to efficient phonon-assisted absorption processes. These resonances were found to be less pronounced for cryogenic CNTs in contact with the silica surface. Effects of modified exciton-phonon coupling were also identified by spectral line shape modeling of the cryogenic CNT-on-silica PL spectra. That the applied model [119] relies on coupling of a localized exciton to a locally modified acoustic phonon reservoir underlines the importance of substrate-induced perturbations on CNT excitons.

In order to investigate the characteristics of exciton localization in more detail, the PL of micelle-encapsulated HiPco and CoMoCAT CNTs as well as the emission from unprocessed CNTs by CVD was studied by confocal microscopy. As described in *Chapter 6*, hyperspectral mapping at three fixed temperatures (295 K, 77 K, and 4.2 K) revealed disorder-induced crossover from the diffusive exciton regime at room temperature to localized excitons at cryogenic temperatures. Spatial PL fragmentation into emission hotspots, spectral variations along the CNT axis, and the emergence of multi-peak PL were identified as main features of exciton localization. By comparing the thermal evolution of the spectrally dispersed PL with theoretical expectations, both at the level of individual CNTs and ensembles, the energy scale of unintentional exciton trap potentials was quantified to be as deep as 50–60 meV and found to be a common feature of the three CNT materials studied. Moreover, the sensitivity of CNT excitons to their immediate surrounding was also highlighted by the *in situ* observation of a laser-induced desorption process with cryogenic PL spectroscopy.

In *Chapter 7* the CNTs to be investigated were synthesized by CVD on a perforated membrane lying on top of a dielectric substrate and features suspended segments over the substrate's craters. At 4.2 K the PL from these structures exhibited emission linewidths of the order of a few hundred microelectronvolts down to the resolution limit of the spectrometer (~40 µeV). As opposed to the reference CoMoCAT CNTs on silica with broad and asymmetric spectral profiles, these narrow optical lines showed strongly suppressed spectral diffusion on the second timescale and were free of intensity fluctuations at moderate excitation powers. While the PL of reference CNTs decays rapidly, on the order of 10–100 ps, the PL lifetime of these suspended CNT excitons was found to be prolonged to a few nanoseconds as predicted by theory [63, 156, 157]. The experimental observations suggest that these excitons are highly isolated from environmental perturbations and are spatially protected from PL quenching sites that are typically encountered in the diffusive regime. Indeed, the observation of strong photon antibunching in second-order photon correlation measurements as well as the absence of a rapid Auger-mediated decay in the PL saturation limit illustrate that excitons are localized in a quasi zero-dimensional CNT quantum dot structure. In addition to that, the absence of photon bunching signatures associated with two-state submicrosecond blinking is a strong indication of ineffective shelving into low-energy, long-lived dark states, rendering localized excitons in suspended CNTs intrinsically bright.

In conclusion, the results achieved by CVD and optical spectroscopy establish exciton localization as a general feature of cryogenic CNTs and can be generalized to other low-dimensional semiconductors with large surface-to-volume ratios such as the emergent class of transition metal dichalcogenides. The comprehensive analysis of spectral

signatures highlights the importance of crystalline and environmental disorder for CNT photophysics. On the one hand, this photo-sensitivity can have detrimental effects on the emission characteristics, in turn hindering successful implementation of nanotubes in photonic devices. On the other hand, it bears significant potential for sensing. As an example of the latter, CNTs positioned at the tip of an AFM cantilever may be utilized as optical charge sensors in a scanning electrometer device where the nanotube exciton is used to detect charges in the specimen via Stark shifts of its energy state.

For the case of suspended CNTs, two distinct regimes of CNT emission characterized by spectrally broad and narrow exciton PL were observed. In the latter regime, spectral linewidths as narrow as the resolution limit of the employed spectrometer indicate a timescale of ~15 ps for the exciton coherence in as-grown suspended CNTs at cryogenic temperatures and were assigned as stemming from localized excitons. However, similarly narrow emission spectra have been attributed to the material quality rather than to exciton localization [126]. It is plausible that both exciton localization and environmental inhomogeneities at CNT side-walls play pivotal roles in determining the spectral characteristics of the CNT exciton PL. The individual contributions and their potential interplay, however, are to be substantiated in follow-up experiments on as-grown suspended CNTs with *in situ* monitoring a controlled crossover from the diffusive to the localized exciton regime [137]. Additionally, as demonstrated in Chapter 5, magneto-PL constitutes a viable complementary investigation of the nanotube emission spectrum. The use of a magnetic field to redistribute the spectral weights among bright and dark CNT excitons may shed light on the origin and specific excitonic state responsible for the observed narrow emission lines. Ultimately, access to CNTs with spectrally narrow non-classical light emission from localized excitons will constitute a crucial step towards the realization of nanotube-based sources of indistinguishable photons [172]. Moreover, CNT quantum dots from controlled fabrication, as can be envisioned by chemical functionalization [135–137, 139, 140], atomic-scale structural modification [173], or controlled inhomogeneous electric fields by static gates [123] may also provide a platform for spintronics: In contrast to quantum dots of GaAs where millions of interacting nuclear spins act as an incoherent bath, nanotubes of purified ^{12}C atoms constitute a nuclear-spin free material that promises long spin coherence times for quantum information processing. Additionally, isotopically engineered ^{12}CNT lattices with few ^{13}C impurities of nuclear spin $\frac{1}{2}$ could enable all-optical manipulation and coupling of spin degrees of freedom [138, 174] where single ^{13}C nuclei could be used to store quantum information on technologically relevant timescales.

Appendix A

Diameter distributions of as-grown carbon nanotubes

The CNT diameter distributions obtained by AFM for samples grown with the CVD method as described in Section 4.2 are depicted in Figure A.1. Each data histogram was fitted by the log-normal distributional fit function

$$f_{\text{fit}}(x) = \frac{A}{x\sigma\sqrt{2\pi}} \exp\left[-\frac{1}{2\sigma^2}\left(\log x - \mu\right)^2\right], \quad x > 0\,, \tag{A.1}$$

where x is the random variable, A is the area under the graph of $f(x)$ and μ and σ can be called the location parameter and the scale parameter, respectively. Common statistics of the log-normal distribution are listed below:

- $\text{Mean}[x] = e^{\mu+0.5\sigma^2}$
  The arithmetic mean is sensitive to outliers. Therefore, it is not a robust statistic.
- $\text{Mode}[x] = e^{\mu-\sigma^2}$
  The mode is the point of global maximum of the probability density function.
- $\text{Med}[x] = e^{\mu}$
  The median is the value that separates the lower half from the higher half of a distribution. It is the same as the second quartile and is a robust statistic. For the skewed log-normal distribution, the median may be a better description of central tendency than the arithmetic mean.
- $\text{Var}[x] = \left(e^{\sigma^2} - 1\right)\sqrt{e^{\sigma^2} - 1}$
  is the variance.
- $\text{Skew}[x] = \left(e^{\sigma^2} + 2\right)\sqrt{e^{\sigma^2} - 1}$
  The skewness is a measure of asymmetry of the distribution.

Table A.1 shows the values of the median, mean, and mode as well as the variance and the skewness of the log-normal distributions fitted to the diameter histograms for the investigated CVD growth parameters.

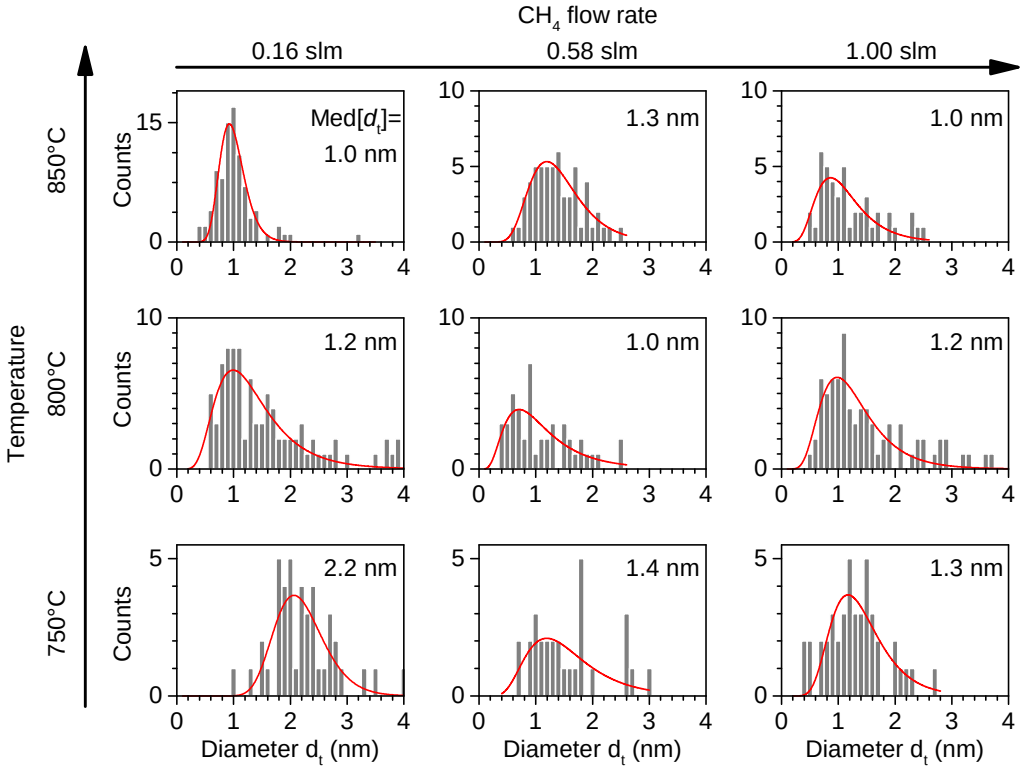

Figure A.1: Carbon nanotube diameter distributions for temperatures of 750°C, 800°C, and 850°C as well as for methane flow rates of 0.16 slm, 0.58 slm, and 1.00 slm. Median values Med[d_t] of the skewed data histograms were extracted from log-normal distributional fits (red solid curves).

Temperature	CH_4 flow rate (slm)	mean (nm)	mode (nm)	median (nm)	variance	skewness
850°C	0.16	1.00	0.93	0.97	0.05	0.70
	0.58	1.43	1.19	1.35	0.27	1.13
	1.00	1.13	0.86	1.03	0.25	1.41
800°C	0.16	1.36	0.99	1.22	0.43	1.56
	0.58	1.14	0.71	0.97	0.49	2.08
	1.00	1.29	0.98	1.18	0.33	1.43
750°C	0.16	2.20	2.06	2.15	0.21	0.63
	0.58	1.58	1.19	1.44	0.51	1.45
	1.00	1.41	1.17	1.33	0.27	1.15

Table A.1: Listed values of the mean, mode, and median as well as the variance and the skewness of the log-normal distributional fits to the carbon nanotube diameter histograms in Figure A.1.

Appendix B

Sample fabrication by optical lithography

Cleaning of the Si/SiO_2 sample surfaces

- Bath-sonication (*Bandelin* Sonorex Super, power level: 100 %) in acetone: 5 min.
- Bath sonication in isopropyl alcohol: 2 min.
- Blow-drying with nitrogen.
- Oxygen plasma treatment.
  Plasma etcher (*LabAsh 100*) parameters: 2 torr, 50 W, 180 s.

Optical lithography

- Spin-coating of the sample surface with an image reversal photoresist (*Clariant* AZ 5214E).
  Spread time: 3 s at 800 rpm, spin time: 30 s at 3000 rpm.
- Edge bead removal (optional).
- Resist prebake on a hotplate: 110°C, 50 s.
- Positioning of the inverted shadow mask on the coated sample surface using the mask aligner (*Karl Suss* MJB3).
- Exposure (UV light): 15 s.
- Wait for 5 min.
- Reversal bake on a hotplate: 120°C, 120 s.
- Wait for 5 min.
- Flood exposure (UV light, without shadow mask): 40 s.
- Agitation in developer (*Clariant* AZ 351B, dilution 1:3): 40 s.
- Agitation in deionized water: 20 s.
- Blow-drying with nitrogen.

Reactive ion etching

Parameters of the parallel plate reactive ion etching system:

- CF_4 flow rate: 20 sccm
- Power: 80 W
- Duration of etching step: 15 min

Removal of remaining photoresist

- Bath-sonication in acetone: 5 min.
- Bath sonication in isopropyl alcohol: 2 min.
- Blow-drying with nitrogen.
- Oxygen plasma treatment.
  Plasma etcher parameters: 2 torr, 50 W, 180 s.

Appendix C

Temperature dependence of the band gap

According to Ref. 151 the temperature dependence of the band gap E_g of semiconducting SWNTs was approximated by a two-phonon Viña model [152] as:

$$\Delta E_g(T) = E_g(T) - E_g(0) = \frac{\alpha_1 \Theta_1}{e^{\Theta_1/T} - 1} + \frac{\alpha_2 \Theta_2}{e^{\Theta_2/T} - 1}\,, \tag{C.1}$$

where Θ_1 and Θ_2 are effective temperatures of the two "average phonons", and $\alpha_j \Theta_j$ are the effective coupling coefficients of the electron-phonon interactions. The coefficients can be calculated with the polynomial expansion $f_\eta(\xi) = \gamma_1^\eta \xi + \gamma_2^\eta \xi^2$ of the variable $\xi = (-1)^\nu \cos 3\theta$ that accounts for chirality by $\nu = (n-m) \mathrm{mod}(3)$:

- $\Theta_1 = A/d^2$
  where the parameter $A = 9.45 \cdot 10^3$ K and $d = \sqrt{n^2 + nm + m^2}$ is the dimensionless nanotube diameter
- $\alpha_1 = \alpha_1^0 + f_{\alpha_1}(\xi) d$
  where $\alpha_1^0 = -1.70 \cdot 10^{-5}$ eV/K, $\gamma_1^{\alpha_1} = 1.68 \cdot 10^{-6}$ eV/K and $\gamma_2^{\alpha_2} = 6.47 \cdot 10^{-7}$ eV/K
- $\Theta_2 = \Theta_2^\infty + \frac{f_{\Theta_2}(\xi)}{d}$
  where $\Theta_2^\infty = 470$ K, $\gamma_1^{\Theta_2} = 1.06 \cdot 10^3$ K and $\gamma_2^{\Theta_2} = -5.94 \cdot 10^{-2}$ K
- $\alpha_2 = \frac{1}{d}\left(B + \frac{f_{\alpha_2}(\xi)}{d}\right)$
  where $B = -4.54 \cdot 10^{-4}$ eV/K, $\gamma_1^{\alpha_2} = -2.68 \cdot 10^{-3}$ eV/K and $\gamma_2^{\alpha_2} = -2.23 \cdot 10^{-5}$ eV/K

The calculated values for the coefficients α_1, Θ_1, α_2, and Θ_2 as well as the determined energy shift at room temperature $\Delta E_g(295\,K) = E_g(295\,K) - E_g(0)$ for various small diameter SWNTs are tabulated in Table C.1.

(n,m)	α_1 (10^{-5} eV/K)	Θ_1 (10^2 K)	α_2 (10^{-5} eV/K)	Θ_2 (10^2 K)	ΔE_g(295 K) (meV)
(5,4)	-1.93	1.55	-4.98	4.44	-10.64
(6,2)	-2.34	1.82	-2.47	3.60	-8.73
(6,4)	-1.14	1.24	-6.40	5.11	-9.74
(6,5)	-1.94	1.04	-4.30	4.53	-10.11
(7,0)	-2.42	1.93	-1.06	3.19	-6.80
(7,3)	-2.41	1.20	-2.98	3.95	-9.96
(7,5)	-1.15	0.87	-5.05	4.99	-8.60
(7,6)	-1.94	0.74	-3.75	4.58	-9.64
(8,1)	-2.57	1.29	-1.84	3.52	-8.85
(8,3)	-0.24	0.97	-6.54	5.45	-7.27
(9,1)	0.42	1.04	-7.62	5.77	-6.22

Table C.1: Coefficients of the temperature dependent band gap energy E_g and the band gap shift at room temperature for several nanotube chiralities calculated according to Ref. 151.

Bibliography

[1] nan'o·tech·nol'o·gy *n. Nature Nanotechnology* **1**, 8–10 (2006).

[2] Saito, R., Dresselhaus, G. & Dresselhaus, M. S. *Physical Properties of Carbon Nanotubes* (Imperial College Press, London, 1998).

[3] Zhang, R. *et al.* Growth of half-meter long carbon nanotubes based on Schulz-Flory distribution. *ACS Nano* **7**, 6156–6161 (2013).

[4] Dresselhaus, M. S., Dreselhaus, G. & Avouris, P. (eds.) *Carbon Nanotubes: Synthesis, Structure, Properties, and Applications* (Springer-Verlag Berlin Heidelberg New York, 2001).

[5] De Volder, M. F. L., Tawfick, S. H., Baughman, R. H. & Hart, A. J. Carbon nanotubes: Present and future commercial applications. *Science* **339**, 535–539 (2013).

[6] Wang, F., Dukovic, G., Brus, L. E. & Heinz, T. F. The optical resonances in carbon nanotubes arise from excitons. *Science* **308**, 838–841 (2005).

[7] Maultzsch, J. *et al.* Exciton binding energies in carbon nanotubes from two-photon photoluminescence. *Physical Review B* **72**, 241402 (2005).

[8] Avouris, P., Freitag, M. & Perebeinos, V. Carbon-nanotube photonics and optoelectronics. *Nature Photonics* **2**, 341–350 (2008).

[9] Mueller, T. *et al.* Efficient narrow-band light emission from a single carbon nanotube p-n diode. *Nature Nanotechnology* **5**, 27–31 (2010).

[10] Wang, S. *et al.* High-performance carbon nanotube light-emitting diodes with asymmetric contacts. *Nano Letters* **11**, 23–29 (2011).

[11] Freitag, M., Martin, Y., Misewich, J. A., Martel, R. & Avouris, P. Photoconductivity of single carbon nanotubes. *Nano Letters* **3**, 1067–1071 (2003).

[12] Pradhan, B., Setyowati, K., Liu, H., Waldeck, D. H. & Chen, J. Carbon nanotube-polymer nanocomposite infrared sensor. *Nano Letters* **8**, 1142–1146 (2008).

[13] Lu, R., Christianson, C., Kirkeminde, A., Ren, S. & Wu, J. Extraordinary photocurrent harvesting at type-II heterojunction interfaces: Toward high detectivity carbon nanotube infrared detectors. *Nano Letters* **12**, 6244–6249 (2012).

[14] Lee, J. U. Photovoltaic effect in ideal carbon nanotube diodes. *Applied Physics Letters* **87**, 073101 (2005).

[15] Chen, C., Lu, Y., Kong, E. S., Zhang, Y. & Lee, S.-T. Nanowelded carbon-nanotube-based solar microcells. *Small* **4**, 1313–1318 (2008).

[16] Wang, S. *et al.* Photovoltaic effects in asymmetrically contacted CNT barrier-free bipolar diode. *Journal of Physical Chemistry C* **113**, 6891–6893 (2009).

[17] Högele, A., Galland, C., Winger, M. & Imamoğlu, A. Photon antibunching in the photoluminescence spectra of a single carbon nanotube. *Physical Review Letters* **100**, 217401 (2008).

[18] Walden-Newman, W., Sarpkaya, I. & Strauf, S. Quantum light signatures and nanosecond spectral diffusion from cavity-embedded carbon nanotubes. *Nano Letters* **12**, 1934–1941 (2012).

[19] Htoon, H., O'Connell, M. J., Cox, P. J., Doorn, S. K. & Klimov, V. I. Low temperature emission spectra of individual single-walled carbon nanotubes: Multiplicity of subspecies within single-species nanotube ensembles. *Physical Review Letters* **93**, 027401 (2004).

[20] Matsuda, K. *et al.* Photoluminescence intermittency in an individual single-walled carbon nanotube at room temperature. *Applied Physics Letters* **86**, 123116 (2005).

[21] Hagen, A. *et al.* Exponential decay lifetimes of excitons in individual single-walled carbon nanotubes. *Physical Review Letters* **95**, 197401 (2005).

[22] Jorio, A. *et al.* G-band resonant Raman study of 62 isolated single-wall carbon nanotubes. *Physical Review B* **65**, 155412 (2002).

[23] Araujo, P. T. *et al.* Nature of the constant factor in the relation between radial breathing mode frequency and tube diameter for single-wall carbon nanotubes. *Physical Review B* **77**, 241403 (2008).

[24] Kobayashi, Y., Takagi, D., Ueno, Y. & Homma, Y. Characterization of carbon nanotubes suspended between nanostructures using micro-Raman spectroscopy. *Physica E: Low-dimensional Systems and Nanostructures* **24**, 26–31 (2004).

[25] Lee, S., Peng, J.-W. & Liu, C.-H. Probing plasma-induced defect formation and oxidation in carbon nanotubes by Raman dispersion spectroscopy. *Carbon* **47**, 3488–3497 (2009).

[26] Georgi, C. & Hartschuh, A. Tip-enhanced raman spectroscopic imaging of localized defects in carbon nanotubes. *Applied Physics Letters* **97**, 143117 (2010).

[27] Irurzun, V. M., Ruiz, M. P. & Resasco, D. E. Raman intensity measurements of single-walled carbon nanotube suspensions as a quantitative technique to assess purity. *Carbon* **48**, 2873–2881 (2010).

[28] Dresselhaus, M., Dresselhaus, G., Saito, R. & Jorio, A. Raman spectroscopy of carbon nanotubes. *Physics Reports* **409**, 47–99 (2005).

[29] Svensson, J. & Campbell, E. E. B. Schottky barriers in carbon nanotube-metal contacts. *Journal of Applied Physics* **110**, 111101 (2011).

[30] Ajiki, H. & Ando, T. Aharonov-Bohm effect in carbon nanotubes. *Physica B: Condensed Matter* **201**, 349–352 (1994).

[31] Miyauchi, Y., Oba, M. & Maruyama, S. Cross-polarized optical absorption of single-walled nanotubes by polarized photoluminescence excitation spectroscopy. *Physical Review B* **74**, 205440 (2006).

[32] Weisman, R. B. & Bachilo, S. M. Dependence of optical transition energies on structure for single-walled carbon nanotubes in aqueous suspension: An empirical Kataura plot. *Nano Letters* **3**, 1235–1238 (2003).

[33] Saito, R., Dresselhaus, G. & Dresselhaus, M. S. Trigonal warping effect of carbon nanotubes. *Physical Review B* **61**, 2981–2990 (2000).

[34] Kataura, H. *et al.* Optical properties of single-wall carbon nanotubes. *Synthetic Metals* **103**, 2555–2558 (1999).

[35] Dukovic, G. *et al.* Structural dependence of excitonic optical transitions and band-gap energies in carbon nanotubes. *Nano Letters* **5**, 2314–2318 (2005).

[36] Ando, T. Effects of valley mixing and exchange on excitons in carbon nanotubes with Aharonov-Bohm flux. *Journal of the Physical Society of Japan* **75**, 024707 (2006).

[37] Shaver, J. & Kono, J. Temperature-dependent magneto-photoluminescence spectroscopy of carbon nanotubes: evidence for dark excitons. *Laser & Photonics Reviews* **1**, 260–274 (2007).

[38] Walsh, A. G. *et al.* Scaling of exciton binding energy with external dielectric function in carbon nanotubes. *Physica E: Low-dimensional Systems and Nanostructures* **40**, 2375–2379 (2008).

[39] Kane, C. L. & Mele, E. J. Electron interactions and scaling relations for optical excitations in carbon nanotubes. *Physical Review Letters* **93**, 197402 (2004).

[40] Torrens, O. N., Milkie, D. E., Zheng, M. & Kikkawa, J. M. Photoluminescence from intertube carrier migration in single-walled carbon nanotube bundles. *Nano Letters* **6**, 2864–2867 (2006).

[41] Tan, P. H. *et al.* Photoluminescence spectroscopy of carbon nanotube bundles: Evidence for exciton energy transfer. *Physical Review Letters* **99**, 137402 (2007).

[42] Qian, H. *et al.* Exciton energy transfer in pairs of single-walled carbon nanotubes. *Nano Letters* **8**, 1363–1367 (2008).

[43] O'Connell, M. J. *et al.* Band gap fluorescence from individual single-walled carbon nanotubes. *Science* **297**, 593–596 (2002).

[44] Islam, M. F., Rojas, E., Bergey, D. M., Johnson, A. T. & Yodh, A. G. High weight fraction surfactant solubilization of single-wall carbon nanotubes in water. *Nano Letters* **3**, 269–273 (2003).

[45] Moore, V. C. *et al.* Individually suspended single-walled carbon nanotubes in various surfactants. *Nano Letters* **3**, 1379–1382 (2003).

[46] Matarredona, O. *et al.* Dispersion of single-walled carbon nanotubes in aqueous solutions of the anionic surfactant NaDDBS. *The Journal of Physical Chemistry B* **107**, 13357–13367 (2003).

[47] Zheng, M. *et al.* DNA-assisted dispersion and separation of carbon nanotubes. *Nature Materials* **2**, 338–342 (2003).

[48] Nish, A., Hwang, J.-Y., Doig, J. & Nicholas, R. J. Highly selective dispersion of single-walled carbon nanotubes using aromatic polymers. *Nature Nanotechnology* **2**, 640–646 (2007).

[49] Hartschuh, A., Pedrosa, H. N., Novotny, L. & Krauss, T. D. Simultaneous fluorescence and Raman scattering from single carbon nanotubes. *Science* **301**, 1354–1356 (2003).

[50] Lefebvre, J., Fraser, J., Homma, Y. & Finnie, P. Photoluminescence from single-walled carbon nanotubes: a comparison between suspended and micelle-encapsulated nanotubes. *Applied Physics A* **78**, 1107–1110 (2004).

[51] Ohno, Y. *et al.* Chirality-dependent environmental effects in photoluminescence of single-walled carbon nanotubes. *Physical Review B* **73**, 235427 (2006).

[52] Miyauchi, Y. *et al.* Dependence of exciton transition energy of single-walled carbon nanotubes on surrounding dielectric materials. *Chemical Physics Letters* **442**, 394–399 (2007).

[53] Ohno, Y. *et al.* Excitonic transition energies in single-walled carbon nanotubes: Dependence on environmental dielectric constant. *Physica Status Solidi (b)* **244**, 4002–4005 (2007).

[54] Matsuda, K., Inoue, T., Murakami, Y., Maruyama, S. & Kanemitsu, Y. Exciton fine structure in a single carbon nanotube revealed through spectral diffusion. *Physical Review B* **77**, 193405 (2008).

[55] Ai, N., Walden-Newman, W., Song, Q., Kalliakos, S. & Strauf, S. Suppression of blinking and enhanced exciton emission from individual carbon nanotubes. *ACS Nano* **5**, 2664–2670 (2011).

[56] Ma, X. *et al.* Influence of exciton dimensionality on spectral diffusion of single-walled carbon nanotubes. *ACS Nano* **8**, 10613–10620 (2014).

[57] Cognet, L. *et al.* Stepwise quenching of exciton fluorescence in carbon nanotubes by single-molecule reactions. *Science* **316**, 1465–1468 (2007).

[58] Chiashi, S., Watanabe, S., Hanashima, T. & Homma, Y. Influence of gas adsorption on optical transition energies of single-walled carbon nanotubes. *Nano Letters* **8**, 3097–3101 (2008).

[59] Cassell, A. M. *et al.* Directed growth of free-standing single-walled carbon nanotubes. *Journal of the American Chemical Society* **121**, 7975–7976 (1999).

[60] Homma, Y., Kobayashi, Y., Ogino, T. & Yamashita, T. Growth of suspended carbon nanotube networks on 100-nm-scale silicon pillars. *Applied Physics Letters* **81**, 2261–2263 (2002).

[61] Lefebvre, J., Homma, Y. & Finnie, P. Bright band gap photoluminescence from unprocessed single-walled carbon nanotubes. *Physical Review Letters* **90**, 217401 (2003).

[62] Walsh, A. G. *et al.* Screening of excitons in single, suspended carbon nanotubes. *Nano Letters* **7**, 1485–1488 (2007).

[63] Perebeinos, V., Tersoff, J. & Avouris, P. Scaling of excitons in carbon nanotubes. *Physical Review Letters* **92**, 257402 (2004).

[64] Kiowski, O. *et al.* Photoluminescence microscopy of carbon nanotubes grown by chemical vapor deposition: Influence of external dielectric screening on optical transition energies. *Physical Review B* **75**, 075421 (2007).

[65] Glückert, J. T. *Optical spectroscopy of individual single-walled carbon nanotubes in an electric gate structure: tuning the photoluminescence with electric fields*. Dissertation, Ludwig-Maximilians-Universität München (2014).

[66] Fox, M. *Quantum Optics : an introduction* (Oxford University Press, 2006).

[67] Yang, F. *et al.* Chirality-specific growth of single-walled carbon nanotubes on solid alloy catalysts. *Nature* **510**, 522–524 (2014).

[68] Sanchez-Valencia, J. R. *et al.* Controlled synthesis of single-chirality carbon nanotubes. *Nature* **512**, 61–64 (2014).

[69] Bachilo, S. M. *et al.* Narrow (n,m)-distribution of single-walled carbon nanotubes grown using a solid supported catalyst. *Journal of the American Chemical Society* **125**, 11186–11187 (2003).

[70] Kong, J., Soh, H. T., Cassell, A. M., Quate, C. F. & Dai, H. Synthesis of individual single-walled carbon nanotubes on patterned silicon wafers. *Nature* **395**, 878–881 (1998).

[71] An, L., Owens, J. M., McNeil, L. E. & Liu, J. Synthesis of nearly uniform single-walled carbon nanotubes using identical metal-containing molecular nanoclusters as catalysts. *Journal of the American Chemical Society* **124**, 13688–13689 (2002).

[72] Li, X. *et al.* Selective synthesis combined with chemical separation of single-walled carbon nanotubes for chirality selection. *Journal of the American Chemical Society* **129**, 15770–15771 (2007).

[73] Chiang, W.-H. & Sankaran, R. M. Linking catalyst composition to chirality distributions of as-grown single-walled carbon nanotubes by tuning Ni_xFe_{1-x} nanoparticles. *Nature Materials* **8**, 882–886 (2009).

[74] He, M. *et al.* Predominant (6,5) single-walled carbon nanotube growth on a copper-promoted iron catalyst. *Journal of the American Chemical Society* **132**, 13994–13996 (2010).

[75] He, M. *et al.* Chiral-selective growth of single-walled carbon nanotubes on lattice-mismatched epitaxial cobalt nanoparticles. *Scientific Reports* **3**, 1460 (2013).

[76] Joselevich, E., Dai, H., Liu, J., Hata, K. & H. Windle, A. Carbon nanotube synthesis and organization. In Jorio, A., Dresselhaus, G. & Dresselhaus, M. S. (eds.) *Carbon Nanotubes, Topics in Applied Physics*, vol. 111, 101–165 (Springer Berlin Heidelberg, 2008).

[77] Hafner, J. H. *et al.* Catalytic growth of single-wall carbon nanotubes from metal particles. *Chemical Physics Letters* **296**, 195–202 (1998).

[78] Nikolaev, P. *et al.* Gas-phase catalytic growth of single-walled carbon nanotubes from carbon monoxide. *Chemical Physics Letters* **313**, 91–97 (1999).

[79] Maruyama, S., Kojima, R., Miyauchi, Y., Chiashi, S. & Kohno, M. Low-temperature synthesis of high-purity single-walled carbon nanotubes from alcohol. *Chemical Physics Letters* **360**, 229–234 (2002).

[80] Wagner, R. S. & Ellis, W. C. Vapor-liquid-solid mechanism of single crystal growth. *Applied Physics Letters* **4**, 89–90 (1964).

[81] Baker, R., Barber, M., Harris, P., Feates, F. & Waite, R. Nucleation and growth of carbon deposits from the nickel catalyzed decomposition of acetylene. *Journal of Catalysis* **26**, 51–62 (1972).

[82] Baker, R., Harris, P., Thomas, R. & Waite, R. Formation of filamentous carbon from iron, cobalt and chromium catalyzed decomposition of acetylene. *Journal of Catalysis* **30**, 86–95 (1973).

[83] Moisala, A., Nasibulin, A. G. & Kauppinen, E. I. The role of metal nanoparticles in the catalytic production of single-walled carbon nanotubes – a review. *Journal of Physics: Condensed Matter* **15**, S3011 (2003).

[84] Hofmann, S. *et al.* In situ observations of catalyst dynamics during surface-bound carbon nanotube nucleation. *Nano Letters* **7**, 602–608 (2007).

[85] Yoshida, H., Takeda, S., Uchiyama, T., Kohno, H. & Homma, Y. Atomic-scale in-situ observation of carbon nanotube growth from solid state iron carbide nanoparticles. *Nano Letters* **8**, 2082–2086 (2008).

[86] Li, Y. *et al.* Growth of single-walled carbon nanotubes from discrete catalytic nanoparticles of various sizes. *The Journal of Physical Chemistry B* **105**, 11424–11431 (2001).

[87] Cheung, C. L., Kurtz, A., Park, H. & Lieber, C. M. Diameter-controlled synthesis of carbon nanotubes. *The Journal of Physical Chemistry B* **106**, 2429–2433 (2002).

[88] Kukovitsky, E., L'vov, S. & Sainov, N. VLS-growth of carbon nanotubes from the vapor. *Chemical Physics Letters* **317**, 65–70 (2000).

[89] Helveg, S. *et al.* Atomic-scale imaging of carbon nanofibre growth. *Nature* **427**, 426–429 (2004).

[90] Lin, M. *et al.* Dynamical observation of bamboo-like carbon nanotube growth. *Nano Letters* **7**, 2234–2238 (2007).

[91] Yoshida, H. *et al.* Atomic-scale analysis on the role of molybdenum in iron-catalyzed carbon nanotube growth. *Nano Letters* **9**, 3810–3815 (2009).

[92] Jourdain, V. & Bichara, C. Current understanding of the growth of carbon nanotubes in catalytic chemical vapour deposition. *Carbon* **58**, 2–39 (2013).

[93] Jungen, A., Stampfer, C., Durrer, L., Helbling, T. & Hierold, C. Amorphous carbon contamination monitoring and process optimization for single-walled carbon nanotube integration. *Nanotechnology* **18**, 075603 (2007).

[94] Furer, J. *Growth of Single-Wall Carbon Nanotubes by Chemical Vapor Deposition for Electrical Devices.* Ph.D. thesis, Universität Basel (2006).

[95] Homma, Y., Suzuki, S., Kobayashi, Y., Nagase, M. & Takagi, D. Mechanism of bright selective imaging of single-walled carbon nanotubes on insulators by scanning electron microscopy. *Applied Physics Letters* **84**, 1750–1752 (2004).

[96] Zhang, R. Y., Wei, Y., Nagahara, L. A., Amlani, I. & Tsui, R. K. The contrast mechanism in low voltage scanning electron microscopy of single-walled carbon nanotubes. *Nanotechnology* **17**, 272–276 (2006).

[97] Paillet, M. *et al.* Versatile synthesis of individual single-walled carbon nanotubes from nickel nanoparticles for the study of their physical properties. *Journal of Physical Chemistry B* **108**, 17112–17118 (2004).

[98] Paillet, M. *et al.* Growth and physical properties of individual single-walled carbon nanotubes. *Diamond and Related Materials* **14**, 1426–1431 (2005).

[99] Ishida, M., Hongo, H., Nihey, F. & Ochiai, Y. Diameter-controlled carbon nanotubes grown from lithographically defined nanoparticles. *Japanese Journal of Applied Physics* **43**, 1356 (2004).

[100] Lin, M. *et al.* Direct observation of single-walled carbon nanotube growth at the atomistic scale. *Nano Letters* **6**, 449–452 (2006).

[101] Limpert, E., Stahel, W. A. & Abbt, M. Log-normal distributions across the sciences: Keys and clues. *BioScience* **54**, 341–352 (2001).

[102] Yang, J. *et al.* Effect of oxygen plasma alumina treatment on growth of carbon nanotube forests. *The Journal of Physical Chemistry C* **118**, 18683–18692 (2014).

[103] Sharma, R., Rez, P., Brown, M., Du, G. & Treacy, M. M. J. Dynamic observations of the effect of pressure and temperature conditions on the selective synthesis of carbon nanotubes. *Nanotechnology* **18**, 125602 (2007).

[104] *Bruker Corporation* Dimension Icon User Guide
http://www.nanophys.kth.se/nanophys/facilities/nfl/afm/icon/bruker-help/DIcon_webhelp_Left.htm
SPM Training Guide > Atomic Force Microscopy (AFM) > AFM Image Quality.

[105] Schaffroth, L. *Analysis of Growth Parameters for Chemical Vapor Deposition of Carbon Nanotubes.* Bachelor thesis, Ludwig-Maximilians-Universität München (2015).

[106] Hofmann, M. S. *et al.* Synthesis and cryogenic spectroscopy of narrow-diameter single-wall carbon nanotubes. *Carbon* **105**, 622–627 (2016).

[107] http://www.swentnano.com/uploads/3/0/7/0/30708225/sg65i_tds_rev3.pdf.

[108] http://www.nanointegris.com/en/hipco.

[109] Empedocles, S. A. & Bawendi, M. G. Quantum-confined stark effect in single CdSe nanocrystallite quantum dots. *Science* **278**, 2114–2117 (1997).

[110] Gómez, D. E., van Embden, J. & Mulvaney, P. Spectral diffusion of single semiconductor nanocrystals: The influence of the dielectric environment. *Applied Physics Letters* **88**, 154106 (2006).

[111] Müller, J. *et al.* Monitoring surface charge movement in single elongated semiconductor nanocrystals. *Physical Review Letters* **93**, 167402 (2004).

[112] Rothenberg, E., Kazes, M., Shaviv, E. & Banin, U. Electric field induced switching of the fluorescence of single semiconductor quantum rods. *Nano Letters* **5**, 1581–1586 (2005).

[113] Georgi, C. *et al.* Photoinduced luminescence blinking and bleaching in individual single-walled carbon nanotubes. *ChemPhysChem* **9**, 1460–1464 (2008).

[114] Yoshikawa, K., Matsuda, K. & Kanemitsu, Y. Exciton transport in suspended single carbon nanotubes studied by photoluminescence imaging spectroscopy. *The Journal of Physical Chemistry C* **114**, 4353–4356 (2010).

[115] Bachilo, S. M. *et al.* Structure-assigned optical spectra of single-walled carbon nanotubes. *Science* **298**, 2361–2366 (2002).

[116] Chou, S. G. *et al.* Phonon-assisted excitonic recombination channels observed in DNA-wrapped carbon nanotubes using photoluminescence spectroscopy. *Physical Review Letters* **94**, 127402 (2005).

[117] Htoon, H., O'Connell, M. J., Doorn, S. K. & Klimov, V. I. Single carbon nanotubes probed by photoluminescence excitation spectroscopy: The role of phonon-assisted transitions. *Physical Review Letters* **94**, 127403 (2005).

[118] Perebeinos, V., Tersoff, J. & Avouris, P. Effect of exciton-phonon coupling in the calculated optical absorption of carbon nanotubes. *Physical Review Letters* **94**, 027402 (2005).

[119] Vialla, F. *et al.* Unifying the low-temperature photoluminescence spectra of carbon nanotubes: The role of acoustic phonon confinement. *Physical Review Letters* **113**, 057402 (2014).

[120] Galland, C., Högele, A., Türeci, H. E. & Imamoğlu, A. Non-Markovian decoherence of localized nanotube excitons by acoustic phonons. *Physical Review Letters* **101**, 067402 (2008).

[121] Krummheuer, B., Axt, V. M. & Kuhn, T. Theory of pure dephasing and the resulting absorption line shape in semiconductor quantum dots. *Physical Review B* **65**, 195313 (2002).

[122] Savin, A. V., Hu, B. & Kivshar, Y. S. Thermal conductivity of single-walled carbon nanotubes. *Physical Review B* **80**, 195423 (2009).

[123] Wilson-Rae, I., Galland, C., Zwerger, W. & Imamoğlu, A. Exciton-assisted optomechanics with suspended carbon nanotubes. *New Journal of Physics* **14**, 115003 (2012).

[124] http://www.temwindows.com/product_p/sn100-a50mp2q05.htm.

[125] Lefebvre, J., Finnie, P. & Homma, Y. Temperature-dependent photoluminescence from single-walled carbon nanotubes. *Physical Review B* **70**, 045419 (2004).

[126] Sarpkaya, I. *et al.* Prolonged spontaneous emission and dephasing of localized excitons in air-bridged carbon nanotubes. *Nature Communications* **4** (2013).

[127] Zaric, S. *et al.* Optical signatures of the Aharonov-Bohm phase in single-walled carbon nanotubes. *Science* **304**, 1129–1131 (2004).

[128] Srivastava, A., Htoon, H., Klimov, V. I. & Kono, J. Direct observation of dark excitons in individual carbon nanotubes: Inhomogeneity in the exchange splitting. *Physical Review Letters* **101**, 087402 (2008).

[129] Matsunaga, R., Matsuda, K. & Kanemitsu, Y. Evidence for dark excitons in a single carbon nanotube due to the Aharonov-Bohm effect. *Physical Review Letters* **101**, 147404 (2008).

[130] Shaver, J. *et al.* Magnetic brightening of carbon nanotube photoluminescence through symmetry breaking. *Nano Letters* **7**, 1851–1855 (2007).

[131] Bronikowski, M. J., Willis, P. A., Colbert, D. T., Smith, K. A. & Smalley, R. E. Gas-phase production of carbon single-walled nanotubes from carbon monoxide via the HiPco process: A parametric study. *Journal of Vacuum Science & Technology A* **19**, 1800–1805 (2001).

[132] Kitiyanan, B., Alvarez, W. E., Harwell, J. H. & Resasco, D. E. Controlled production of single-wall carbon nanotubes by catalytic decomposition of CO on bimetallic Co-Mo catalysts. *Chemical Physics Letters* **317**, 497–503 (2000).

[133] Hirori, H., Matsuda, K., Miyauchi, Y., Maruyama, S. & Kanemitsu, Y. Exciton localization of single-walled carbon nanotubes revealed by femtosecond excitation correlation spectroscopy. *Physical Review Letters* **97**, 257401 (2006).

[134] Hofmann, M. S. *et al.* Bright, long-lived and coherent excitons in carbon nanotube quantum dots. *Nature Nanotechnology* **8**, 502–505 (2013).

[135] Miyauchi, Y. *et al.* Brightening of excitons in carbon nanotubes on dimensionality modification. *Nature Photonics* **7**, 715–719 (2013).

[136] Piao, Y. *et al.* Brightening of carbon nanotube photoluminescence through the incorporation of sp^3 defects. *Nature Chemistry* **5**, 840–845 (2013).

[137] Ma, X., Hartmann, N. F., Baldwin, J. K. S., Doorn, S. K. & Htoon, H. Room-temperature single-photon generation from solitary dopants of carbon nanotubes. *Nature Nanotechnology* **10**, 671–675 (2015).

[138] Galland, C. & Imamoğlu, A. All-optical manipulation of electron spins in carbon-nanotube quantum dots. *Physical Review Letters* **101**, 157404 (2008).

[139] Ghosh, S., Bachilo, S. M., Simonette, R. A., Beckingham, K. M. & Weisman, R. B. Oxygen doping modifies near-infrared band gaps in fluorescent single-walled carbon nanotubes. *Science* **330**, 1656–1659 (2010).

[140] Ma, X. *et al.* Electronic structure and chemical nature of oxygen dopant states in carbon nanotubes. *ACS Nano* **8**, 10782–10789 (2014).

[141] Lüer, L. *et al.* Size and mobility of excitons in (6, 5) carbon nanotubes. *Nature Physics* **5**, 54–58 (2009).

[142] Georgi, C., Böhmler, M., Qian, H., Novotny, L. & Hartschuh, A. Probing exciton propagation and quenching in carbon nanotubes with near-field optical microscopy. *Physica Status Solidi (b)* **246**, 2683–2688 (2009).

[143] Moritsubo, S. *et al.* Exciton diffusion in air-suspended single-walled carbon nanotubes. *Physical Review Letters* **104**, 247402 (2010).

[144] Hertel, T., Himmelein, S., Ackermann, T., Stich, D. & Crochet, J. Diffusion limited photoluminescence quantum yields in 1-D semiconductors: Single-wall carbon nanotubes. *ACS Nano* **4**, 7161–7168 (2010).

[145] Harrah, D. M. & Swan, A. K. The role of length and defects on optical quantum efficiency and exciton decay dynamics in single-walled carbon nanotubes. *ACS Nano* **5**, 647–655 (2011).

[146] Xie, J., Inaba, T., Sugiyama, R. & Homma, Y. Intrinsic diffusion length of excitons in long single-walled carbon nanotubes from photoluminescence spectra. *Physical Review B* **85**, 085434 (2012).

[147] Siitonen, A. J., Bachilo, S. M., Tsyboulski, D. A. & Weisman, R. B. Evidence for long-lived, optically generated quenchers of excitons in single-walled carbon nanotubes. *Nano Letters* **12**, 33–38 (2012).

[148] Crochet, J. J. *et al.* Disorder limited exciton transport in colloidal single-wall carbon nanotubes. *Nano Letters* **12**, 5091–5096 (2012).

[149] Oudjedi, L., Parra-Vasquez, A. N. G., Godin, A. G., Cognet, L. & Lounis, B. Metrological investigation of the (6,5) carbon nanotube absorption cross section. *The Journal of Physical Chemistry Letters* **4**, 1460–1464 (2013).

[150] Ishii, A., Yoshida, M. & Kato, Y. K. Exciton diffusion, end quenching, and exciton-exciton annihilation in individual air-suspended carbon nanotubes. *Physical Review B* **91**, 125427 (2015).

[151] Capaz, R. B., Spataru, C. D., Tangney, P., Cohen, M. L. & Louie, S. G. Temperature dependence of the band gap of semiconducting carbon nanotubes. *Physical Review Letters* **94**, 036801 (2005).

[152] Viña, L., Logothetidis, S. & Cardona, M. Temperature dependence of the dielectric function of germanium. *Physical Review B* **30**, 1979–1991 (1984).

[153] Cambré, S. *et al.* Luminescence properties of individual empty and water-filled single-walled carbon nanotubes. *ACS Nano* **6**, 2649–2655 (2012).

[154] Finnie, P., Homma, Y. & Lefebvre, J. Band-gap shift transition in the photoluminescence of single-walled carbon nanotubes. *Physical Review Letters* **94**, 247401 (2005).

[155] Choi, J. H. & Strano, M. S. Solvatochromism in single-walled carbon nanotubes. *Applied Physics Letters* **90**, 223114 (2007).

[156] Perebeinos, V., Tersoff, J. & Avouris, P. Radiative lifetime of excitons in carbon nanotubes. *Nano Letters* **5**, 2495–2499 (2005).

[157] Spataru, C. D., Ismail-Beigi, S., Capaz, R. B. & Louie, S. G. Theory and abăinitio calculation of radiative lifetime of excitons in semiconducting carbon nanotubes. *Physical Review Letters* **95**, 247402 (2005).

[158] Hüttel, A. K. *et al.* Carbon nanotubes as ultrahigh quality factor mechanical resonators. *Nano Letters* **9**, 2547–2552 (2009).

[159] Bulaev, D. V., Trauzettel, B. & Loss, D. Spin-orbit interaction and anomalous spin relaxation in carbon nanotube quantum dots. *Physical Review B* **77**, 235301 (2008).

[160] Balasubramanian, G. *et al.* Ultralong spin coherence time in isotopically engineered diamond. *Nature Materials* **8**, 383–387 (2009).

[161] Pályi, A., Struck, P. R., Rudner, M., Flensberg, K. & Burkard, G. Spin-orbit-induced strong coupling of a single spin to a nanomechanical resonator. *Physical Review Letters* **108**, 206811 (2012).

[162] Lefebvre, J., Austing, D. G., Bond, J. & Finnie, P. Photoluminescence imaging of suspended single-walled carbon nanotubes. *Nano Letters* **6**, 1603–1608 (2006).

[163] Cao, J., Wang, Q. & Dai, H. Electron transport in very clean, as-grown suspended carbon nanotubes. *Nature Materials* **4**, 745–749 (2005).

[164] Hauck, M. *et al.* Locating environmental charge impurities with confluent laser spectroscopy of multiple quantum dots. *Physical Review B* **90**, 235306 (2014).

[165] Gokus, T. *et al.* Mono- and biexponential luminescence decays of individual single-walled carbon nanotubes. *The Journal of Physical Chemistry C* **114**, 14025–14028 (2010).

[166] Capaz, R. B., Spataru, C. D., Ismail-Beigi, S. & Louie, S. G. Diameter and chirality dependence of exciton properties in carbon nanotubes. *Physical Review B* **74**, 121401 (2006).

[167] Murakami, Y. & Kono, J. Nonlinear photoluminescence excitation spectroscopy of carbon nanotubes: Exploring the upper density limit of one-dimensional excitons. *Physical Review Letters* **102**, 037401 (2009).

[168] Santori, C., Pelton, M., Solomon, G., Dale, Y. & Yamamoto, Y. Triggered single photons from a quantum dot. *Physical Review Letters* **86**, 1502–1505 (2001).

[169] Tinnefeld, P., Müller, C. & Sauer, M. Time-varying photon probability distribution of individual molecules at room temperature. *Chemical Physics Letters* **345**, 252–258 (2001).

[170] Endo, T., Ishi-Hayase, J. & Maki, H. Photon antibunching in single-walled carbon nanotubes at telecommunication wavelengths and room temperature. *Applied Physics Letters* **106**, 113106 (2015).

[171] Tayo, B. O. & Rotkin, S. V. Charge impurity as a localization center for singlet excitons in single-wall nanotubes. *Physical Review B* **86**, 125431 (2012).

[172] Santori, C., Fattal, D., Vuckovic, J., Solomon, G. S. & Yamamoto, Y. Indistinguishable photons from a single-photon device. *Nature* **419**, 594–597 (2002).

[173] Gomes, K. K., Mar, W., Ko, W., Guinea, F. & Manoharan, H. C. Designer dirac fermions and topological phases in molecular graphene. *Nature* **483**, 306–310 (2012).

[174] Childress, L. *et al.* Coherent dynamics of coupled electron and nuclear spin qubits in diamond. *Science* **314**, 281–285 (2006).

List of abbreviations

1D	one-dimensional
2D	two-dimensional
AFM	atomic force microscopy
APD	avalanche photodiode
CCD	charge-coupled device
CNT	carbon nanotube
CVD	chemical vapor deposition
cw	continuous wave
FWHM	full width at half maximum
HBT	Hanbury Brown and Twiss
PL	photoluminescence
PLE	photoluminescence excitation
RBM	radial breathing mode
SEM	scanning electron microscopy
SWNT	single-walled carbon nanotube
TEM	transmission electron microscopy
UV	ultraviolet
VHs	Van Hove singularities
VLS	vapor-liquid-solid

List of publications

- M. S. Hofmann, J. T. Glückert, J. Noé, C. Bourjau, R. Dehmel & A. Högele
  Bright, long-lived and coherent excitons in carbon nanotube quantum dots
  Nature Nanotechnology **8**, 502–505 (2013)

- N. Mauser, N. Hartmann, M. S. Hofmann, J. Janik, A. Högele & A. Hartschuh
  Antenna-enhanced optoelectronic probing of carbon nanotubes
  Nano Letters **14**, 3773–3778 (2014)

- M. S. Hofmann, J. Noé, A. Kneer, J. J. Crochet & A. Högele
  Ubiquity of exciton localization in cryogenic carbon nanotubes
  Nano Letters **16**, 2958–2962 (2016)

- M. S. Hofmann, J. Noé, M. Nutz, A. Kneer, R. Dehmel, L. Schaffroth & A. Högele
  Synthesis and cryogenic spectroscopy of narrow-diameter single-wall carbon nanotubes
  Carbon **105**, 622–627 (2016)

- T. Hümmer, J. Noé, M. S. Hofmann, T. W. Hänsch, A. Högele & D. Hunger
  Cavity-enhanced Raman microscopy of individual carbon nanotubes
  Nature Communications **7**, 12155 (2016)

Danksagung

Zu guter Letzt möchte ich mich bei all denjenigen bedanken, die mich während der letzten Jahre unterstützt und begleitet haben und so zum Gelingen und Fertigstellen dieser Arbeit maßgeblich beigetragen haben.

An erster Stelle danke ich meinem Doktorvater Alex Högele für die Möglichkeit, die Röhren zu beleuchten. Ein herzliches Dankeschön für deine stets offene Tür, deinen Optimismus und deine unentwegte Unterstützung in allen Themenbereichen und Belangen.

Jörg Kotthaus danke ich für den Rahmen, der alles zusammenhält. Die tolle Atmosphäre am Lehrstuhl kommt nicht von alleine.

Ein großes Dankeschön geht an Jan Glückert. Danke für die freundschaftliche Zusammenarbeit und Unterstützung im Ramanlabor. Ich hatte immer viel Spaß bei unserer gemeinschaftlichen Erkundung von Erwin und Co.

Danke an alle Master- und Bachelorstudenten:
Vielen Dank an Jonathan Noé. Mit deiner lebendigen und interessierten Art hast du meinen Arbeitsalltag sehr bereichert. Alexander Kneer, Michael Förg, Christian Bourjau, Raphael Dehmel, Fabian Storek; ein großes Dankeschön für euer aller Engagement, euer Mitwirken und die wertvollen Beiträge.

Meinen Bürokollegen Jonathan Noé, Manuel Nutz, Jessica Lindlau, Enrico Schubert, Jens Repp, Thomas Faust und Johannes Rieger danke ich für die gesellige und humorvolle Atmosphäre an den Schreibtischen. Manuel, danke auch für deine Hilfsbereitschaft bei Programmierfragen und Druckerproblemen.

Ich möchte auch allen weiteren Nanophotonikern im Hause danken. Es war mir immer eine Freude Seite an Seite bzw. Tür an Tür mit euch zu arbeiten. Danke an Andre Neumann, Matthias Hauck, Florian Seilmeier, Sarah Wittig, Léo Colombier und Jiaxiang Zhang.

Darren Southworth danke ich für das aufwendige Korrekturlesen der wichtigen Abschnitte.

Dem Organisationsteam Martina Edenhofer und Bert Lorenz danke ich dafür, dass der Betrieb am Lehrstuhl so reibungslos abläuft. Vielen Dank auch für eure Unterstützung bei bürokratischen Themen.

Besonderen Dank verdient auch das Reinraumteam Philipp Altpeter und Reinhold Rath. Danke für die Unterstützung bei der Probenfabrikation und die große Hilfe bei der CVD.

Anton Heindl danke ich für die zuverlässige Versorgung mit Helium und Stickstoff.

Danke an Stephan Manus für die Elektronik am Experiment.

Danke den Mitstreitern Florian Forster, Sergey Platonov, Sebastian Stapfner, Gunnar Petersen und Georg Schinner für Austausch, Unterstützung, Späße und gemeinsame Mittagessen.

Herzlichen Dank an die "Externen" Nina Mauser, Andrés Vargas Lugo Cantú und Antoine Reserbat-Plantey für den wissenschaftlichen Austausch und die gute Zusammenarbeit.

Heidi und Kurt danke ich für die große Unterstützung im Hintergrund.

Meiner Familie danke ich für den großen Rahmen, der alles erst ermöglicht hat.

Katharina, dir danke ich einfach dafür, dass es dich gibt und du mir so unglaublich viel Freude bereitest.

Steffi, DANKE für deine schier endlose Unterstützung, dein Verständnis und dafür, dass du mich immer wieder aufgebaut und motiviert hast.